Dissertation

Resonant MEMS sensors for real-time oil condition monitoring

Zur Erlangung des akademischen Grades

Doktor der technischen Wissenschaften (Dr. techn.)

Institut für Sensor- und Aktuatorsysteme

Technische Universität Wien

Dipl.-Ing. Florian Patocka

00927264

Wien, 2024

Acknowledgements

I would like to express my gratitude to my supervisor Univ.Prof. Dr. Ulrich Schmid, who not only made it possible for me to work on this dissertation, but also sparked my interest for the world of MEMS technology during my bachelor's degree. Having started out as a student assistant during my bachelor's degree, I am very happy to have been part of the Institute of Sensors and Actuators for so many years.

I would also like to thank Dr Michael Schneider for the countless fruitful discussions and helpful suggestions for a novice PhD student. Furthermore, many thanks are due to the cleanroom technicians Sophia Ewert, Michael Buchholz and Patrick Meyer, without whom the sensors would certainly not exist today in their current form.

The institute would not function without people who ensure order in the background. Many thanks to Martina Bittner, Martina 'Nussi' Nuhsbaumer and Andreas Astleitner for their prompt help at all times and in all matters.

This work was supported by the Austrian COMET-Program (K2, program InTribology, FFG-no. 906860, project coordinator AC2T research GmbH) and partially carried out at the "Excellence Center of Tribology" (AC2T research GmbH). In this regard, I would particularly like to thank Dr. Nicole Dörr and Dipl.-Ing. (FH) Christoph Schneidhofer, who drove the joint project forward in countless meetings and provided me with an understanding of the field of lubricant technology.

I would especially like to thank my parents, whose love and support made my academic journey possible in the first place. In times of doubt and exhaustion, I could always turn to them and find new motivation. Countless pages of this work were written in my grandmother's house in Lungau. A big thank you for the support (not only culinary) during these busy days.

Finally, I would like to thank my partner Kinza, who pushed me to finally finish my dissertation after all this time. Without her constant encouragement, it would not have been possible for me to finalise this thesis alongside a full-time job.

Abstract

In this thesis the application of resonant MEMS (micro-electromechanical Systems) cantilevered sensors for condition monitoring of lubricating oil is studied. This work is focused on the real-time detection of particulate matter suspended in the lubricating oil, an important enabler for inline monitoring of lubricant condition for, *e.g.*, predictive maintenance of critical infrastructure such as gas turbine and other heavy industrial machinery. During the course of this thesis two novel sensors for the detection of ferrous wear particles and oxidation-related varnish particles in lubricating oil were developed, fabricated and tested under lab conditions. The novel sensors utilize the resonance characteristics of the roof tile-shaped eigenmodes found in MEMS cantilevers and the unique physical properties of the particles to attract the particles of interest to the sensor where they adhere to the cantilever surface. The adhered particles change the total mass of the oscillating cantilever leading to a measurable change of the cantilever's resonant characteristics such as the mechanical resonance frequency and Q factor.

For the detection of ferrous wear particles, a MEMS cantilever with an integrated planar electromagnetic coil for installation in the oil circuit of lubricated machinery was developed and fabricated. The magnetic field of the coil attracts and accumulates suspended ferrous particles on the surface of the cantilever. The proof of concept was successfully demonstrated by detecting ferrous particles with a hydrodynamic diameter of 250 nm dispersed in deionized water with a concentration of 350 ppm. The detection range spans three magnitudes in particle size, covering the size range needed for detection of abnormal wear in lubricated machinery.

The second MEMS sensor developed in this thesis utilizes the polar properties of oxidation-related varnish particles by generating an electric field using a tailored interdigitated electrode structure integrated on the cantilever surface. The varnish particles are accumulated and can be detected by monitoring the resonance characteristics of the microcantilever. The sensor was exposed to artificially aged commercial turbine oil at various stages of oil deterioration. The sensor response in terms of resonance frequency and Q factor was compared to the results of conventional oil analysis techniques and showed a clear correlation with the varnish condition of the oil. To demonstrate the applicability of the MEMS sensor in an industrial environment for real-time monitoring of the oil condition, two test rigs were developed in which the sensor continuously monitored the oil quality. Again, the MEMS sensor performed as expected and the proof of concept was successfully demonstrated.

Kurzfassung

In dieser Arbeit wird die Anwendung piezoelektrisch angeregter MEMS (mikro-elektro-mechanische Systeme) Resonatoren für die Zustandsüberwachung von Schmierölen untersucht. Der Fokus wird hierbei auf die Detektion suspendierter Partikel im Schmieröl gelegt. Die Echtzeitüberwachung des Schmieröls hinsichtlich der Partikelkontamination ist eine wichtige Voraussetzung für den sicheren und wirtschaftlichen Betrieb kritischer technischer Infrastruktur, wie Gasturbinen zur Bereitstellung elektrischer Energie und anderer industrieller Großanlagen. Im Zuge dieser Arbeit wurden daher zwei neuartige MEMS-Sensoren auf Basis mikromechanischer Resonatoren zur Detektion ferromagnetischer Abriebpartikel und *Varnish*-Partikel, die durch die oxidative Alterung der Ölbestandteile entstehen, entwickelt, hergestellt und charakterisiert. Die Sensoren sind für den Betrieb im Ölkreislauf der Maschine ausgelegt und verwenden integrierte Aktuatoren, um die Partikel an die Oberfläche des Resonators zu binden. Die zusätzliche Masse der gebundenen Partikel bewirkt eine Änderung der Schwingungseigenschaften wie der Resonanzfrequenz und des Gütefaktors. Durch kontinuierliche Messung dieser Kenngrößen des Resonators kann so die Partikelkontamination des Schmieröls überwacht werden.

Zur Detektion der ferromagnetischen Abriebpartikel wurde ein mikromechanischer Resonator mit integrierter planarer elektromagnetischer Spule entwickelt. Das durch die Spule hervorgerufene Magnetfeld akkumuliert die im Öl suspendierten Abriebpartikel auf der Oberfläche des Resonators und bewirkt so eine Änderung der Schwingungseigenschaften. Durch die erfolgreiche Detektion von Eisenoxidpartikel in deionisiertem Wasser mit einem hydrodynamischen Durchmesser von 250 nm und einer Konzentration von 350 ppm wurde das Sensorkonzept erfolgreich in einem Laborversuch validiert. Der Detektionsbereich des neuartigen Sensors erstreckt sich über drei Größenordnungen der Partikelgröße und deckt damit den Größenbereich ab, der für die Erkennung von anormalem Verschleiß in geschmierten Maschinen erforderlich ist.

Der zweite in dieser Arbeit entwickelte Sensor nutzt die polaren Eigenschaften der *Varnish*-Partikel. Eine integrierte Elektrodenstruktur erzeugt ein inhomogenes elektrisches Feld, durch das die *Varnish*-Partikel gezielt an die Oberfläche des Resonators gebunden werden. Zum Funktionsnachweis wurden künstlich gealterte Turbinenöle eingesetzt. Es wurde gezeigt, dass die gemessenen Änderungen der Resonanzfrequenz und des Gütefaktors des Resonators hierbei abhängig vom Grad der oxidativen Alterung des Öls sind. Um die Anwendbarkeit des neuartigen Sensors im industriellen Umfeld zu untersuchen, wurden zwei Teststände entwickelt, die die Umgebungsbedingungen innerhalb des Ölkreislaufs geschmierter Maschinen simulieren. Hier zeigte sich, dass der Sensor unter realistischen Bedingungen in der Lage ist, im vorbeiströmenden Öl *Varnish*-Partikel zu detektieren.

Table of contents

1 Introduction

1.1 Motivation and state-of-the-art

The use of animal and vegetable oils to reduce friction on contact surfaces dates back to the Bronze Age. Tallow was used to lubricate the axels of chariots and Egyptian wall paintings give reason to believe that olive oil was used to move heavy stone objects when building the pyramids [1]. While the demands on lubricating oils were relatively low at that time, today's lubricating oils are expected to deliver consistent peak performance even under the harshest conditions, such as extreme temperatures, high mechanical loads and chemically contaminated environments. With the ever-increasing demand for higher performance and efficiency in all areas of industry, lubricating oils became more and more one of the central components of modern industrial machinery. This can be seen, for example, in the abundance of different available lubricants, whereby there is a specially adapted lubricating oil for almost every application. With very few exceptions, lubricating oils consist of two main components, base oil and additives. Base oil is typically a mixture of different hydrocarbons obtained by refining crude oil or synthesized from crude oil. Additives enhance the desired properties of the oil while suppressing undesirable properties. High running speeds and contact pressures demand higher thermal and mechanical load capacity to guarantee sufficient lubrication in all operating states of the machinery. Because of these demanding operating conditions, the lubricating oil is subjected to aging, which has a significant impact on its performance and lifetime. Therefore, three strategies for the maintenance of lubricated systems have been developed and are state of the art nowadays [2]:

1. *Reactive maintenance*: if continued operation is no longer possible due to the degraded condition of the oil.
2. *Preventive maintenance*: oil change at defined service intervals with sufficient safety margin; the intervals are determined by statistical analysis of the failure probability.
3. *Predictive maintenance*: maintenance is planned based on the actual (measured) condition of the lubricating oil.

It is obvious that the first approach is only applicable in the case of non-critical applications and is no longer considered to be relevant today. In contrast, preventive maintenance is the most widespread strategy in many areas. In this case the equipment manufacturer specifies a time interval during which the oil can be used under normal operating conditions. This procedure is mainly used for machines with small quantities of oil and short oil change intervals (*e.g.,* passenger cars), where the financial and environmental impact of a possibly premature oil change is negligible. However, this strategy is not suitable for machines with large oil reservoirs such as gas turbine or surface mining equipment, where several thousand liters of oil have a planned lifetime of up to 10 years and more [3]. During this long

period, it is difficult to schedule preventive oil changes, as the oil condition heavily depends on the operating mode and mechanical condition of the machinery. While the evolution of the oil condition in case of short oil change intervals can be described with sufficient accuracy using statistical methods, these models fail for the expected operating times of several years for industrial lubricating oils. In this case, maintenance of the lubricated machinery based on the actual oil condition is the only reasonable strategy to keep both economic and environmental costs at an acceptable level. The term *oil condition* is very general and can be understood as the oils ability to provide sufficient lubrication while adequately meeting all other requirements in the lubricated system, such as transferring heat and binding of contaminants. It is therefore obvious that the condition of the lubricating oil cannot be assessed accurately by a single physical property but is determined by considering the mutual dependence of the oil parameters, their variation over time and the operating conditions of the lubricated machinery.

Therefore, the fundamental question arises which oil parameters are to be monitored to assess the condition of the lubricating oil during operation. Table 1.1 gives an overview of the standard laboratory methods for various oil parameters as well as their interpretation in terms of lubricant condition [4]. These parameters are determined in regular intervals and are used to evaluate the remaining lifetime of the lubricant in use. With this approach, however, only snapshots of the oil condition are taken at fixed time intervals. In the case of sudden malfunctions, such as localized thermal overload due to a defective bearing, the oil condition can drop rapidly, causing the lubricated machine to fail before the oil degradation is detected at the next scheduled oil check. Additionally, oil samples have to be taken from the machinery and sent to a laboratory for analysis, increasing the logistic effort during the machine lifetime. For particularly critical applications, such as gas turbines in peak-load power plants and other heavy industrial machinery, there is therefore a growing need for real-time monitoring of the oil condition, allowing to react to sudden changes without any delay.

Table 1.1: Overview of various laboratory methods for determining various oil parameters and their interpretation in terms of lubricant condition [4].

Parameter	Method(s)	Interpretation
Viscosity	Capillary/rotational viscometer, measurement usually at 40°C and 100°C	Contamination (fuel, water), oxidative degradation
Acidity	Potentiometric titration of diluted oil sample	Oxidative degradation, additive depletion
Flash point	Heating at constant rate until vapor is ignited by test flame	Fuel contamination, thermal overload
Spectral properties (FTIR)	Comparison of the used oil spectra to a reference spectrum of fresh oil	Degradation, contaminants (soot, fuel, water), additive depletion
Oxidation reserve	Rotary pressure vessel oxidation test (RPVOT), turbine oxidation stability test (TOST)	Remaining antioxidative additive effect
Solid particle content	Visual inspection, gravimetric analysis of filter residues, centrifugation, ferrography	Wear debris particle contamination

Many of these laboratory measurement methods listed in Table 1.1 were adapted to allow for the measurement of the respective oil condition parameter in real-time by a tailored sensor integrated into the technical system of interest. For example, a widely used technique is the measurement of the oil viscosity using (micro)-acoustic devices such as quartz crystal microbalances (QCM) or vibrational methods employing tuning forks and microcantilevers [5] [6] [7] [8]. The latter were also successfully used to detect diesel contamination of engine oil in real-time [9].

Because of its significance for machine health, the detection of suspended particles in lubricating oils is the focus of many studies dating back more than three decades and is still a growing field today [10]. When talking about particle contamination of lubricating oils, two types are distinguished: hard wear debris particles and soft degradation-related contaminants caused by the formation of insoluble species in the oil. The following sections give an overview of the state-of-the-art for the real-time detection of such particles.

1.1.1 State-of-the-art for the detection of wear debris particles

Wear debris particles are the consequence of various processes, *e.g.*, abrasion, due to mechanical load in the lubricated system and are an important indicator of machine health and the trending thereof [11]. Hence, many different principles for the real-time detection of this type of particles have been developed. Early techniques relied on the continuous accumulation of ferrous particles and measuring the resulting change of inductivity or resistivity of the sensing elements [12] [13] [14] [15]. However, these sensors do not offer real-time capabilities, as they do not detect individual particles and only issue a warning when the number of accumulated particles exceeds a certain threshold limit. To allow for the real-time detection and characterization of wear particles, the inductive principle was further developed. The proposed sensors rely on the disturbance of a magnetic sensing field due to the wear particles. Using two- or three-dimensional coil structures, ferrous and non-ferrous particles can be distinguished and sized as they flow along the tubular sensing area [16] [17]. Due to the early introduction of this sensor principle and the continuous development in both industry and academia, inductive sensors have already been commercialized and are used in various industrial applications [18] [19] [20]. However, the smallest detectable particle size is in the range of 100 µm and above, which is too large to allow for an early detection of impending machine fault. Studies showed that during normal operating conditions, most wear debris particles are smaller than 10 µm [21]. In case of abnormal wear, larger particles are generated, whereas particles larger than 100 µm indicate severe wear and imminent failure of the lubricated machinery. Hence the inductive principle was adapted to allow for the detection of even smaller wear particles using microfluidic devices based on an inductive Coulter counting principle [22] [23]. Due to the use of microfluidic channels however, the throughput of these devices is limited to only a few milliliters per minute, rendering them unfeasible for real-time wear debris detection in industrial environments. Efforts were made to increase the throughput by parallelizing the detectors, which allows for the detection of wear particles in the range of 50 µm at a flow rate of approximately 500 ml/min [24]

[25] [26] [27] [28] [29]. However, some of these sensors showed issues in practical use due to clogging of the fluid channels and their inability to handle the occurring oil pressures.

An alternative approach relies on the influence of the wear particle on an electrostatic field by changing the capacitance of an electrode structure [30] [31]. Despite offering a high sensitivity down to 10 µm, the employed microfluidic channels reduce the throughput to only a few µl per minute and are prone to clogging due to the suspended particles. The direct measurement of the particle charge produced by wear processes allows for higher flow rates but the susceptibility of this detection scheme to electromagnetic interference renders its usage unfeasible in an industrial environment [32] [33] [34].

Acoustic wear particle sensors use ultrasonic transducers to emit acoustic pulses and monitor the echoes generated by the wear particles in the oil stream [35]. Based on the strength of the echo, information about the size of the particle can be deduced. To discriminate wear debris from entrained air bubbles, either the propagation direction or phase shift of the echo with respect to the initial pulse is used [36] [37]. However, this method has the major drawback that it cannot differentiate metallic wear debris from dielectric particles due to their similar acoustic reflection coefficient [38]. Despite a sensitivity of down to 3 µm, sensors based on these methods are not established in industrial use due to unresolved issues: Because the acoustic field emitted by the ultrasonic transducers is highly non-uniform, the effective sensing zone within the fluid channel is only in the range of a few millimeters in diameter and depth. If a particle passes the sensor outside this acoustic focal area, the size of the particle may be underestimated [39]. A reduction in the size of the oil channel can mitigate this problem, but significantly reduces the maximum flow rate. In addition, the shape of the particle has a major impact on the reflected echo, thus increasing the uncertainty of the particle size determination [40].

Finally, optical methods based on imaging the wear debris using charge-coupled devices (CCD) allow for the extraction of many important features, such as morphology, color, and material of the particles [41] [42] [43] [44]. However, due to the loss of oil transparency during operation, these methods cannot reliably detect wear debris in later stages of the machine life. Additionally, the hardware requirements are very high due to the large amount of data that must be recorded and analyzed in real-time. Despite the ability to detect and classify wear debris particles down to a size of 7 µm, this technique needs to be improved for industrial applications [45] [46].

1.1.2 State-of-the-art for soft degradation-related contaminants

In contrast to wear debris particles caused by abrasion, the soft degradation-related contaminants are caused by chemical reactions due to oxidation or thermal breakdown of oil constituents [47]. As explained in detail later (section 2.5.3), these degradation mechanisms lead to the formation of sub-micron particles via polymerization of the reaction products. Depending on the operating conditions of the machinery (*e.g.*, temperature, pressure, design of the oil circuit), these particles accumulate on oil-wetted surfaces in the oil circuit [48]. These deposits are called *varnish*, and the corresponding particles

are therefore henceforth referred to as *varnish particles*. Varnish can cause substantial damage to machines due to clogged oil feed lines, stuck valves, reduced heat transfer and increased friction of bearings. However, due to their small size, varnish particles cannot be detected by conventional particle detection techniques [49]. In addition, their solubility in oil depends significantly on the ambient conditions, so that the concentration of the particles can vary with changes in temperature or pressure. For this reason, up-to-date varnish particles cannot be detected directly, but changes in oil parameters that promote the formation of such particles are monitored [50]. A fundamental lubricant parameter is the viscosity, which depends strongly on the composition of the oil [51]. When varnish particles are formed, the polymerization of oil constituents causes an increase in the viscosity. At the same time, other contaminants, such as fuel and coolant, have the opposite effect, so that the measurement of viscosity alone is not considered sufficient to detect the formation of varnish particles [2]. Although usually not part of a laboratory-based analysis, monitoring oil permittivity [52] [53] [54] and conductivity [55] [56] is useful for real-time monitoring of oil condition, as both parameters are significantly influenced by the composition of the oil. However, due to their cross-sensitivity to other contaminants, such as wear debris, these methods are considered too unreliable for the detection of the imminent formation of varnish particles. In an attempt to specifically detect the acidic components in the oil, resonant devices based on QCM employing a chemical-sensitive layer were developed [57] [58] [59]. Although the sensor output signal scales with the number of acidic species in the oil, it was shown that the acidity has limited significance regarding the formation of varnish particles in lubricating oils [50]. Infrared spectroscopy is a widely used tool to determine the lubricant condition based on the infrared absorbance of an oil sample [60] [61] [62] [63] [64] [65] [66]. This principle usually uses devices such as a Fourier Transmission Infrared (FTIR) spectrometer to record the full infrared spectrum of the oil sample, which is then investigated for characteristic changes in comparison of a fresh reference oil sample. However, because certain degradation processes predominately affect the absorbance only in small wavelength regions (absorption bands), the instrumental effort can be significantly reduced by restricting the measurement to only a few wavelengths using monochromatic emitters, such as IR-diodes. It was shown that measuring the absorbance at two wavelengths is sufficient to detect the degradation of oil during operation [67] [68]. The major disadvantage of this technique is the expensive hardware and the vulnerability to contaminations of the optical path due to deposits and wear particles.

1.2 Aim and structure of this thesis

As described in the previous sections, the detection of particles for the purpose of real-time oil condition monitoring has attracted much attention in the recent decades. However, while the detection of wear debris particles is a well-established field with already commercialized sensor principles, no techniques for the direct detection of degradation-related varnish particles have been reported in literature so far. Therefore, novel sensing techniques are needed to allow for the detection of such particles in industrial lubricating oils with an “on board” integration capability.

Resonant MEMS (micro-electromechanical system) sensors are regarded to serve the requirements for this challenging application, especially when based on cantilevers as key function component. This is due to their exceptionally high sensitivity to even small changes of the environmental conditions that affect their mechanical key properties such as resonance frequency and even the quality factor [69]. By monitoring the resonance frequency of a selected mechanical mode, even small changes of the effective mass can be detected, making MEMS cantilevers applicable as ultra-precise mass sensors as demonstrated already in air by numerous studies [70, 71, 72, 73]. In liquids this sensor principle is also widely used for the detection of biochemicals and microorganisms such as viruses and bacteria, where the cantilever surface is functionalized to promote the binding of specific substances [74] [75]. Table 1.2 summarizes the key parameters, such as the detection limit and mass responsivity (resonance frequency shift per unit mass change) found in studies of resonant mass detection using MEMS cantilevers. It is apparent that an exceptionally high mass sensitivity and detection limit can be achieved, what predestines this measurement technique for the detection of suspended particles in oil. However, there are many unsolved issues regarding the application of resonant MEMS cantilevers for the detection of wear debris and varnish particles in lubricating oil, such as the high damping in viscous fluids, which dramatically reduces the mass sensing performance. Another unresolved question is how to attract the wear debris and varnish particles to the cantilever surface, which requires the development of new on chip particle manipulation techniques.

The aim of this thesis is to develop a sensor system based on resonant MEMS cantilevers that is able to detect suspended particles in lubricating oil and to prove its functionality in a test bench setup to simulate the operation in an industrial machinery oil circuit. The focus is on the detection of varnish particles since the direct real-time detection of varnish particle accumulation is a novelty. Furthermore, it will be investigated whether such a sensor system can also be applied to the detection of wear debris particle accumulation.

This thesis is structured as follows: Chapter 2 starts with an introduction to resonant MEMS cantilevers and their usage as mass sensors, measurement and fabrication methods used in this thesis as well as an overview of the field of lubricating oils and oil condition monitoring. Chapter 3 examines the use of non-conventional vibration modes for the purpose of mass detection, which serves as a foundation for subsequent measurements in lubricating oils. Chapter 4 presents the concept, fabrication, and characterization of the novel MEMS cantilever sensors for the detection of wear debris and varnish particles. In the last chapter of this thesis, these sensors are then tested in tailored testbenches and benchmarked against conventional oil analysis techniques to prove their functionality in an industrial-like environment.

Table 1.2: Overview of the relevant key parameters found in other studies of MEMS cantilevers for mass detection in liquids.

Authors	Dimensions	Frequency/Mode	Q factor	Responsivity	Detection limit	Read-Out	Application
Braun et al. [76]	500x100x1 μm^3	750 kHz, 13th out-of-plane (OOP)	-	400 Hz/ng	0.7ng	Optical	Latex beads in buffer
Braun et al. [77]	500x100x1 μm^3	~685 kHz, 14th OOP	-	~200 Hz/ng	0.5 ng	Optical	T5 phages in buffer
Davila et al. [78]	20x9x0.2 μm^3	-	2	100 Hz/pg	0.14 ng	Optical	B. anthracis Sterne spores in water
Jensen et al. [79]	500x100x1 μm^3	~640 kHz, 14th OOP		250 Hz/ng	< 1 ng	Optical	α-synuclein in buffer
Leahy et al. [80]	Paddle, ~320x70x10 μm^3	1.16 MHz, 7th OOP	36	~3 kHz/ng	-	Optical	E.Coli in deionized water
Tao et al. [81]	Paddle, ~190x270x5 μm^3	436 kHz, In-plane	22	8.8 Hz/pg	14 pg	Piezo resistive	Streptavidin-labeled beads in buffer
Tseng et al. [82]	500x100x1 μm^3	-	-	8.7 Hz/ng	-	Optical	MDMA in buffer
Walther et al. [83]	500x100x1 μm^3	370 kHz, 10th OOP	-	220 Hz/ng	50 pg	Optical	PS-beads in buffer

2 Device fundamentals

In this chapter the fundamental physical concepts and techniques used in this thesis are established. The chapter begins with an introduction to resonant MEMS cantilevers and their application as resonant mass sensors and explains how the piezoelectric effect is used as a transduction mechanism. Furthermore, the fabrication and characterization techniques used in this thesis are described. The chapter ends with an explanation of the most important aspects of lubrication engineering to enable the reader to follow the descriptions in the next chapters.

2.1 Resonant MEMS cantilevers

In this section, the theoretical framework to describe resonant MEMS cantilevers is established. After introducing fundamental kinetic and mechanical models of mechanically oscillating structures, the most important damping mechanisms and their influence on the vibrational performance of cantilevers are discussed. Finally, the section presents an introduction to mass detection with resonant MEMS cantilevers and the application of non-conventional eigenmodes for such sensor applications.

2.1.1 Lumped element resonator

Under the assumption that a cantilever oscillates in a linear regime, which is valid for small amplitudes, its motion can be described by the model of the so-called lumped element resonator [84]. In this model, the oscillating system is described by a zero-mass spring, a linear damping element (dashpot) and a mass. Assuming a time-dependent displacement $x(t)$ of the mass, the force balance equation according to Newton`s second law is

$$m\ddot{x}(t) + c\dot{x}(t) + kx(t) = F(t) \tag{2.1}$$

where m is the mass, c is the coefficient of damping, k is the spring constant and $F(t)$ is an external force exerted on the mass. Depending on the external force and the coefficient of damping, three cases can be distinguished:

1) Free undamped vibration: $F(t) = 0, c = 0$
2) Free damped vibration: $F(t) = 0, c \neq 0$
3) Driven damped vibration: $F(t) \neq 0, c \neq 0$

A short explanation of each fundamental case is given in the following sections. For sake of compactness, not all intermediate steps are shown when deriving the relevant parameters. Such a step-by-step derivation can be found for example in [85].

2.1.1.1 Free undamped vibration

In case of no external force and zero damping, the total energy stored in the system oscillates between the kinetic energy of the moving mass and the potential energy stored in the spring without any losses. The force balance equation in that case reads

$$m\ddot{x}(t) + kx(t) = 0 \tag{2.2}$$

what allows for the calculation of the *eigenfrequency*

$$\Omega = \sqrt{\frac{\mathrm{k}}{\mathrm{m}}} \tag{2.3}$$

of the system, *i.e.*, the frequency of mechanical oscillation in absence of any external force and damping.

2.1.1.2 Free damped vibration

In contrast to the previous case, the conversion between kinetic and potential energy is not lossless for a coefficient of damping $c \neq 0$, *i.e.*, energy is dissipated during each oscillation cycle. The solution of the force balance equation

$$m\ddot{x}(t) + c\dot{x}(t) + kx(t) = 0 \tag{2.4}$$

is in the form

$$x(t) = x_0 e^{\lambda t}. \tag{2.5}$$

Substituting this generic solution into the force balance equation and solving for λ one obtains the solutions

$$\lambda_{1,2} = -\frac{c}{2m} \pm \sqrt{\left(\frac{c}{2m}\right)^2 - \Omega^2}\,. \tag{2.6}$$

Depending on the term in the square root, three possible solutions exist:

1) $\frac{c}{2m} > \Omega$: overdamped system, no oscillation
2) $\frac{c}{2m} = \Omega$: critically damped
3) $\frac{c}{2m} < \Omega$: underdamped system, oscillating behavior

In case of an underdamped system, rewriting equation 2.6 using $i = \sqrt{-1}$ and the damping ratio

$$\zeta = \frac{c}{2m}\frac{1}{\Omega} \tag{2.7}$$

leads to

$$\lambda_{1,2} = -\Omega\left(\zeta \pm i\sqrt{1-\zeta^2}\right). \tag{2.8}$$

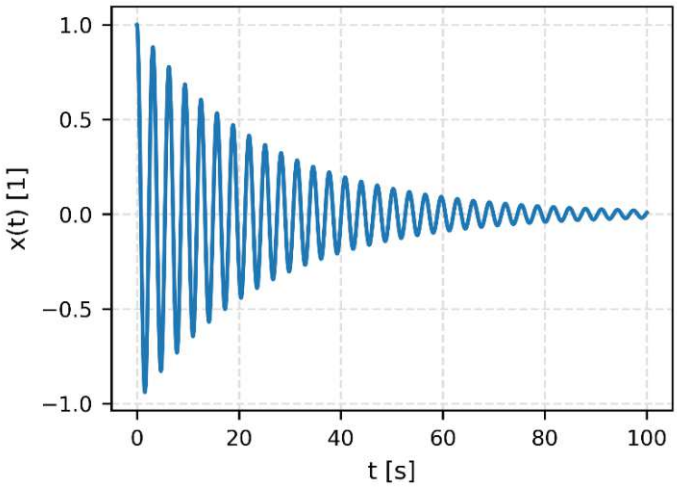

Figure 2-1: Amplitude of a free-damped system ((equation 2.9) with Ω = 2 Hz and ζ = 0.02.

Using this expression, the solution for a free damped system is

$$x(t) = x_0 e^{-\Omega\zeta t} \cos\left(\Omega\sqrt{1-\zeta^2}t\right), \tag{2.9}$$

which describes an exponentially decaying oscillation with an initial amplitude of x_0 (Figure 2-1). The frequency of the oscillation is the *natural frequency* of the system $\omega = \Omega\sqrt{1-\zeta^2}$, *i.e.*, the eigenfrequency of the system is reduced by a factor of $\sqrt{1-\zeta^2}$. For damping ratios $\zeta \ll 1$, it is valid to approximate the natural frequency as $\omega \approx \Omega$.

2.1.1.3 Driven damped vibration

For a harmonic external force $F(t) = F_0 \cos(\omega t)$ the steady state solution of equation 2.1 is

$$x(t) = x_0 e^{i\omega t}\,. \tag{2.10}$$

In polar form, the complex amplitude x_0 has the absolute value

$$|x_0| = \frac{F_0/k}{\sqrt{\left(1-\left(\frac{\omega}{\Omega}\right)^2\right)^2 + 4\zeta^2\left(\frac{\omega}{\Omega}\right)^2}} \tag{2.11}$$

and phase

$$\varphi = \arctan\left(\frac{2\zeta\left(\frac{\omega}{\Omega}\right)}{\left(\frac{\omega}{\Omega}\right)^2 - 1}\right) \tag{2.12}$$

describing the amplitude and phase response of a damped system with an eigenfrequency Ω which is excited by a harmonic force of frequency ω.

The amplitude and phase response are depicted in Figure 2-2 for different values of ζ. For $\zeta < 1$ (underdamped system), the amplitude has a distinct maximum near the eigenfrequency of the system. This frequency is called the *resonance frequency* and is given by

$$\omega_r = \Omega\sqrt{1 - 2\zeta^2}\,. \tag{2.13}$$

For low damping, the term in the square root can be neglected, *i.e.*, $\omega_r \approx \Omega$. On the other hand, the phase at the resonance frequency is

$$\varphi_r = \arctan\left(\frac{\sqrt{1 - 2\zeta^2}}{\zeta}\right) \tag{2.14}$$

approaching $\varphi_r = \pi/2$ for $\zeta \ll 1$.

From Figure 2-2 it can be seen that the shape of the resonance peak changes with the damping ratio ζ. The sharpness of the peak is described by the quality factor Q which is the ratio between the energy stored in the system E and the energy δE that is lost during each oscillation cycle

$$Q = 2\pi\frac{E}{\delta E} = \frac{\sqrt{1 - 2\zeta^2}}{2\zeta}. \tag{2.15}$$

For small damping ratios ($\sqrt{1 - 2\zeta^2} \approx 1$) the quality factor can be well approximated by

$$Q \approx \frac{1}{2\zeta}. \tag{2.16}$$

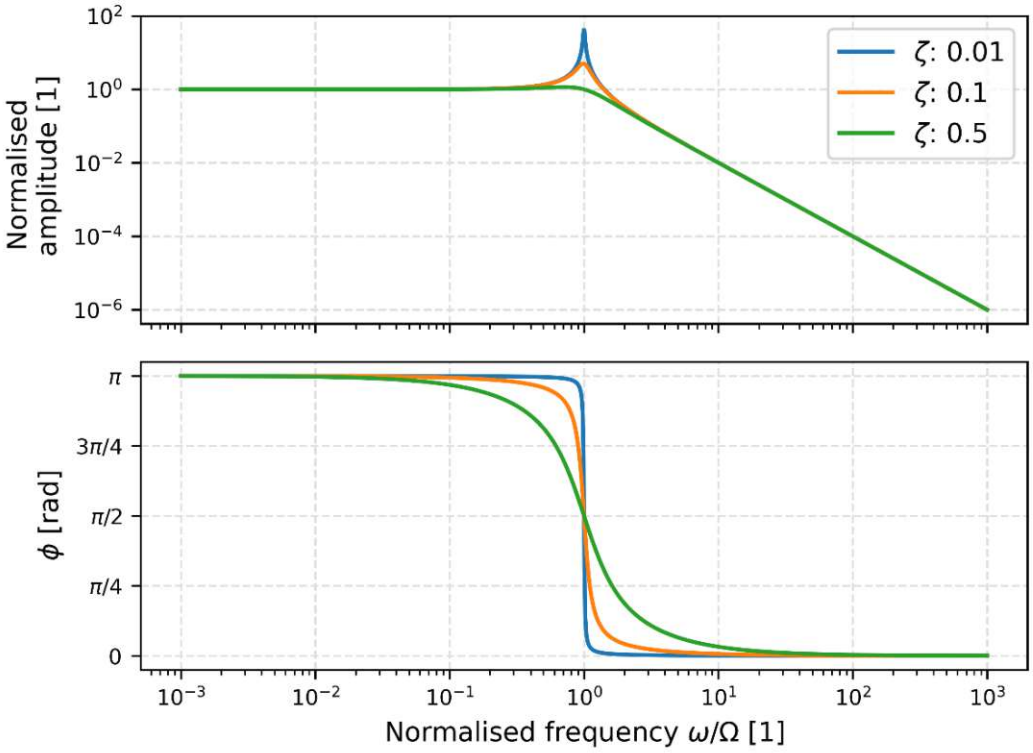

Figure 2-2: Normalized amplitude and phase response of driven-damped system for different values of ζ.

As a measure of the damping of the vibration, the quality factor depends on a variety of internal and external factors, such as the damping properties of the surrounding medium, of the anchor region and cantilever material. An overview of the most relevant damping mechanisms is given in section 2.1.3.

2.1.2 Analytical elastic models for resonant microstructures

Analytical elastic models are used to describe the vibration of resonant microstructures in a continuum mechanical approach. This is in contrast to the description in the previous section, where the oscillating structure is represented by lumped elements, such as springs, dashpots and (point) masses. The continuum mechanical approach allows for the derivation of the shape of vibration, *i.e.,* the mode shape function of the respective eigenmode.

In the following section, the vibration of the structure is assumed to be lossless, hence the kinetic energy of vibration is fully transformed into potential energy stored in the bending of the material and *vice versa*. Two analytical models will be presented: the Euler-Bernoulli beam theory for cantilever beams and the Kirchhoff-Love plate theory for plates. For many relevant structures found in MEMS technology, such as clamped plates, the mode shape function is usually approximated by a suitable function and the resonance frequency is derived by the Rayleigh method, which is briefly explained at the end of this section.

2.1.2.1 Euler-Bernoulli beam theory for cantilevered beams

For simple structures such as cantilevered beams, the mode shape function is derived by applying Newton's third law of motion to an infinitesimal small portion of the structure's material [86]. By equalizing all forces, the equation of motion of a vibrating beam is derived:

$$\rho A \frac{\partial^2 u(x,t)}{\partial t^2} + E I_y \frac{\partial^4 u(x,t)}{\partial x^4} = 0\,. \tag{2.17}$$

This equation is known as the *Euler-Bernoulli beam equation* for the displacement $u(x,t)$ of the beam at the position x along its length L. ρ and E are the density and Young's Modulus of the beam material, respectively, A is the cross-sectional area of the beam and I_y represents its second moment of inertia. The solution of this equation is composed of all possible mode shapes $U_n(x)$ and a temporal function $\cos(\Omega_n t)$ with the eigenfrequency of the nth eigenmode Ω_n:

$$u(x,t) = \sum_{n=1}^{\infty} U_n(x)\cos(\Omega_n t)\,. \tag{2.18}$$

The modal part $U_n(x)$ is time-independent and has the general form

$$U_n(x) = a_n \cos(\beta_n x) + b_n \sin(\beta_n x) + c_n \cosh(\beta_n x) + d_n \sinh(\beta_n x) \tag{2.19}$$

for the flexural out-of-plane eigenmodes, with the wavenumber of the nth eigenmode β_n and four coefficients $a_n \dots d_n$ that depend on the boundary conditions, *i.e.*, the clamping of the beam. Inserting equation 2.19 into the equation 2.18 and. 2.17 yields

$$-\rho A \Omega_n^2 u(x,t) + E I_y \beta_n^4 u(x,t) = 0 \tag{2.20}$$

using

$$\Omega_n = \beta_n^2 \sqrt{\frac{E I_y}{\rho A}}\,. \tag{2.21}$$

which is the eigenfrequency of the nth eigenmode of vibration.

To derive the wavenumber β_n for a specific eigenmode, the clamping of the beam must be considered. In the case of a single-sided clamped beam, the boundary conditions for $U_n(x)$ and its derivates at the anchor $x = 0$ and the free end $x = L$ are

$$\begin{aligned} U_n(0) &= \frac{\partial U_n(0)}{\partial x} = 0 \\ \frac{\partial^2 U_n(L)}{\partial x^2} &= \frac{\partial^3 U_n(L)}{\partial x^3} = 0 \end{aligned} \tag{2.22}$$

Applying these conditions to equation 2.19 yields a system of four linear equations with the solutions $\lambda_n = \beta_n L =$ 1.8751, 4.6941, 7.8548, $(2n - 1)\pi / 2$ that satisfy the condition

$$\cos(\lambda_n)\cosh(\lambda_n) + 1 = 0. \tag{2.23}$$

Using the boundary conditions in equation 2.22, the mode shape function of the out-of-plane eigenmodes can be derived as

$$U_n(x) = a_n \left[\cos\left(\lambda_n \frac{x}{L}\right) - \cosh\left(\lambda_n \frac{x}{L}\right) - \frac{\cos(\lambda_n) + \cosh(\lambda_n)}{\sin(\lambda_n) + \sinh(\lambda_n)} \left(\sin\left(\lambda_n \frac{x}{L}\right) - \sinh\left(\lambda_n \frac{x}{L}\right) \right) \right]. \tag{2.24}$$

The remaining coefficient a_n is used to normalize the mode shape function by splitting equation 2.24 into two terms

$$U_n(x) = U_{n,0} \phi_n(x) \tag{2.25}$$

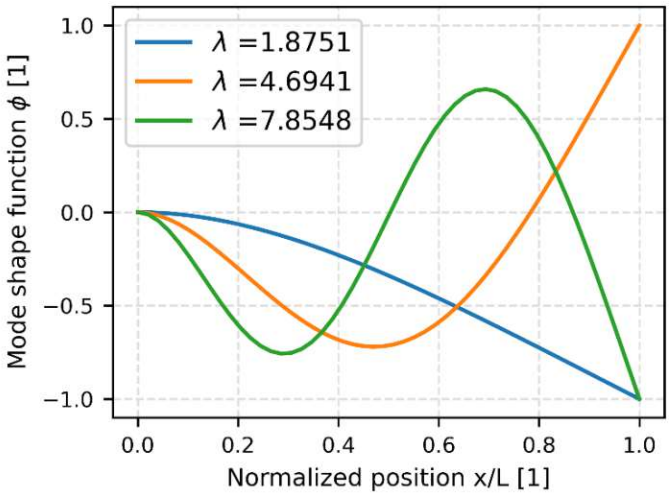

Figure 2-3: The first three eigenmodes for a single-sided clamped cantilever. A normalization scheme $|\phi_n(L)| = 1$ was used.

where $\phi_n(x)$ is the normalized mode shape function.

Figure 2-3 shows a plot of the first three eigenmodes, where a normalization scheme $|\phi_n(L)| = 1$ is used. However, any other normalization is possible since it does not affect the validity of the boundary conditions or equation of motion [85]. For example, the normalization

$$\frac{1}{L}\int_0^L \phi^2(x)dx = 1 \qquad 2.26$$

allows to conveniently calculate the kinetic energy of the cantilever based on its actual mass, rather than using an effective mass, as sometimes used by other authors [87] [88].

2.1.2.2 Kirchhoff-Love theory for two-dimensional bending modes in plates

In contrast to the cantilevered beams in the previous sections, the displacement of plates is described by a function $u(x, y, t)$ which is dependent on the two spatial coordinates x, y. The governing equation is given by the Kirchhoff-Love plate theory of a vibrating rectangular plate

$$D_p \nabla^4 u(x, y, t) - \rho \frac{\partial^2 u(x, y, t)}{\partial t^2} = 0 \qquad 2.27$$

with the flexural rigidity

$$D_p = \frac{ET^3}{12(1 - \nu^2)} \qquad 2.28$$

having a thickness T and the Poisson's ratio ν. An analytical solution as derived in the previous chapter can only be found for the case for the special case of a simply supported plate (supported on both ends

with no fixed anchor, such as, *e.g,* a bridge). Other configurations, such as a fully clamped membrane or a cantilevered plate are much more common in MEMS technology. For such cases, the mode shape function cannot be derived analytically, but must be approximated by a suitable analytical function. In such cases, an approximation for eigenfrequency of the fundamental eigenmode can be readily derived by the *Rayleigh's method* [89]. This method assumes that the total energy in the vibrating system commutes between the kinetic energy stored in the movement of the plate and the potential energy stored in the elastic bending of the plate material:

$$E_{kin,max} = E_{pot,max} \tag{2.29}$$

Since the kinetic energy scales with the velocity squared

$$E_{kin} \propto \left(\frac{\partial u(x,y,t)}{\partial t}\right)^2 \tag{2.30}$$

and the displacement $u(x,y,t)$ is in the form

$$u(x,y,t) = U(x,y)\cos(\Omega t), \tag{2.31}$$

the maximum kinetic energy can be stated as

$$E_{kin,max} = \max[E_{kin}\{u(x,y,t)\}] = \Omega^2 E_{kin}\{U(x,y)\} \tag{2.32}$$

where $\max\{\cos(\Omega t)\} = 1$ was used. Likewise, the potential energy is given by

$$E_{pot,max} = \max\left[E_{pot}\{u(x,y,t)\}\right] = E_{pot}\{U(x,y)\}. \tag{2.33}$$

Substituting these two expressions into equation 2.29, a general term for the eigenfrequency can be derived as

$$\Omega^2 = \frac{E_{pot}\{U(x,y)\}}{E_{kin}\{U(x,y)\}}. \tag{2.34}$$

As mentioned above, the mode shape function must be approximated by suitable analytical functions. These approximations, together with the set of formulas for calculating the kinetic and potential energy can be found for many relevant configurations in the literature, for example in [90]. Another approach that not only gives the resonant frequency but also the mode shape function is the finite element method (FEM). Using commercially or open-source software packages, even complicated geometries can be analyzed in terms of their vibrational characteristics. A detailed introduction to the finite element method can be found for example in [91].

2.1.3 Damping mechanisms

The quality factor as a measure for damping of the vibration was introduced in earlier in equation 2.15. The total quality factor of a vibrating system depends on a multitude of damping mechanisms

$$Q = \left(\frac{1}{Q_{fluidic}} + \frac{1}{Q_{anchor}} + \frac{1}{Q_{internal}} + \cdots \right)^{-1} \qquad 2.35$$

which are, among others, fluidic losses due to the surrounding medium, anchor losses and energy dissipation inside the material of the vibrating system itself, represented by Q_{fludic}, Q_{anchor} and $Q_{internal}$, respectively [92].

2.1.3.1 Fluidic losses

Vibrating structures interact with the surrounding medium via the dissipation of energy. These so-called fluidic losses can cause substantial damping of the vibration. Even in ultra-high vacuum, the remaining gas molecules cause a measurable change of the structure's resonance characteristics. In a liquid, fluidic losses in the form of viscous damping are usually the dominant energy loss mechanism for microcantilevers, thus defining the total quality factor of the vibrating system [93]. Viscous damping was studied extensively, a well-established model was developed by Sader *et al.* [94]. Based on the latter results, the quality factor of an immersed cantilever can be calculated using

$$Q_{fluidic} = \frac{2\pi\sqrt{1 + Lg_2/m}}{Lg_1/m}\Omega \qquad 2.36$$

with the eigenfrequency Ω, and the mass m and length L of the cantilever. The two coefficients g_1 and g_2 represent the influence of the viscosity and the additional mass of the surrounding fluid that is dragged along during the oscillation, respectively. Both coefficients depend on the "hydrodynamic function", which was derived by Sader *et al.* by analyzing the force exerted on the cantilever beam by the surrounding fluid. Due to the complexity of this function, efforts have been made to use approximations to simplify the application of this function for typically encountered geometries and mode shapes in MEMS devices [95] [96] [97].

The surrounding fluid does not only deteriorate the quality factor of vibration, but also increases the total mass of the oscillating system by the fluid that is dragged along in phase during oscillation [98]. This leads to a significant reduction of the resonance frequency and has a dramatic impact on the usability of microcantilevers for sensing applications in liquid environments. The performance of microcantilevers in a liquid environment used for mass sensing purposes is discussed extensively in chapter 4.

2.1.3.2 Anchor losses

In a typical manufacturing process, the microcantilever is formed from the bulk material using various etching or deposition techniques. One side remains clamped to the substrate, which enables a fraction

of the vibration energy to leave the resonator and to be transferred to the substrate via this “anchor”. This energy exchange occurs in form of elastic waves, which, depending on the cantilever shape, mode type and anchor design, account for a considerable part of the total energy loss [99]. Due to the complexity of this process, only approximations for the quality factor because of clamping losses can be found in literature [100] [101] [102]. As a general design guideline, the thickness of the substrate should be considerably larger than the thickness of the microcantilever. This is especially true for plate-like cantilevers where the width of the clamping region is large relative to the length of the structure. An interesting approach of reducing the clamping losses was shown by Pfusterschmied *et al.*, who confined the clamping to regions of zero vibrational amplitude [103]. Doing so, the overall quality factor of a submerged microplate resonator was increased by 6% in comparison to a conventional anchor design.

2.1.3.3 Internal losses

Multilayer cantilevers, *i.e.*, cantilevers composed of several functional layers, experience considerable damping in the form of friction losses. For example, piezoelectrically driven cantilevers consist of a piezoelectric layer with electrodes and often several passivation layers in addition to the supporting structure. During vibration, energy is dissipated in each of these layers due to crystal defect dislocations, grain boundary slipping in the metal electrode material or phase boundary slipping at the interface between two layers [104]. If such a cantilever is used as a sensor, a functionalization layer is often applied to the surface, significantly contributing to the total dissipated energy [105]. This effect must be considered especially in the design of resonant mass sensors since the degradation of the quality factor during operation also affects the accuracy when determining the resonance frequency.

Even in the absence of any frictional losses, fundamental energy losses occur within the resonator material during oscillation. When a cantilever undergoes bending, the resulting strain causes either heating (compression) or cooling (tension) inside the cantilever material. For the fundamental out-of-plane mode, one side of the cantilever experiences compression while the opposite side is tensioned. The resulting temperature difference between the two sides causes a heat flow that is fed by the vibrational energy of the cantilever. This phenomenon is called thermoelastic damping and is often the limiting damping mechanism when designing high-Q mechanical resonators [106].

2.1.4 Mass detection using resonant microstructures

In section 2.1.1 it was shown that the resonance frequency of a microcantilever is dependent on the oscillating mass. However, this mass does not only consist of the mass of the cantilever material, but also includes any adsorbed mass on the cantilever surface. An important application of oscillating microcantilevers is therefore the detection of adsorbed material by measuring the mass-induced shift of the cantilever-related resonance frequency from its initial "non-loaded" starting point. Mass detection using resonant microstructures was proposed more than twenty years ago by Cleveland *et al.* and efforts have been made to reduce the detection limit down to the mass of single molecules [107] [108] [109]

[110]. This section introduces the principle of resonant mass detection by defining the basic terminology and deriving the formulas to calculate the mass-induced resonance frequency shift for two scenarios: the adsorption of a point mass and an evenly distributed layer of matter.

2.1.4.1 Definitions

When it comes to the terminology used in publications on resonant mass sensors, many different and sometimes conflicting definitions of the basic quantities can be found. The reason for this often lies in the research focus of the publishing group, which adopts the terminology of their respective field. It is therefore necessary to define the basic quantities used in this thesis:

The **mass responsivity** is the resonance frequency shift $\partial\omega$ ($= \partial\Omega$ for slight damping) per unit mass change ∂m and is given in Hz/ng:

$$\mathcal{R} = \frac{\partial\Omega}{\partial m}. \tag{2.37}$$

In this section weak damping is assumed, therefore, the resonance frequency shift $\partial\omega$ can be approximated by the shift of the eigenfrequency $\partial\Omega$. In some cases, the inverse of equation 2.37 is defined as the mass responsivity, *i.e.*, the amount of mass needed to cause a resonance frequency shift of 1 Hz. Both definitions are used in this thesis and can be differentiated unambiguously by the units. It is important to mention that the mass responsivity is a linearization of the frequency response of the cantilever to the added mass and dependent on the total mass of the system. However, ensuring that the added mass is much smaller than the cantilever mass ($\Delta m \ll m_c$), the mass responsivity can be assumed to be constant.

The **limit of detection (LOD)** also referred to as **sensitivity** is the lowest detectable mass change and is dependent on the ratio of the smallest measurable resonance frequency shift $\Delta\Omega_{min}$ and the mass responsivity:

$$\mathrm{LOD} = \frac{\Delta\Omega_{min}}{\mathcal{R}}. \tag{2.38}$$

The LOD therefore not only depends on the microcantilever's properties, but also on the accuracy of the measurement setup to determine the resonance frequency.

2.1.4.2 Adsorption of a single point mass

If a single point mass Δm is added to the cantilever surface, the resulting resonance frequency shift depends not only on the amount, but also on the exact position of the mass (Figure 2-4a). It is intuitive that the same mass has a greater effect on the resonant frequency when deposited in areas of high vibrational amplitude than in those of very low amplitude. In the following section, the formula for the mass-induced shift in resonance frequency will be derived for an arbitrary position on the cantilever surface.

As discussed in section 2.1.2 an ideal resonant structure is characterized by the continuous commutation of kinetic energy E_{kin} and potential energy E_{pot} stored in the bending of the resonator material. Under the assumption that the added point mass Δm is very small in comparison to the mass of the cantilever m_c, the mode shape does not change when adding the mass to the surface and hence the potential energy is the same as in the unloaded case. The energy balance for a mass-loaded cantilever therefore is

$$E_{pot} = E_{kin} + E_{kin,\Delta\mathrm{m}} \tag{2.39}$$

with the kinetic energy of the point mass $E_{kin,\Delta\mathrm{m}}$. The kinetic energy of the cantilever can readily be expressed as

$$E_{kin} = \frac{1}{2} A^2 \Omega_{\Delta\mathrm{m}}^2 m_c \tag{2.40}$$

with the vibrational amplitude A and the resonance frequency of the mass-loaded cantilever $\Omega_{\Delta m}$. Likewise, the kinetic energy of the point mass is given by

$$E_{kin,\Delta m} = \frac{1}{2} A^2 \Omega_{\Delta\mathrm{m}}^2 \Delta m \phi^2(x_{\Delta m})\,. \tag{2.41}$$

The position dependence of the vibrational amplitude is considered by the value of the normalized mode shape function $\phi(x)$ at the position of the particle $x_{\Delta m}$ on the cantilever surface. Note that the normalization $\frac{1}{L}\int_0^L \phi^2(x)dx = 1$ is chosed, as described in section 2.1.2.1.

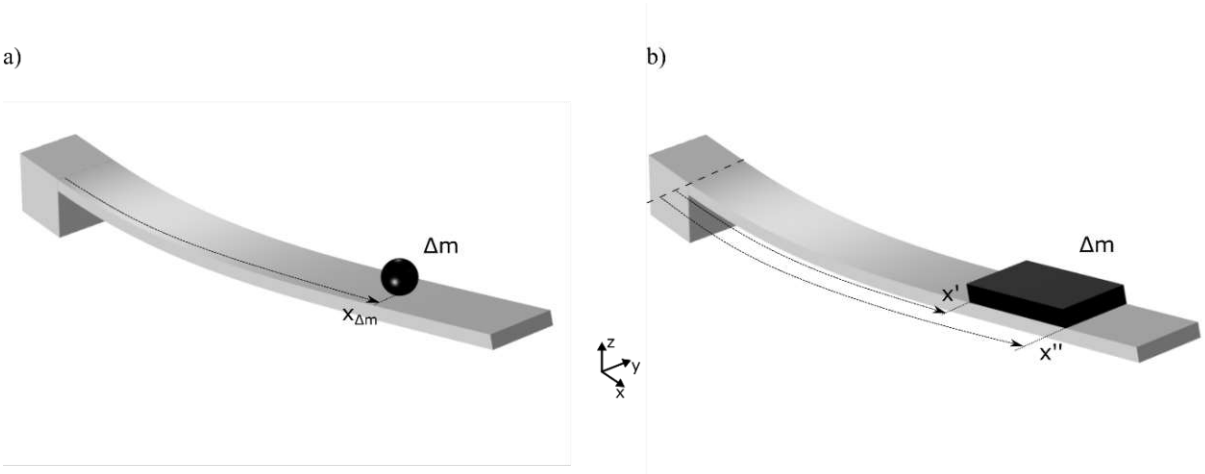

Figure 2-4: Visualisation of mass-loaded cantilevers in the case of (a) a point mass Δm at the position $x_{\Delta m}$, (b) a distributed mass Δm between x' and x'' along the length of the cantilever.

The potential energy stored in the material bending remains unchanged upon addition of the point mass (*i.e.*, the mode shape does not change due to the particle) and hence equals the kinetic energy of the cantilever in the unloaded case:

$$E_{pot} = \frac{1}{2} A^2 \Omega^2 m_c \qquad 2.42$$

with the resonance frequency of the unloaded cantilever Ω. Equations 2.40 – 2.42 are substituted into equation 2.39 and rearranged, resulting in an expression for the resonance frequency of the mass-loaded cantilever

$$\Omega_{\Delta m} = \frac{\Omega}{\sqrt{1 + \frac{\Delta m}{m_c} \phi^2(x_{\Delta m})}}. \qquad 2.43$$

Since $\Delta m \ll m_c$ equation 2.43 can be rewritten by means of a Taylor series expansion ($1/\sqrt{1+x} \approx 1 - x/2$):

$$\Omega_{\Delta m} = \Omega \left(1 - \frac{1}{2} \frac{\Delta m}{m_c} \phi^2(x_{\Delta m})\right). \qquad 2.44$$

The mass responsivity at an arbitrary point $x_{\Delta m}$ on the cantilever surface is therefore given by

$$\mathcal{R}(x_{\Delta m}) = \frac{\Omega_{\Delta m} - \Omega}{\Delta m} = \frac{\Delta \Omega}{\Delta m} = -\frac{1}{2} \frac{\Omega}{m_c} \phi^2(x_{\Delta m}). \qquad 2.45$$

This equation confirms the statement in the beginning paragraph of this section: The identical mass Δm leads to a higher resonance frequency shift in areas of high amplitude (large $\phi(x)$) compared to those of low amplitude. In the limiting case $\phi(x) = 0$ the mass is located on a nodal line and the resulting resonance frequency shift is zero.

2.1.4.3 Distributed mass on the cantilever surface

In most practical cases the adsorbed mass is distributed homogeneously across the cantilever surface rather than occurring as a point mass at a specific location. This is due to the design of most microcantilever sensors, in which a functionalized layer promotes the accumulation of specific particles on the cantilever surface. Consider a microcantilever of length L and width W that is coated on one side with a functional layer in between the x-coordinates x' and x'' (Figure 2-4b). For this example, the influence of the functional layer on the mechanical properties of the cantilever is neglected, *i.e.*, it is assumed to have zero mass and stiffness. The accumulated particles form an evenly distributed layer on the cantilever surface with a total mass of Δm. To calculate the resulting resonance frequency shift due to the presence of these particles, equation 2.45 is rearranged and integrated along the extension of the functionalized layer:

$$\Delta\Omega = -\frac{1}{2}\frac{\Omega}{m_c}\frac{\Delta m}{x'' - x'}\int_{x'}^{x''} \phi^2(x)\, dx\,. \qquad 2.46$$

For a fully coated cantilever ($x' = 0, x'' = L$), equation 2.46 results in

$$\Delta\Omega = -\frac{1}{2}\frac{\Delta m}{m_c}\Omega \qquad 2.47$$

because

$$\frac{1}{L}\int_{0}^{L} \phi^2(x)\, dx = 1 \qquad 2.48$$

as given in equation 2.26.

2.1.5 Non-conventional eigenmodes in MEMS resonators

So far, only flexural out-of-plane (OOP) eigenmodes, where the displacement solely varies along the length of the cantilever, were considered. These eigenmodes are predominantly used in cantilevers where the length exceeds the width and thickness significantly. However, these modes experience significant viscous damping when immersed in a liquid (cf. section 2.1.3.1) what limits their applicability as resonant mass sensors in liquid environments substantially [111]. To mitigate the fluidic impact on the cantilever vibration, other eigenmodes were studied for sensing purposes in liquid environments. Probably best known is the in-plane eigenmode, which undergoes a lateral oscillation parallel to the surface of the cantilever. Using this eigenmode, the quality factor of an immersed microcantilever can be improved by orders of magnitude compared to the OOP-modes [112] [113] [114] [115]. For practical applications, however, the in-plane mode has a major drawback: Especially for relatively wide structures, like plate-like cantilevers, the lateral vibration leads to a very high stiffness of the system and hence small amplitude of vibration, which renders both the excitation and the detection of the resonant frequency difficult [116]. Apart from these one-dimensional eigenmodes, more complex mode shapes, where the vibrational amplitude depends not only on the position along the length but also on the position along the width of the cantilevers, were studied. One prominent example is the torsional eigenmode, showing a rotatory vibration along the length of the cantilever. It was shown that the mass responsivity of this class of modes exceeds the performance of the OOP-modes by about an order of magnitude [117] [118].

While investigating alternative eigenmodes suitable for sensing applications in liquids, the special class of so-called *roof tile-shaped eigenmodes* was discovered [119] [120] [121]. These two-dimensional eigenmodes show additional nodal lines along the length of the cantilever and are named according to Leissa's notation for flexural eigenmodes: two numbers represent the nodal lines along the width and length of the resonator, respectively [90]. Following this notation, the fundamental OOP-mode is called

10-mode, while the roof tile-shaped modes are called 1X-modes, where X is the number of nodal lines along the width of the cantilever. The fundamental roof tile-shaped mode is therefore called 12-mode. Figure 2-5 shows a visualization of the roof-tile shaped eigenmodes up to 8th order. Compared to the OOP-eigenmodes, rather than being concentrated in the anchor region, the mechanical strain is distributed across the whole cantilever surface, what predestines the usage of a piezoelectric actuation and sensing scheme. This actuation scheme will be presented in detail in section 2.2.

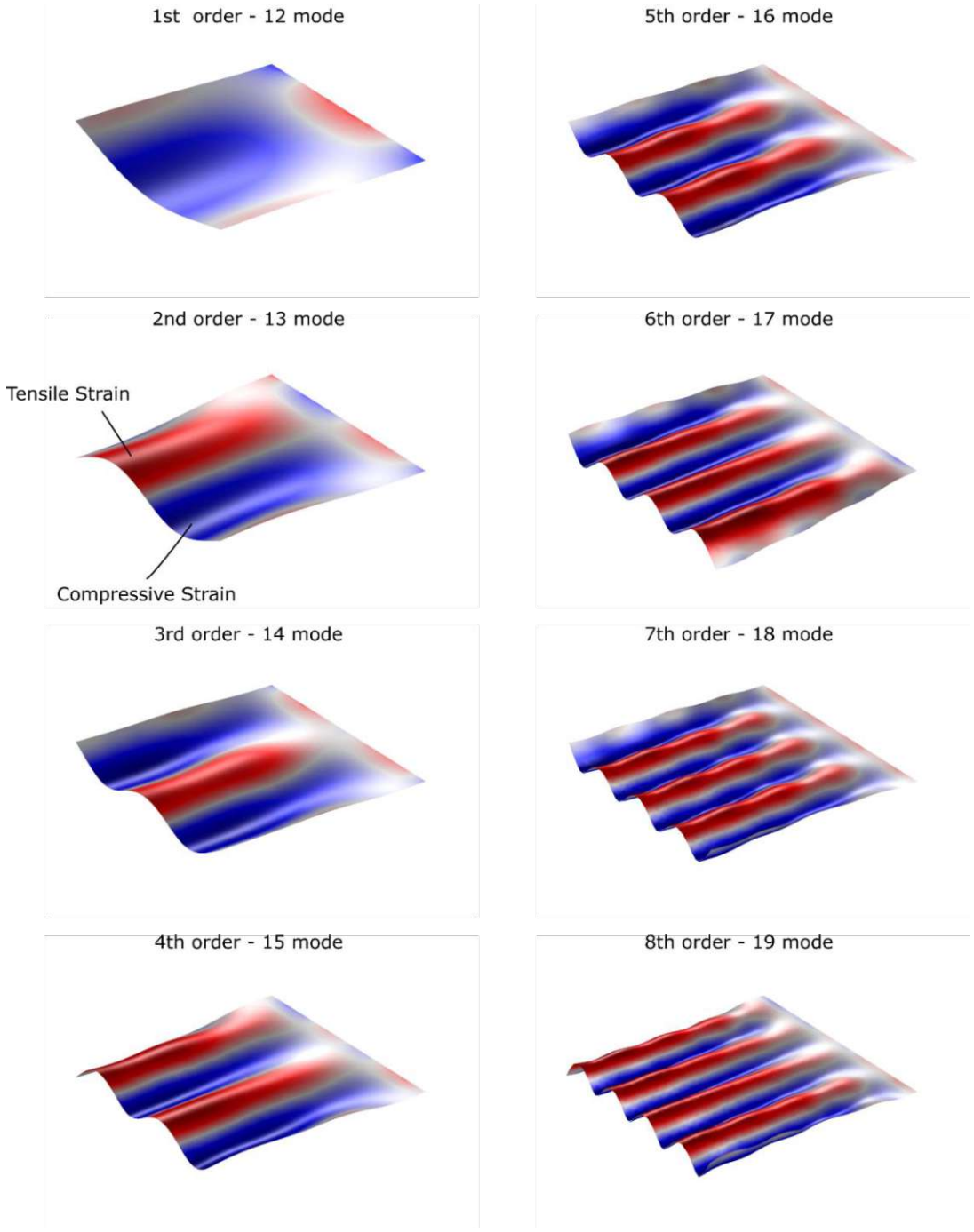

Figure 2-5: Visualization of the roof tile-shaped eigenmodes for a plate-like cantilever up to the 8th order. The colours indicate the strain: red - tensile, blue - compressive.

The resonance frequency of the roof tile-shaped eigenmodes can be approximated by equation 2.21 using the plate modulus $E/(1-\nu^2)$ to account for the transverse strain as expressed by the Poisson's ratio ν of the cantilever material:

$$\Omega_n = \frac{\lambda_n^2}{4\pi}\frac{T}{W^2}\sqrt{\frac{E}{3\rho(1-\nu^2)}} \qquad 2.49$$

Here, the eigenvalues λ_n as derived for a free-free clamping condition is used, which is a valid approximation considering the shape of the roof tile-eigenmodes perpendicular to the length of the cantilever. Equation 2.49 shows that the roof tile-shaped eigenmodes appear at high frequencies for cantilevers with low width W, while their resonance frequency is substantially lower for wide structures where $W \gg T$. Because of this, most structures that utilize the roof tile-shaped eigenmodes are designed to have lower length-to-width ratios, such as plate-like cantilevers.

The roof tile-shaped modes were studied extensively due to their extraordinary performance in liquid environment. Kucera *et al.* presented a study of a piezoelectrically-driven microcantilever (2524 x 1274 x 90 µm^3) driven in the fundamental roof tile shaped mode (12-mode), immersed in deionized water [120]. Compared to the OOP-mode, an increase in Q factor up to a factor of five was measured. Even for high viscosity liquids, such as the viscosity standard D500 ($\eta \approx 730$ mPa·s at 20°C), the fundamental roof tile-shaped mode was successfully excited and detected using the integrated piezoelectric transducer, showing the outstanding performance of this eigenmode when used in a liquid environment. When exploiting higher order roof tile-shaped modes, even higher Q factors can be achieved. Kucera *et al.* studied the roof tile-shaped modes up to the 10th order (1B-mode) and measured a Q factor of 366 in deionized water at a resonance frequency of approximately 3.5 MHz [121]. Because of the complex mode shape, the electrode designs for piezoelectric excitation and detection of the cantilever oscillation had to be adapted to the specific mode shape by patterning, what is discussed later in section 2.2.3.

Because of its superior performance in liquid environments, the application of the roof tile-shaped eigenmode for liquid sensing applications was studied extensively [122] [123]. One of the most prominent applications of microcantilever sensor is the measurement of rheological properties, such as density and viscosity of liquids. By monitoring the resonance frequency and Q factor of the cantilever oscillation, changes in liquid properties can be detected with high precision requesting only a very small sample volume. Different calibration schemes were investigated and mean deviations as low as 0.4% for the density measurement and 2.8% for the viscosity measurement were obtained compared to standard measurements with a commercial density-viscosimeter [7]. The very high sensitivity to any changes in viscosity or density allows for the utilization of roof tile-shaped eigenmodes in many industrial applications such as the monitoring fermentation processes or the detection of fuel dilution in lubricating oil systems [9] [124] [125] [126]. Recently, the roof tile-shaped eigenmode impressively showed its performance by successful measuring the viscosity of bitumen samples with a dynamic

viscosity of up to 64000 mPa·s [127]. This allows for structural monitoring of road asphalt pavements to detect early stages of deterioration due to bitumen oxidation processes.

Besides their practical application, the roof tile-shaped eigenmodes were studied theoretically to gain better understanding of the oscillatory properties of submerged plate-like microcantilevers. It was shown that the established analytical models cannot be applied to this eigenmodes because of the complex fluid flow around the structure [128]. Computational fluid dynamics and fluid structure interaction models were implemented using FEM, giving first insights on the pressure and velocity distributions of a plate-like microcantilever oscillating in a liquid environment in the roof tile-shaped eigenmode [129] [130]. Additionally, the influence of the mode order on the responsivity and sensitivity for rheological measurement was investigated [131]. It was shown that the damping of the oscillation is substantially increased for higher order modes due to the dissipation of acoustic radiation caused by the compressibility of the fluid [132].

Due to their outstanding performance, the roof tile-shaped eigenmodes will be utilized in this thesis for the detection of particles in viscous liquids such as lubricating oil. A detailed explanation of the sensor design and measurement procedures will be given in chapter 4 of this thesis.

2.2 Piezoelectricity

2.2.1 The piezoelectric effect

The piezoelectric effect was discovered in the late 19th century by the brothers Pierre and Jacques Curie. While experimenting with Tourmaline crystals, they found that an electric polarization and hence charge is generated on the crystal surface when it is subjected to mechanical stress. Likewise, it was found that certain crystals deform when they are exposed to an electric field [133]. The discovery of the piezoelectric effect laid the foundation for many everyday applications such as sensors and actuators in industry, medical technology and consumer electronics.

The piezoelectric effect can be divided into three types, depending on the direction of the applied force and the resulting electric polarization:

1. Transversal piezoelectric effect: Electric polarization is perpendicular to the applied force.
2. Longitudinal piezoelectric effect: The axes of the electric polarization and the applied force are parallel.
3. Piezoelectric shear effect: The electric polarization is perpendicular to the direction of mechanical shearing.

Using the Voigt notation, the piezoelectric effect is expressed by a set of two coupled equations for the strain S and the electric displacement D [134]:

$$S_j = s_{ij}^E \sigma_j + d_{ij} E_i$$
$$D_i = d_{ij} \sigma_j + \epsilon_{ii}^T E_i \qquad 2.50$$

Here, σ_j and E_i are the mechanical stress and electric field strength in the directions j and i, and s_{ij}^E and ϵ_{ii}^T are the i,j-coefficients of the compliance matrix at constant electric field strength and permittivity matrix at constant mechanical stress, respectively. The coupling between the mechanical and electrical domain is provided by the piezoelectric coefficient matrix d (Voigt notation), which is given in pm/V or equivalently in pC/N.

2.2.2 Piezoelectric materials

The piezoelectric effect is based on a shift of the charge centers of positive and negative charge due to a deformation of the unit cell [133]. Without any external force, the centers of positive and negative charge are located at the same position, hence the resulting net polarization is zero. When a force is applied, however, the charge-related symmetry is broken, causing a measurable electric polarization on the surface of the piezoelectric material. Roughly speaking, piezoelectric materials can be divided into three categories: crystals, ceramics, and polymers. The probably best-known piezoelectric crystal is quartz, which is often used as crystal oscillator in timing applications. The crystal structure is an important criterion for the occurrence of the piezoelectric effect. If the elementary cell has an inversion center, *i.e.*, it can be transferred into itself by a reflection at a certain point, no electrical net polarization can occur as a result of deformation. Other important piezoelectric crystals are lithium niobate $LiNbO_3$, zinc oxide ZnO, as well as the ferroelectric materials barium titanate (BTO) and lead zirconium titanate (PZT). However, the latter are usually sintered to polycrystalline ceramics with macroscopic dimensions. After the sintering process, these electroceramics do not possess measurable piezoelectric properties due to the random arrangement of the domains but must be polarized in a strong electric DC field at elevated temperatures. The same applies to piezoelectric polymers, of which the best known is probably polyvinylidene fluoride (PVDF). This material is especially interesting for MEMS applications, because very thin layers can be applied by spin-coating [135].

The piezoelectric material used in this thesis is aluminum nitride (AlN), a wide-bandgap semiconductor (E_g = 6.2 eV at 300 K) material of the class of group III-Nitrides [136]. AlN synthesizes in a wurtzite crystal structure, which is a type of a hexagonal crystal system. The aluminum and nitrogen atoms each form a hexagonal close-packed microstructure, where the nitrogen atoms are located in the tetrahedron gaps between four aluminum atoms. Because of the high electronegativity of the nitrogen, the elementary cell is deformed from its ideal shape with respect to the so-called c-axis causing an electrical polarization along this direction. Compared to other piezoelectric materials, such as PZT, the piezoelectric constants are lower by up to two orders of magnitude, depending on, *e.g.,* the chemical

composition of the PZT and the film morphology. However, its outstanding thermal and chemical resistance compared to PZT makes the application of AlN in harsh environments feasible. Table 2-1 gives an overview of the key properties of AlN for MEMS applications. The most outstanding advantage of AlN compared to any other piezoelectric material is its CMOS (Complementary Metall-Oxide Semiconductor) compatibility, since unlike PZT, it does not contain lead. Additionally, aluminum nitride exhibits piezoelectric properties without a dedicated polarization procedure, reducing manufacturing effort. AlN can be deposited via standard deposition methods, such as reactive sputtering (cf. section 2.3), where the properties of AlN thin films can be adjusted by variation of the deposition parameters [137].

Table 2-1: Key properties of aluminium nitride (AlN) for MEMS applications [138] [139] [140] [141] [142] [143]

Property	Value
Melting point	2500°C
Thermal conductivity	2.85 W/(cm·K)
Thermal expansion coeff.	$5.27 \cdot 10^{-6}$ K^{-1} (c-axis)
Bandgap	6.2 eV
Dielectric constant	8.5
Piezoelectric constants	3.5-5.1 pm/V (d_{33})
	1-1.28 pm/V (d_{31})
Dielectric strength	1.2-1.8 kV/mm
Density	3.23 g/cm^3
Young's modulus	225-243.5 GPa

2.2.3 Piezoelectrically-driven MEMS cantilevers

One of the most important applications for piezoelectric thin films is the actuation of MEMS cantilevers and membranes. Because of their low mechanical deformation when an external electric field is applied, piezoelectric materials are commonly used for dynamic-mode cantilever applications rather than static-mode operation. A thin piezoelectric layer is deposited on the microcantilever and sandwiched between two electrodes. An alternating voltage is applied to the electrodes to excite an electric field in the piezoelectric material. For these applications, the d_{31}-effect is mainly used, where the alternating expansion and contraction of the piezoelectric layer perpendicular to the applied electric field causes a displacement of the cantilever structure. If the frequency of the alternating field is chosen to be at or near the mechanical resonance frequency of the cantilever, the cyclic excitation induces a resonant oscillation of the cantilever structure. By suitable patterning of the electrodes, the excitation of certain mode shapes can be promoted. Figure 2-6 shows a piezoelectrically-driven cantilever with two piezoelectric layers along the length of the cantilever. An optimized excitation scheme for out-of-plane

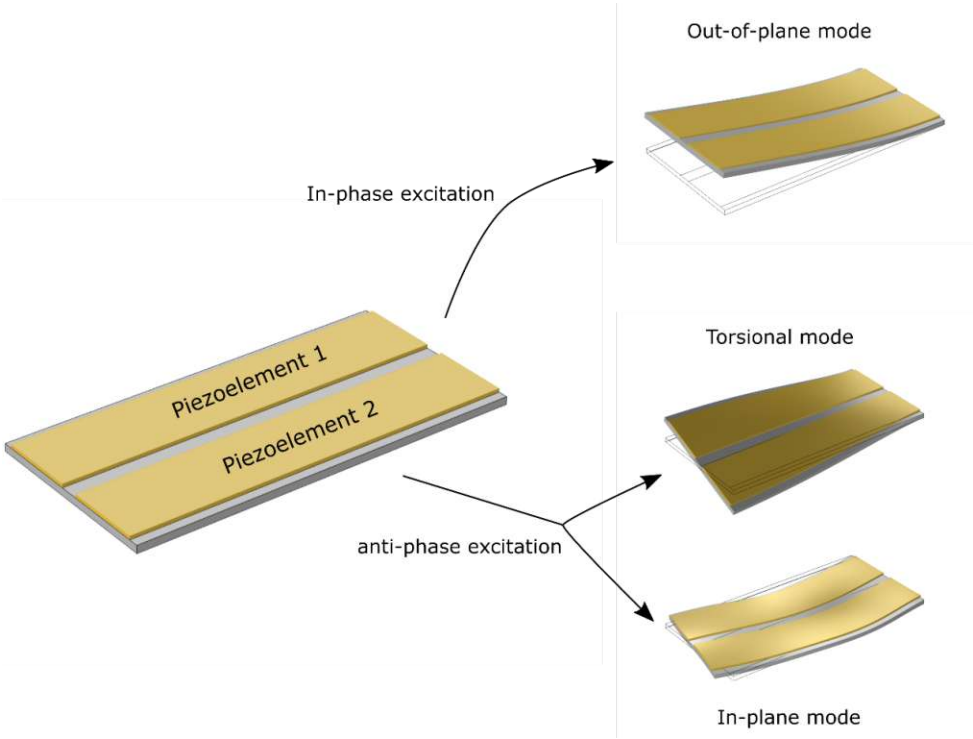

Figure 2-6: Piezoelectrically-driven cantilever with two piezoelectric layers along the length of the cantilever, allowing for an optimized excitation of different modes: in-phase for out-of-plane modes, anti-phase for torsional and in-plane modes

modes is achieved by operating both piezoelectric elements in phase, while for the in-plane and torsional modes an anti-phase excitation is chosen.

Another distinct feature of the piezoelectrical transduction method is the possibility to detect the frequency response of the oscillating cantilever during excitation. The basis for this approach is the Butterworth-van Dyke (BvD) model, which represents the oscillatory system by a lumped element model in the electrical domain (Figure 2-7) [144]. The mechanical resonance phenomenon is modelled by a series resonance circuit, consisting of the motional resistance R_m, the motional inductance L_m and the motional capacitance C_m. Parasitic influences, such as the leakage current across the piezoelectric layer and the capacitance of the electrodes, are represented by the parallel resistance R_p and capacitance C_p, respectively. The electrical impedance of the motional part of the BvD-model is therefore given by

$$Z_m(\omega) = R_m + i\omega L_m - i\frac{1}{\omega C_m} \tag{2.51}$$

with $i = \sqrt{-1}$. The complex admittance of the motional part

$$Y_m(\omega) = \frac{1}{Z_m(\omega)} = \frac{\omega C_m}{\omega C_m R_m + i(\omega^2 L_m C_m - 1)} \tag{2.52}$$

is then added to the complex admittance of the parasitic elements

$$Y_p(\omega) = \frac{1}{R_p} + i\omega C_p \tag{2.53}$$

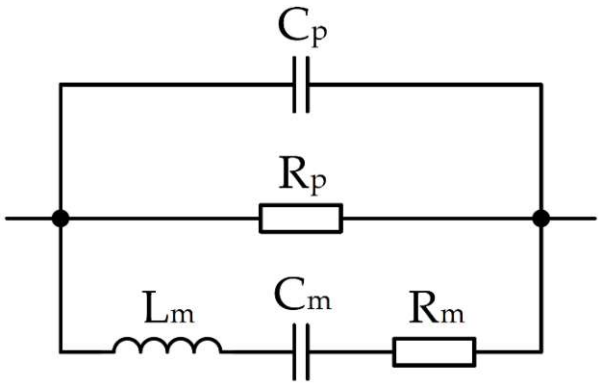

Figure 2-7: Butterworth-van Dyke (BvD) equivalent circuit to model the dynamic behaviour of a piezoelectrically-driven oscillating cantilever. Lm-Cm-Rm are the motional branch to model the resonance behaviour while Cp and Rp represent the capacitive and resistive losses across the piezoelectric material, respectively.

what results after a conjugate complex expansion in the final expression for the complex admittance of the BvD-model

$$Y(\omega) = G(\omega) + iB(\omega) \tag{2.54}$$

consisting of the frequency-dependent conductance $G(\omega)$ and susceptance $B(\omega)$

$$G(\omega) = \frac{1}{R_p} + \frac{\omega^2 C_m^2 R_m}{\omega^4 L_m^2 C_m^2 + \omega^2 (C_m^2 R_m^2 - 2L_m C_m) + 1} \tag{2.55}$$

$$B(\omega) = \omega C_p - \frac{\omega C_m (\omega^2 L_m C_m - 1)}{\omega^4 L_m^2 C_m^2 + \omega^2 (C_m^2 R_m^2 - 2L_m C_m) + 1}. \tag{2.56}$$

By measuring the complex admittance during the excitation of the cantilever oscillation, it is possible to fit equations 2.55 and 2.56 to the measurement data. Doing so, the values of the motional branch R_m-L_m-C_m can be extracted and used to calculate the mechanical resonance frequency of the cantilever and the Q factor of oscillation:

$$f_r = \frac{1}{2\pi} \frac{1}{\sqrt{L_m C_m}} \tag{2.57}$$

$$Q = \frac{1}{R_m} \sqrt{\frac{L_m}{C_m}}. \tag{2.58}$$

As described above for the excitation, the electrode shape also has a strong influence on the readout of the oscillation parameters, which will be shown using the example of the 2nd order (13) roof tile shaped mode. If a single electrode is used as shown in Figure 2-8a, the surface electric charges generated in the stretched and compressed regions on each side of the piezoelectric element compensate each other. The resulting electrical signal would therefore be zero. If the shape of the electrodes, as shown in Figure

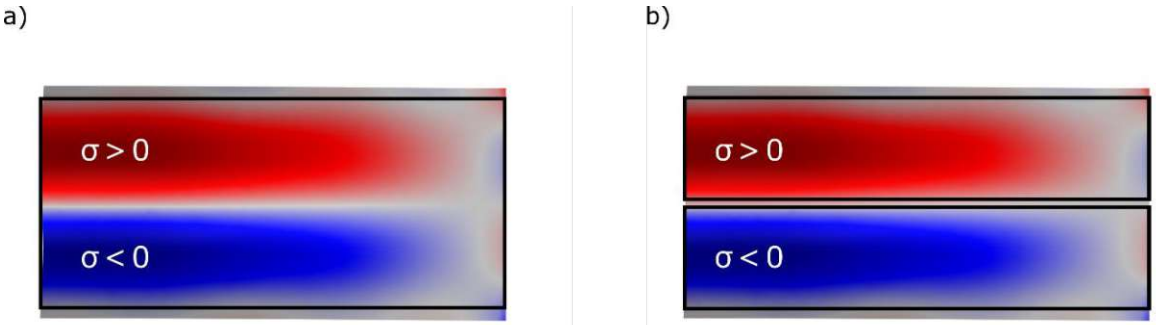

Figure 2-8: Comparison of single and patterned electrodes (depicted as black outline) for piezoelectric readout: (a) using a single electrode, the surface electric charges σ cancel each other out, (b) the patterned electrodes each capture mainly positive or negative surface electric charges σ.

2-8b, is adjusted to include only areas of positive or negative strain, respectively, the electrical output of the mode of interest is maximized.

Therefore, in this thesis, a tailored stripe electrode pattern is used to selectively excite and detect the roof tile-shaped eigenmode under study investigated in the piezoelectrically-driven microcantilevers within this study. An in-depth discussion of the used electrode designs is given in [145].

The microcantilevers used in this thesis were electrically characterized with impedance analyzers from Agilent (4294A precision impedance analyzer) and from Zurich instruments (MFIA impedance analyzer). Both instruments allow simultaneous excitation of the cantilever and measurement of the frequency-dependent conductance in a wide frequency range with a frequency accuracy of 1 mHz and even below. The manufacturers state a basic impedance accuracy of well below ±0.1%, which is more than sufficient for the characterization of the cantilevers used in this thesis. For further information regarding functionality and sensitivity the reader is referred to the user manuals provided by the manufacturers [1,2].

2.3 Fabrication techniques for MEMS sensors

In this section, the techniques used for fabricating the MEMS sensors in this thesis are explained. The section begins with an introduction of commonly used substrates and substrate-structuring processes, followed by deposition and patterning techniques for thin films. Finally, the dicing and packaging processes for the finished devices are explained.

2.3.1 Substrates and substrate-structuring techniques

Silicon-on-insulator (SOI) wafers are commonly used as substrate material in MEMS technology. These wafers consist of a layered structure, where a thin layer of silicon oxide (buried oxide, BOX) is

[1] Keysight (formerly Agilent) 4294A: https://www.keysight.com/at/de/product/4294A/precision-impedance-analyzer-40-hz-to-110-mhz.html (accessed 03. May 2024)
[2] Zurich Instruments MFIA: https://www.zhinst.com/europe/de/products/mfia-impedance-analyzer (accessed 05. May 2024

sandwiched between two monocrystalline silicon layers. This type of wafer stems from the microelectronic sector, where it is used to fabricate high speed and low power semiconductor devices with low stray capacitance, due to excellent electrical insulation of the BOX to the bulk silicon [146]. One silicon layer is called *device layer*, as it is used to fabricate the devices, while the other layer provides mechanical stability and is therefore called *handle layer*. The MEMS industry uses this type of wafer, because of its inherit advantages in the substrate patterning process. The BOX-layer acts as natural etch barrier for commonly used dry etching processes, such as deep reactive ion etching (DRIE), to achieve well defined device geometries.

In the DRIE-process, the substrate material is cyclically exposed to a sulfur hexafluoride (SF_6) and octafluorocyclobutane (C_4F_8) plasma [147]. The former causes combined chemical-physical removal of silicon by the reactive ions, while the C_4F_8 plasma causes passivation of the exposed silicon. When switching back to the SF_6 gas, the impacting ions break up this passivation layer at the bottom of the targeted structure, while the sidewalls remain protected from the subsequent chemical etching attack. By repeating this process, three-dimensional structures with high aspect ratios and near-vertical sidewalls can be manufactured. When applying this process to a SOI-wafer, the buried oxide acts as natural etch barrier because of the very low etch rates compared to monocrystalline silicon (selectivity approx. 100:1) [148] [149]. In MEMS technology, this allows the device geometry to be precisely controlled by choosing the thickness of the device layer of the SOI wafer equal to the desired thickness of the devices, while the length and width are defined by the etching process. Structured photoresists are used as masking during the DRIE process (see below). In this work, DRIE etching was used for defining the device geometry and etching the handle layer before releasing the cantilevers.

Another important process for substrate patterning is etching of silicon oxide by hydrofluoric acid (HF) [148]. This process follows the reaction equation

$$SiO_2 + 6HF \rightarrow H_2SiF_6 + 2H_2O \ , \qquad 2.59$$

where SiO_2 is converted to a soluble complex salt at a high rate. This etching process was used in this thesis to release the cantilevers by removing the BOX-layer.

2.3.2 Deposition and patterning of thin films

In addition to substrate patterning, MEMS technology also utilizes processes for depositing and structuring thin films. These thin films serve different purposes. On one hand, metal thin films are mostly used for contacting the devices, while functional thin films, such as aluminum nitride, are used for actuation and/or readout of the MEMS devices. On the other hand, non-conductive layers are used to electrically isolate the devices and to provide protection from environmental influences. In this subsection, the most important processes for the deposition of such thin films and their patterning by photolithography are described.

For the deposition of metal thin films, physical vapor deposition (PVD) techniques are commonly used [150]. In these processes, source material is evaporated by means of a physical process. A commonly used technique is thermal evaporation, where metal is heated in an ultra-high vacuum by an electric current or an electron beam in order to transfer it to the gas phase. Because of the vacuum conditions, the metal vapor can migrate unobstructed to the opposing substrate, where it condenses as a thin film. The advantages of this technique are the high deposition rates, the high layer quality due to low residual gas incorporation, and the low mechanical stress on the substrate material. However, since ultra-high vacuum conditions and thus long pump-down times are required for a high-quality vapor deposition process, this method is characterized by a relatively long process time. Additionally, due to the low kinetic energy of the impinging atoms (below 1 eV), adhesion problems of the deposited layers may occur. This can usually be avoided by first depositing a reactive metal such as titanium or chromium to serve as an adhesive layer.

Another PVD process which can also be used to deposit semiconductors and alloys, is sputter deposition. In this process, the substrate is located underneath a solid target made of the desired film material. A plasma is ignited between these two bodies (usually an inert gas, such as argon), from which ions are accelerated towards the target. Individual atoms are ejected from the target by the ion bombardment and condense on the opposing substrate material. Since the target atoms are removed by the impinging particles, metals, alloys and other compounds can be deposited close to the original composition in the target even when consisting of elements with a strong difference in melting points. If a reactive gas is used instead of inert gas, chemical reactions with the ejected target atoms occur, which enables the deposition of compound thin films. In this thesis, reactive sputtering of an aluminum target using a nitrogen plasma was applied to deposit piezoelectric aluminum nitride thin films.

Chemical vapor deposition (CVD) techniques rely on chemical reactions of gaseous precursors on the substrate surface for the deposition of thin films [151]. While it is also possible to deposit metals using CVD, it is mainly used to fabricate non-metallic thin films such as silicon carbide, silicon nitride and silicon oxide. For this purpose, precursor gases are directed onto the heated substrate, where they decompose or react with the surface. To reduce the thermal stress on the substrate, plasma-enhanced vapor deposition (PECVD) was developed where the energy required for the chemical reaction is (partially) provided by a plasma. In this thesis, PECVD was used to deposit silicon nitride passivation layers on the cantilevers.

In most cases, full-surface coverage is not desired, but the thin film should be patterned. An example are the stripe electrodes as depicted in Figure 2-6. The thin film is either etched after deposition or patterned by means of a lift-off process. For both methods, photolithography is used, where thin photosensitive polymers (photoresist) are spun onto the substrate and patterned by suitable UV-light exposure [152]. The desired pattern is contained on a glass mask, which is placed on or above the resist-covered substrate prior to the UV-exposure. Depending on the reaction initiated by the UV light,

photoresists are grouped into three fundamental categories: If it becomes soluble for alkaline developer fluids through exposure to UV light, it is referred to as a positive resist. The opposite behavior is found in negative resists. Both types of photoresist are mainly used for etching processes. A special type of photoresists is the image reversal resist. After initial exposure, the image reversal resist behaves like a positive resist, however, an additional temperature step (reversal bake) causes the exposed areas to become insoluble again. By flood exposure of the entire substrate, the previously unexposed areas become soluble and leave negative flanks after removal. This resist pattern can now be used for the lift-off process, which allows vapor-deposited metal layers to be structured without the need of an etching step. After the metal is deposited over the entire surface, the resist mask is removed with a solvent, partially lifting off the metal layer from the substrate. As a result, only the desired metal pattern remains on the substrate.

2.3.3 Dicing and packaging

After fabrication, the devices must be separated from the wafer, this process is referred to as dicing. For this purpose, the wafer is cut with a special diamond-coated saw blade with a thickness of a few tens of micrometers. A thick layer of protective resist prevents contamination of the finished devices with sawdust during this process. The separated devices are then glued into suitable packages to facilitate handling and electrical interconnection. In this thesis, ceramic 24-pin dual in-line packages (DIP) were used because of their high thermal and chemical resistance. The individual pins were wire bonded to the electrical contacts on the MEMS chip. Both ball-wedge and wedge-wedge processes were used for this purpose.

2.4 Characterization techniques for MEMS structures

2.4.1 Laser-Doppler Vibrometry (LDV)

Laser-Doppler Vibrometry (LDV) is a method for the optical analysis of vibrating structures. This method is based on the Doppler shift, *i.e.*, the change in frequency of a coherent laser beam when it is reflected by a moving body. If the body moves towards the light source, the frequency of the reflected beam increases and *vice versa*. The frequency changes therefore contain the motion information of the examined object and allow the determination of the oscillation frequency and amplitude. LDVs are based on an interferometer in which a laser beam is split into two arms via beam splitters. The reference beam with a fixed path length is directed directly to a photodetector, while the measuring beam is focused on the object under investigation, from which it is scattered and reflected into the optics of the LDV. The reflected measuring beam is superimposed on the reference beam in the LDV. The result is a frequency modulated signal from which the vibration information of the examined body can be extracted. The time-dependent modulated signal is typically Fourier transformed, so that the frequency spectrum is obtained. Scanning Laser-Doppler vibrometers do not measure only one point on the sample surface, but scan a predefined area, creating a frequency spectrum for each point. By combining these

individual spectra, it is possible to reconstruct a displacement profile of the sample surface. In MEMS technology, this allows to visualize the eigenmodes of resonators.

2.4.2 Thermoelastic excitation

As discussed in section 2.2.3, integrated piezoelectric layers can be used for the actuation of resonant microsystems. However, for passive structures, such as bare silicon cantilevers, other actuation techniques must be employed. For low frequencies (typically below 1 MHz), the cantilever can be glued on a commercially available piezo actuator to excite the oscillation by actuation of the cantilever base substrate. Besides the relatively low maximum actuation frequency, another disadvantage of this method is the appearance of spurious modes and undefined oscillatory behavior caused by the crosstalk of the resonant modes of the cantilever, the cantilever substrate, and the piezoelectric actuator. An elegant method to drive passive microsystems, even at high frequencies, is the thermoelastic excitation scheme. The resonator is heated locally by a laser beam, which causes a local expansion of the material. By modulating the power of the laser beam, it is thus possible to excite resonant vibrations of microstructures such as cantilevers [153]. This method is often used in conjunction with LDV, thus allowing for simultaneous excitation and measurement of the cantilever resonant characteristics. In this thesis a mid-infrared laser (4.55 µm wavelength, Thorlabs Inc., USA) was used to excite the bare silicon cantilevers presented in chapter 3.

2.4.3 Scanning electron microscopy (SEM)

SEM is an optical characterization technique based on the interaction of electrons with the sample surface [154]. Electrons are emitted by a filament, accelerated and focused on the sample using magnetic lenses. Since the optical path is evacuated, the beam can be moved very precisely across the surface. When the beam impinges on the sample surface, electrons are ejected from the atoms (secondary electrons, SE) and some of the incident electrons are scattered back (back scattered electrons, BSE). The intensity of these electrons is measured with a detector and converted into a gray value. By scanning the surface, an image of the surface structure can be obtained. The secondary electrons primarily reflect the topography, while the intensity of the BSE depends on the atomic number of the sample material, therefore providing material contrast. The major advantage of SEM is the high spatial resolution compared to optical light microscopy, due to the high energy of the incident electrons (several keV) resulting in a low characteristic wavelength. Another mode of operation is energy-dispersive X-ray spectroscopy (EDX). The incident electron beam ejects electrons from inner shells of the atoms forming the target material, leaving an electron hole. EDX is based on the measurement of the X-ray radiation, that is generated when this hole is repopulated by an electron from an outer higher-energy shell. Since the wavelength of this X-ray radiation is material-dependent, the chemical composition of the sample material can be determined.

In this thesis, the commercially available scanning electron microscopes SU8030 (Hitachi Ltd., Japan) and JSM-IT500 (JEOL Ltd., Japan) were used for imaging purposes and the characterization of oil deposits using EDX.

2.4.4 Atomic force microscopy (AFM)

Atomic force microscopy (AFM) is a well-established variant of scanning probe microscopy (SPM). Rather than using light or electrons, a microscopic sharp tip attached to the end of a cantilever is used to probe the sample surface [155]. While the tip scans over the surface, the interaction with the sample via atomic forces is used to reconstruct the sample topography. The basic components of an atomic force microscope are a piezo tube to enable the lateral and vertical positioning of the probe tip with extremely high precision and an optical system to measure the deflection of the cantilever. The light of a laser diode is reflected from the backside of the cantilever and captured in a position-sensitive photodetector. A feedback-system allows for the adjustment of the interaction force via controlling the voltage of the vertical actuators of the piezo tube.

Three different imaging modes are commonly used:

1. *Contact mode:* The tip is in mechanical contact with the sample surface and is deflected by the sample's topography. In constant height operation, the output of the position-sensitive photodetector directly reflects the topography of the surface. Because of the risk of damage to both the tip and the specimen in this mode, the alternative constant force mode is used far more frequently. Here the force (*i.e.*, the deflection) of the cantilever is kept constant by the control loop, the topography is therefore derived from the piezo tube actuator signal for the vertical positioning of the tip.

2. *Non-Contact mode:* The tip of the cantilever is not in contact with the sample but oscillates at the mechanical resonance frequency of the cantilever above the surface. Long range forces, such as the *van der Waals* forces, interact with the tip, thus changing the cantilever's resonance frequency. While scanning the surface, the controller adjusts the height of the tip in a way that the resonance frequency stays constant. Again, the topography is derived from the actuator signal of the piezo tube.

3. *Tapping mode:* In this mode, the tip is in intermittent contact with the sample surface while the cantilever oscillates near its resonant frequency. The interaction with the surface reduces the amplitude of vibration, allowing the derivation of the topography. This mode can be described as a combination of contact and non-contact modes and is particularly used in the study of biological samples.

In this thesis, the AFM was not used for imaging purposes but as a micromanipulation tool. The exceptional high spatial accuracy of the piezo tube allows to manipulate microparticles using a tipless cantilever with a precision of several µm. This technique is explained in detail in section 3.2.

2.5 Lubrication engineering

2.5.1 Introduction

Lubricating oil reduces the wear and controls the friction between two moving surfaces by forming a thin reaction layer, often called the tribofilm, and/or a thin film of oil, the so-called hydrodynamic film, effectively preventing the direct physical contact of the surfaces [156]. The friction of an oil-lubricated contact is dependent on the contact load (pressure), the relative velocity of the surfaces and the viscosity of the lubricating oil. This dependency is qualitatively visualized in the Stribeck curve (Figure 2-9), where three lubrication regimes can be identified [157]:

1. *Boundary lubrication:* Direct contact of surfaces, due to high load, low velocity or low viscosity.

2. *Mixed lubrication:* Some asperities of the facing surfaces touch, friction decreases rapidly with increasing viscosity, velocity or decreasing contact load.

3. *Hydrodynamic lubrication:* Surfaces are fully separated by hydrodynamic film, friction coefficient slowly increases with velocity, viscosity and lower loads due to fluidic friction.

The ideal operating point for lubricated contacts is in the hydrodynamic lubrication regime, close to the crossover point to the mixed regime, as this point offers a balanced trade-off between durability of the contact and low friction [158]. However, the machine cannot always be operated at this point, as during start-up, shut-down and in partial load operation the necessary contact speed for the hydrodynamic film to form is not given. Besides the effect on friction, lubricating oils serve many other purposes such as cooling hot parts of the machinery, collecting wear debris and transport it to filter elements or acting as a seal for gases, as found for example in engines where the engine oil helps sealing the gap between the piston ring and cylinder wall. Additionally, the oil film protects the working surfaces from corrosion and prevents components from seizing.

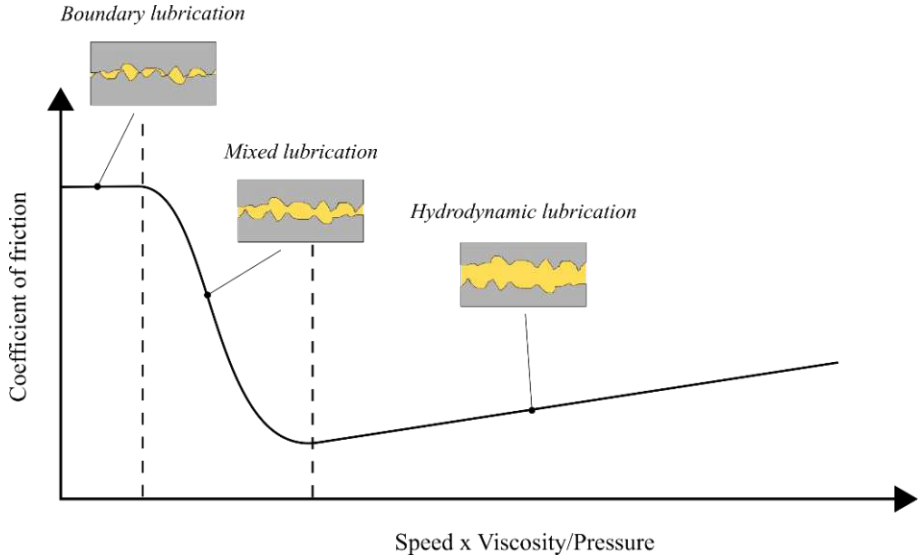

Figure 2-9:Stribeck curve visualizing the dependence of the coefficient of friction on the contact speed, pressure (load) and viscosity of the lubricating oil [157].

Types of lubricating oils

Depending on the chemical composition and the fabrication, three types of lubricating oils can be distinguished [156] [159] [160]:

1. *Mineral oils:* Refined crude oil products, generally speaking a mixture of paraffinic, aromatic and naphthenic hydrocarbons. Currently, the most widely used type of lubricating oil.

2. *Synthetic oils:* Mixture of synthetized hydrocarbons from sources like crude oil and others. Better performance in comparison to refined crude oil lubricants due to their adjustable properties.

3. *Natural oils:* Derived from natural sources such as vegetable oils. Very limited use at present, but on the rise due to efforts to find climate-friendly alternatives to mineral oil.

Oil additives

While the pure lubricating oil, the so-called base oil, provides the basic lubrication to the machinery, oil additives are needed to improve its performance, enhance its functionality and suppress undesirable properties such as the tendency to form deposits [161]. Many different oil additives have been developed that are, based on the application, blended into the base oil. The following list gives an overview of the most encountered additives in modern lubricating oils:

- *Antioxidants:* Oxidation of oil components is one of the main causes of deterioration of lubricating oils, as this process generates harmful substances that change the lubricating properties of the oil and lead to the formation of deposits. Therefore, virtually all lubricating oils contain antioxidant additives that prevent oxidation or inhibit the harmful oxidation by-

products. A detailed explanation of the mechanisms leading to the formation of deposits, the so-called varnish, is given in section 4.3.1.

- *Anti-wear (AW) additives:* These additives prevent metal-to-metal contact by forming a reaction layer on the metal surfaces, where the "normal" oil film does not provide enough lubrication. This layer can serve different purposes, depending on the type of AW additive used. It either supports the hydrodynamic oil film by filling the asperities or acts as a sacrificial layer when asperities come in contact. Some AW additives also react with the surface and have a polishing effect on the surface by removing protruding asperities.

- *Extreme pressure (EP) additives:* Similar to AW additives, the EP additives react with the metal surfaces to form sacrificial layers that prevent direct contact between the metal surfaces. However, the rate of reaction is much faster compared to AW additives and is triggered by very high pressures and temperatures, which is why they serve as protection in high load situations.

- *Viscosity modifiers:* Help to maintain constant viscosity throughout a large temperature range by counteracting the thinning of the oil at elevated temperatures. Viscosity modifiers therefore increase the usable temperature range of the lubricating oil.

- *Detergents and dispersants:* Together with antioxidant additives, detergents and dispersants provide contamination control in the lubricating oil by neutralizing oxidation-derived acids and prevent oxidation products, soot and wear particles from accumulating by keeping them suspended in the oil.

- *Friction modifiers:* These additives decrease the friction of, *e.g.,* engines, by forming a boundary layer with a very low coefficient of friction and are used to increase fuel economy.

- *Metal deactivators:* Prevent the catalytic decomposition of oil constituents by metal surfaces (such as copper) through formation of a passivating layer.

- *Demulsifier:* When oil is contaminated with water, emulsion can form with sufficient agitation, thus greatly reducing the lubrication ability. Demulsifier additives ensure separation of water and oil and thus prevent the formation of oil-water mixtures.

- *Anti-foaming agents:* Reduce formation of foam and air bubbles, as they cause a local loss of lubrication and therefore overstressing of the surface material.

- *Pour point depressants*: Inhibit the formation of paraffinic wax at low temperatures, therefore enhancing the usable temperature range for, *e.g.,* cold-starts of engines.

- *Rust/Corrosion inhibitor:* Protection against oxidation of ferrous parts in the machinery by forming a protective layer.

2.5.2 Formulation of modern turbine oils

Due to their short start-up times and fast power regulation, gas turbines are a key element of today's energy supply, as they are used to feed additional electrical energy in periods of high demand. However, because of economic and ecological reasons, there is an ever-increasing demand for higher turbine efficiency, leading to increased firing temperatures, higher load capacities and longer service intervals of the lubricant in use [3]. In modern turbine systems, the lubricating oil does not only supply lubrication and cooling to the bearings but also performs many other functions such as providing hydrostatic lift during the start-up and serve as hydraulic liquid for the actuation of control valves. The turbine oil must supply sufficient lubrication in different running conditions, from high temperatures and load during peak demand operation, to low temperature and speed operation when the turbine is on turning gear. Oil sumps of modern gas turbine systems may hold oil volumes up to several thousand liters. Hence, unlike engine oils that are changed annually, the targeted lifespan for turbine oils is up to 10 years. To fulfill the performance demands for such a long time span, the turbine oil has to be formulated using high performance base oils and a carefully balanced additive package. Base oils are categorized by the American Petroleum Institute (API) into five categories, depending on the sulfur and saturate content as well as the viscosity index (VI) for group I to III and chemistry for group IV and V, as seen in Table 2-2 [162]. The viscosity index is a measure for the temperature behavior of the oil viscosity. To ensure stable lubrication, the viscosity of the lubricating oil in use should preferably only vary little over a wide temperature range. Historically, the viscosity index ranged from 0 (high temperature dependence) to 100 (low temperature dependence). However, due to improved refinement techniques, modern base oils show viscosity indices of more than 100.

Table 2-2: Classification of base stocks by the American Petroleum Institute (API) [162].

Group	Sulfur (wt. %)		Saturated hydrocarbons (wt. %)	Viscosity index
I	> 0.03	and/or	< 90	80-119
II	< 0.03	and	> 90	80-119
III	< 0.03	and	> 90	> 120
IV	Polyalphaolefins (PAO)			
V	All others not included in group I-IV			

Gas turbine oils were traditionally formulated with solvent-refined group I base oils, where the relatively high sulfur content offered enough oxidation resistance for medium load operation. However, the increased thermal load in modern turbine systems leads to a faster degradation of group I base oils which makes it necessary to use highly refined group II and III base oils. Due to the higher saturate content, these base oils show enhanced chemical and thermal stability as well as an improved viscosity index.

Most turbine oils used today are based on group II and group III base oils. However, due to the high degree of refinement, these base oils lack solvency for contaminants such as oxidation products, leading to an early onset of precipitation and the formation of deposits [48]. The additive formulation is therefore focused on controlling these deposits rather than viscosity or acid number. Typically, the additive package of modern turbine oils constitutes about 0.5-1.5% of the total mass, whereas antioxidants take up the highest proportion. While group I base oils were usually formulated with only one type of antioxidant, the trend is nowadays towards synergistic combinations, such as phenolic and aminic antioxidants. The phenolic antioxidant effectively protects the oil from oxidation at low temperatures but will decompose to regenerate the aminic antioxidant at higher temperatures, which offers excellent protection in the high-temperature regime [161]. However, the exact composition of turbine oils is a well-kept trade secret of the respective manufacturer.

Since the goal of this thesis was the development of a sensor system to detect deterioration of turbine oils, all experiments in the following chapters were conducted using a commercially available oil for steam and gas turbines. This turbine oil has the approvals from established producers of turbomachinery and is therefore widely used in industry.

2.5.3 Oil degradation mechanisms

During use, lubricating oil is exposed to many external influences that negatively impact its properties such as air, heat, humidity, particle contamination and high pressures. As discussed in the previous section, the base oil is blended with additives to increase its resilience and ensure proper lubrication under these conditions. However, most additives are slowly consumed during operation, leading to a depletion of the additive levels and consequently a deterioration of the oil's lubrication performance. Due to inappropriate operating conditions, this process can be accelerated significantly, leading to an early onset of oil degradation. In the following, the most relevant degradation mechanisms of lubricating oils are described [48].

Oxidative degradation

Oxidative degradation of oil constituents is the most prominent degradation mechanism in lubricating oils [47]. Due to the demand of high turbine efficiency and the enhanced burning temperatures, thermal stress on the lubricating oil has increased significantly. The oxidation rate approximately increases two-fold for every 10 K temperature increase, underlining the severe oxidative stress modern turbine oils are subjected to. Also wear metals, especially copper, can serve as a catalyst and speed up the oxidative degradation process. The oxidative degradation of lubricating oil can be separated into three stages. During the *initiation stage*, hydrocarbons react with oxygen or decompose in the presence of catalyst metals, forming free radicals. The free radicals readily react with the remaining hydrocarbons and dissolved oxygen, resulting in the formation of even more free radicals and oxygenated compounds, such as aldehydes, ketones, etc. This stage is called the *propagation stage* since the initial formation of radicals leads to a progressing oxidative breakdown of the oil constituents. This is the point where the

antioxidants come into play by reacting with the free radicals and oxygenated compounds to break the oxidation cycle. If the antioxidants are exhausted or inappropriate antioxidants are used, the reaction can progress into the *termination stage*, where the oxygenated compounds form organic acids or high molecular weight products via polymerization. In this final stage of oxidation, these products will eventually become insoluble and lead to the buildup of deposits, such as sludge and varnish as extensively discussed in section 4.3.1.

Thermal breakdown

In the absence of oxygen, overheating of the oil can cause chemical breakdown of the base oil and additives leading to the generation of insoluble reaction products. The temperature needed to initiate this decomposition process is usually higher than 200°C and can arise from hot spots such as broken bearings, combustion processes, steam and similar. Another source of heat is *micro-dieseling*: entrained air bubbles travel from low-pressure to high-pressure areas, where the increased pressure leads to adiabatic compression (implosion) of the air bubble, resulting in localized temperatures of more than 1000°C. Therefore, special care must be taken to avoid excessive aeration of the oil that can stem from suction line and pump seal leaks or an inappropriate design of the lubrication system.

Spark discharge

Due to internal friction of the flowing oil, a considerable amount of electric charge can build up, ultimately leading to spark discharges. These discharges cause localized overheating and decomposition of the lubricating oil.

2.5.4 Laboratory methods to measure lubricant condition

As discussed in the previous sections, modern lubricating oils are a complex mixture of base oils and additives. During operation, some of the additives are consumed by degradative mechanisms, transformed into other chemical species or precipitate out of solution. Due to the long service-life of lubricating oil in industrial applications, the monitoring of the lubricant condition is of utmost importance, to ensure interruption-free operation without unscheduled downtime. The measurement methods for monitoring the most important oil parameters are presented in this section and their use within the scope of this work is explained.

Viscosity

Viscosity is an important parameter for every lubricating oil, as it defines the thickness of the hydrodynamic film during operation. Wrong oil viscosity with regard to the operating conditions can lead to fatal damage of the lubricated machinery. Oil degradation, as described above, leads to a change of oil viscosity due to the formation of high molecular weight products or the evaporation of short chained hydrocarbons (so-called *short ends*) [50]. The monitoring of the viscosity is therefore of utmost importance for a reliable operation of every lubricated machinery. Because the viscosity strongly

depends on the temperature, the measurement should be done at two different temperatures (commonly used are 40°C and 100°C) to verify the effect of the viscosity modifiers.

Most instruments to measure the viscosity in a laboratory setting are based on the viscous drag force that is caused by the relative movement of the fluid under test and a solid surface. In falling ball viscometers, a metal sphere falls vertically through the fluid and the time to pass a defined distance is measured. The reverse principle is found in capillary viscometer that use gravity to force a defined volume of the fluid through a capillary. Again, the time is measured and correlated with a corresponding viscosity value. The viscosity values stated in this thesis are measured using a Stabinger viscometer (Anton Paar SVM 3000) according to ASTM D7042 [163]. A metal tube is filled with the sample liquid and rotated at a constant speed in a temperature-controlled enclosure. A cylinder is placed in the tube and brought to rotation by the fluid shear forces. Magnets attached to the cylinder induce eddy-currents in the enclosing metal tube that counteract the rotation. The equilibrium rotational speed of the inner cylinder is measured and converted into a viscosity value. The advantage of this measurement technique is a very high precision, the need for only small sample volumes, and the possibility to determine the viscosity and density over a wide temperature range.

Neutralization number

The degradation mechanisms, as discussed in the previous section, lead to the formation of acidic species, such as carboxylic acids. The acidity is therefore used as an indicator of the oil condition and is quantified by the neutralization number, which is the amount of potassium hydroxide needed to neutralize the acid in one gram of oil (mg KOH/g). This value is determined by manual or automatic titration of the oil sample. For modern turbine oils based on highly refined group II or group III base oil, the degradation-induced change of the neutralization number is usually very low and in the range of 0.1 mg KOH/g [50]. The values stated in this thesis were manually determined using a pH value dependent color indicator as described in DIN 51588 [164].

Spectral analysis (FTIR)

The characterization of the oil infrared absorption spectrum gives insights in the chemical composition of the lubricant and is used to monitor degradation-induced changes thereof. The most common technique is FTIR (Fourier Transform Infrared Spectroscopy). The light of a polychromatic infrared source is split up into two arms of a Michelson interferometer, where the length of one arm can be varied by a movable mirror. The changing beam path length causes interference patterns that are dependent on the wavelength and absorption in the sample. The intensity is recorded in dependence of the mirror position (interferogram) and post-processed using a Fourier transform algorithm. The resulting absorbance spectrum is plotted over the wavenumber (inverse of wavelength, given in cm^{-1}) and contains characteristic absorbance bands, since specific molecules absorb light at specific wavelengths. Thus, it is possible to detect the presence of certain chemical species in the lubricating oil, such as oxidation products and additive components. In mineral oil, a distinct change in the absorption spectrum at a

wavenumber of 1710 cm^{-1} can be noticed due to the oxidation of the base oil as described in DIN 51453 [60]. According to this standard, the difference of the absorption value of the used oil and a reference oil (fresh, out of the container) is stated in the unit *Absorption per centimeter oil* (A/cm) and was used to quantify the oxidation-induced degradation of the lubricating oils studied in this thesis.

Gravimetric analysis

This measurement technique allows for the detection of particulate matter in lubricating oil and is based on running the oil through a membrane filter with a sub-micron pore size, as described for example in ASTM 4055 [165]. The particle concentration of the oil is determined by weighing the membrane before and after the filtration process and is given in *mg/kg oil*. The membrane may be washed after the filtering with a series of solvents to remove certain particle species, however, this procedure only allows for a rough distinction of the type and chemical composition of the particles. Another major source of error is the temperature-dependent solubility of certain particle species, like polymerized oxidation products. At high temperatures, the oil can hold more particles in suspension compared to low temperatures. Because the oil temperature during the filtering process usually differs from those during operation, the measured particle concentration may not reflect the actual concentration in the oil circuit of the lubricated machinery.

Oxidation stability (RPVOT, TOST)

The Rotating Pressure Vessel Oxidation Test (RPVOT) and Turbine Oil Oxidation Stability Test (TOST) are procedures to test the resistance of a lubricating oil to oxidative degradation [166] [167]. Both tests are established in industry and the results are used to determine the remaining lifetime of a lubricant in use. For the RPVOT 50 g of the tested lubricant is mixed with 5 ml of distilled water and poured into a glass beaker that contains a copper coil to serve as a catalyst. The glass beaker is placed in a sealable steal container that is filled with pure oxygen at a pressure of exactly 620 kPa. Because of oil oxidation, the oxygen in the steel container is slowly consumed, leading to a drop in gas pressure. While monitoring the gas pressure, the beaker is rotated at 100 revolutions/min until the pressure drops by 175 kPa. The time in minutes to reach this pressure drop is then given as the RPVOT value. For TOST, 300 ml of oil is mixed with 60 ml of water and heated to 95°C while a copper and steel coil serves as a catalyst. Oxygen is injected into the oil-water mixture until a neutralization number of 2 mg KOH/g is reached. Again, the time to reach this value is recorded and given as "TOST life" in hours. Typical results of these tests for modern turbine oils are in the range of thousand minutes for RPVOT and several thousand hours for TOST [168]. However, these methods measure the effectiveness of the remaining antioxidant additives and do not allow for the detection of insoluble species that have already formed in the lubricating oil. Therefore, despite their applicability in industrial lubricant condition monitoring, the RPVOT and TOST were not applied in this thesis.

2.5.5 Accelerated aging of turbine oils

As mentioned above, the lifetime of turbine oils can nowadays reach values up to 10 years. In many situations, such as testing and benchmarking a new sensor system, it is desirable to age oils in a defined manner in a short time to produce samples with different degrees of oil deterioration. As explained above, the oxidation rate of the oil doubles with every 10 K increase in temperature. Therefore, if the oil is exposed to elevated temperatures (> 100°C), the entire life cycle of an oil can be simulated in just a few days. Additionally, catalyst metals such as copper can be added to accelerate the aging process. The injection of pure oxygen can further accelerate oil aging, which is particularly recommended for large quantities of oil.

In this thesis, thermal-oxidative aging analog to the standard DIN 51545:2023-10 is applied, if not stated otherwise [169]. In this technique, 50 ml of lubricating oil are filled in a glass beaker and heated to 150°C for several hours. This procedure leads to a progressive oxidative deterioration of the oil and was used to produce oil samples with different levels of oxidative deterioration, as verified by standard laboratory methods (cf. section 4.3)

3 Mass detection in vacuum with MEMS resonators using non-conventional eigenmodes

Parts of this chapter were published in [170].

After the theoretical framework for mass detection using the 1D-modes of resonant microcantilever was established in the previous chapter, this section covers the generalization of the framework to non-conventional 2D-modes of plate-like microcantilevers. The first question to be answered is how to approximate the mode shape function of 2D-modes for the derivation of the position-dependent mass responsivity. Next, the validity of this expression is investigated by experimentally determining the mass responsivity of the fundamental roof tile-shaped eigenmode of a plate-like cantilever. The results of these experiments and their validation allow a more detailed discussion of the position-dependent mass responsivity. In addition, important consequences regarding the design and accuracy of resonant mass sensors are discussed when utilizing non-conventional eigenmodes of plate-like cantilevers.

3.1 Modelling the mass responsivity of non-conventional eigenmodes

3.1.1 General considerations

In section 2.1.4 an expression for the position-dependent mass responsivity of one-dimensional eigenmodes found in microcantilevers was derived. In this expression, the resonance frequency shift only depends on the position of the additional mass along the length of the cantilever since the mode shape function is only dependent on one coordinate (Figure 3-1a). When examining non-conventional eigenmodes of, *e.g.*, plate-like microcantilevers, the mass responsivity $\mathcal{R}$ depends on two coordinates due to the two-dimensional mode shape of the oscillation [171]:

$$\mathcal{R}(x,y) = -\frac{\Omega_0}{2m_c}\phi^2(x,y)\,. \tag{3.1}$$

with Ω_0 and m_c being the resonance frequency and the cantilever mass, respectively. The now two-dimensional mode shape function $\phi(x,y)$ causes the resonance frequency shift to be dependent on the exact position of the additional mass along the length and width of the microcantilever (Figure 3-1b). Note, that for the validity of equation 3.1 a suitable normalization of the mode shape function must be chosen, as described for the one-dimensional case in section 2.1.2. The extension of this normalization procedure to two-dimensional non-conventional modes will be shown below.

In this section, the general workflow for deriving the mass responsivity of non-conventional eigenmodes is demonstrated using the fundamental roof tile-shaped mode (12-mode) as an example. However, due to its universal applicability, the method presented here can be used for any eigenmode found in oscillating microcantilevers.

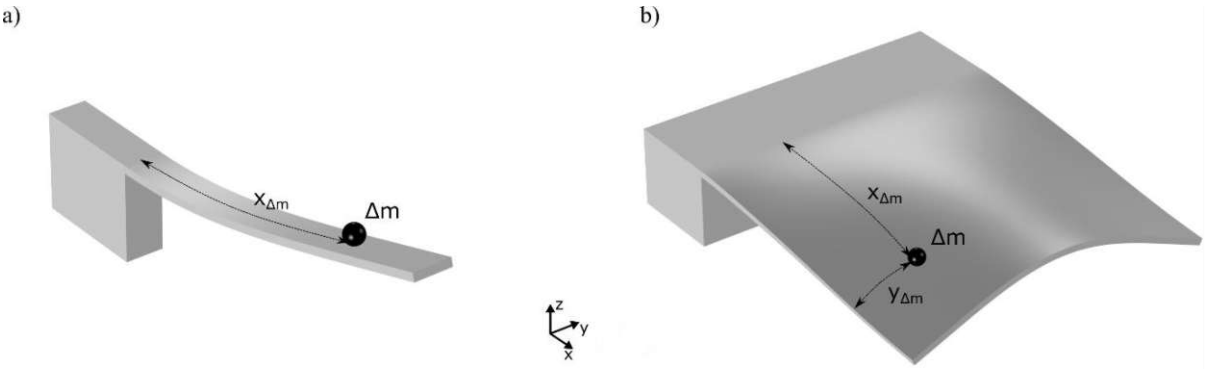

Figure 3-1: The resonance frequency shift induced by an additional mass Δm depends on the location on the cantilever: (a) only along the length of the cantilever for 1D-flexural modes, (b) along the length and width of the cantilever for 2D non-conventional modes.

3.1.2 Derivation of the mode shape function and the position-dependent mass responsivity for the fundamental roof tile-shaped mode

As explained in section 2.1.2, simple analytical approximations of the mode shape yield the resonance frequency with sufficient precision for a clamped plate. In contrast, when using a resonant structure for mass sensing, these approximations are not sufficient, as any deviation from the accurate mode shape will directly affect the derived mass responsivity. In contrast to conventional one-dimensional eigenmodes, there is no analytical expression that yield the exact mode shape function of the roof tile-shaped eigenmode. Hence, another approach was used in this thesis. A convenient method to predict the mode shape function of oscillating structures with high accuracy is the finite element method (FEM). By defining the geometry and material properties of the structure of interest, an eigenfrequency study yields all possible mode shapes and resonance frequencies, respectively. This approach was applied in this work to derive the mode shape function of the fundamental roof tile-shaped eigenmode found in silicon microcantilevers. In the following, the oscillating structure is assumed to be a quadratic plate with a side length of 1000 µm and a thickness of 20 µm, made of monocrystalline silicon. The plate is in the cantilever configuration, *i.e.,* it is fixed on one side and free on the remaining sides.

The geometry was defined in the FEM software (COMSOL Multiphysics[3]) and the default solid mechanics module was used to model the mechanical behavior of the structure. To ensure high accuracy when simulating the mode shape, special care has to be taken to use the correct material model for the structure under study. By default, COMSOL assumes isotropic material behavior, neglecting any

[3] COMSOL Multiphysics® v. 5.5. COMSOL AB, Stockholm, Sweden (http://www.comsol.com).

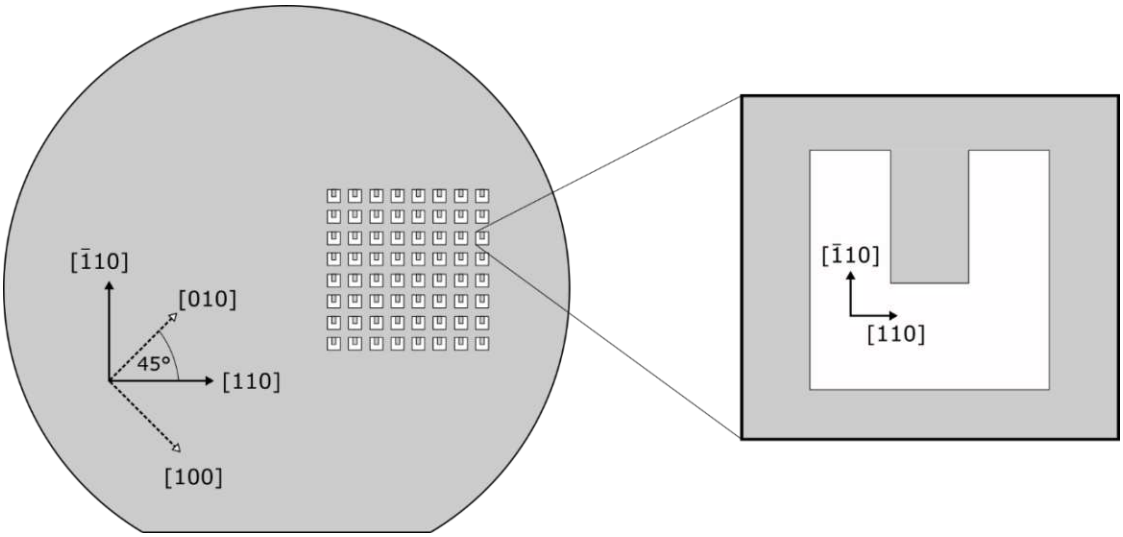

Figure 3-2: Crystal orientation in a standard (100) silicon wafer. The flat is oriented along the [110] directions, hence, the fabricated devices are usually aligned in the same direction. As the elasticity matrix implemented in the FEM-software is usually specified for devices along the [100] directions of the silicon lattice, its values must be adjusted to account for the rotation.

directional dependence of the elastic constants of monocrystalline silicon. While this simplified material model is usually sufficient for conventional flexural out-of-plane modes, the two-dimensional non-conventional eigenmodes of microcantilevers require a full anisotropic material model to replicate the exact mode shape. However, when using an anisotropic material model, the correct alignment of the structure with respect to the simulation coordinate system must be chosen. The fundamental elasticity matrix, as pre-defined in the FEM-software, is specified for devices oriented along the <100> directions of the silicon lattice. However, for the commonly used (100)-wafers in MEMS technology, the primary flat is aligned with the <110> directions (see Figure 3-2). As this flat is used to align the wafer in the MEMS fabrication equipment, the resulting devices are usually also oriented along this group of directions and the fundamental elastic matrix must be adapted. An excellent in-depth discussion of this topic can be found in the study of Hopcroft *et al.* [172] that also provides the elastic constants which are used in this section. After defining the geometry and material model, the FEM-software calculates the eigenmodes and respective resonance frequencies. A comparison of the simulated mode shapes for the isotropic and anisotropic material model is depicted in Figure 3-3, where the strong influence of the selected material model on the resulting mode shape, especially in the region of the nodal lines, is illustrated. When comparing the simulated mode shapes functions to a Laser-Doppler scan of the fundamental roof tile-shaped mode, it is apparent that only the anisotropic material model reproduces the correct mode shape function.

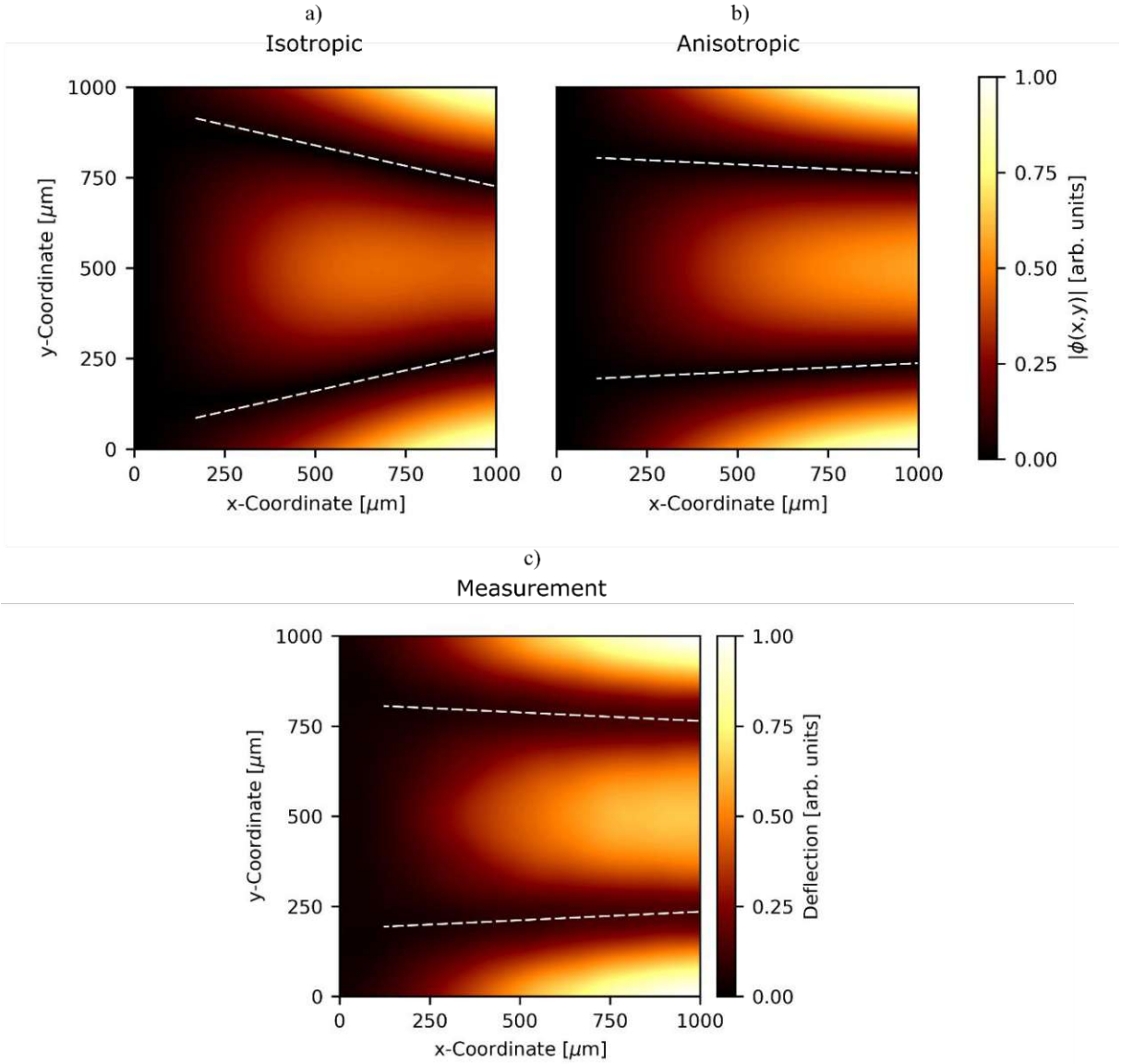

Figure 3-3: Comparison of the FEM-derived mode shape and a Laser-Doppler scan of the fundamental roof tile-shaped eigenmode for a quadratic silicon microcantilever (clamped at x = 0): (a) using an isotropic material model, the nodal lines (white dashed lines) along the length of the cantilever gradually approach each other. (b) The mode shape using an anisotropic material model exhibits nodal lines (white dashed lines) approximately parallel to the edges of the cantilever. A comparison to a Laser-Doppler scan (c) shows that only the anisotropic material model correctly reproduces the mode shape.

Since the simulated mode shape is normalized in an arbitrary manner, a suitable normalization scheme must be employed to calculate the position-dependent mass responsivity as given in equation 3.1. The appropriate normalization can be found by considering a cantilever where the mass is evenly distributed on the top surface. The resulting mass responsivity is then given by

$$\mathcal{R}_H = \frac{1}{LW}\int_0^L \int_0^W \mathcal{R}(x,y)\,dx\,dy = -\frac{1}{2}\frac{\Omega_0}{m_c} \qquad 3.2$$

with L and W being the length and width of the cantilever, respectively [173]. By comparing with equation 3.1 it is obvious that the mode shape function $\phi(x,y)$ must be normalized in a way that

$$\frac{1}{LW}\int_0^L\int_0^W \phi^2(x,y)\,dx\,dy = 1\,. \qquad 3.3$$

Using this normalization scheme, the FEM-derived mode shape function can now be used to calculate the mass responsivity at any point (x, y) on the cantilever surface. A surface plot of $\mathcal{R}(x, y)$, calculated by using equation 3.1, is depicted in Figure 3-4a, where a maximum mass responsivity of 24 Hz/ng at a resonance frequency of approximately 207 kHz is found at the edge regions on the free end of the cantilever. Despite the large geometrical dimensions and the high resulting device mass m_c of approximately 50 µg, this mass responsivity value is in the same range or even higher compared to similar devices found in literature, exhibiting even lower m_c-values [174] [175] [176]. This is due to the high resonance frequency of the roof tile-shaped eigenmodes in comparison to the flexural out-of-plane (OOP) modes of the same geometry. For the device under study, the resonance frequency of the fundamental roof tile-shaped eigenmode exceeds the fundamental flexural OOP-mode by one order of a magnitude, thus resulting in a substantial increase of the mass responsivity (see Figure 3-4b).

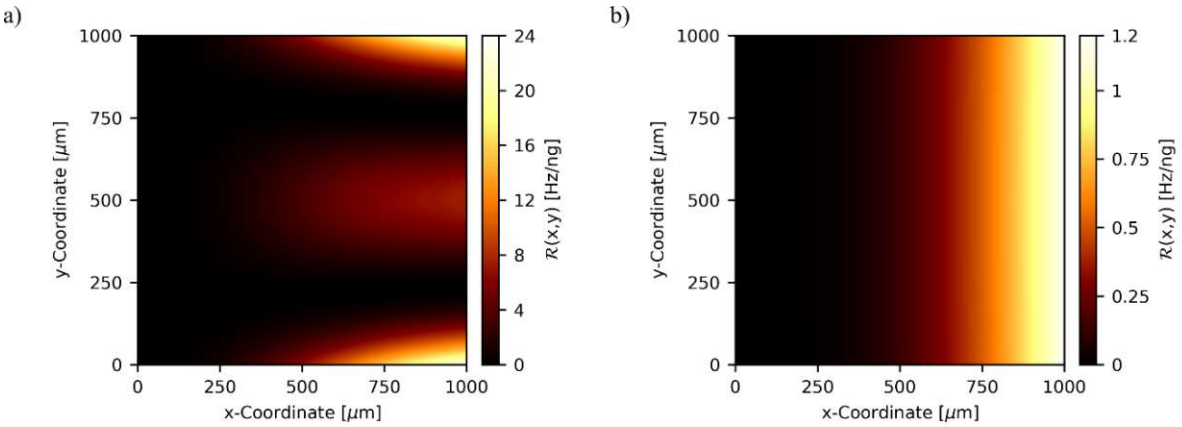

Figure 3-4: Surface plot of the analytically derived mass responsivity $\mathcal{R}$ (equation 3.1) for (a) the fundamental (12) roof tile-shaped and (b) fundamental out-of-plane eigenmode. The cantilever is fixed at x = 0 µm and free on the three remaining sides. Note the different ranges of both color bars.

3.2 Experimental determination of the mass responsivity for the fundamental roof tile-shaped eigenmode

In the last section, the analytical expression to determine the position-dependent mass responsivity of the roof tile-shaped eigenmode was derived using FEM to obtain the mode shape function. In this section, this expression is verified by experimentally mapping the spatial mass responsivity distribution.

This section gives a brief comparison of different probing techniques and the experimental determination of the probing mass. After explaining the fabrication of the devices and the measurement procedure, the experimental results of the spatial mass responsivity mapping are presented. The section concludes with a discussion on the practical implications for mass measurements with resonantly operated microcantilevers.

3.2.1 Probing the mass responsivity of plate-like MEMS cantilevers

3.2.1.1 Probing techniques

The mass responsivity $\mathcal{R}$ of a specific location on the cantilever surface can be determined experimentally by adding a known probing mass Δm to a defined position $(x_{\Delta m}, y_{\Delta m})$ on the cantilever while monitoring the resulting resonance frequency shift $\Delta\Omega_{res}$ [177]:

$$\mathcal{R}(x_{\Delta m}, y_{\Delta m}) = \frac{\Delta\Omega_{res}}{\Delta m}\Big|_{(x_{\Delta m}, y_{\Delta m})} \tag{3.4}$$

If this procedure is repeated for several positions on the cantilever surface, it is possible to experimentally map the spatial distribution of the mass responsivity. However, for this purpose the probing mass must be known with high accuracy, as any error directly affects the determined mass responsivity. A variety of methods can be used to apply mass in a controlled manner to the surface of a cantilever. In the following section the two most important methods are presented and their suitability for testing the mass responsivity of microcantilevers is evaluated.

An established method to deposit mass on microstructures is the Focused Electron Beam Induced Deposition (FEBID) and the Focused Ion Beam Induced Deposition (FIBID). These techniques utilize an electron or ion beam to decompose gaseous precursor molecules in the immediate vicinity of the cantilever surface, resulting in the deposition of non-volatile compounds [178] [179]. The use of high accelerating voltages of up to 300 keV allows a very high spatial resolution with practically no limitations regarding the shape of the deposited material. Using a suitable precursor gas (mainly metal carbonyls or metallocenes), a wide variety of different materials can be deposited. This method was used in [180] to determine the position-dependent mass responsivity of 1-D flexural out-of-plane modes. However, due to incorporation of precursor constituents, the density of the deposited materials can differ from that of the pure material, rendering the precise determination of the probing mass difficult [181]. Additionally, if material is deposited on a large surface area, the material's flexural rigidity can influence the resonance characteristics by changing the overall stiffness of the cantilever. This stiffness effect is also position-dependent and can overcompensate the mass effect when material is deposited in regions of high curvature on the surface, resulting in an increase of the cantilever-related resonance frequency [182]. Hence, two opposing influences affect the cantilever's resonance frequency, which cannot be clearly separated without the exact knowledge of the stiffness of the deposited layer. Another major drawback is that the mass cannot be easily removed, *i.e.,* it cannot be repositioned for a subsequent measurement of the same device. Therefore, multiple mass deposition steps by FEBID/DIBID are needed, reducing the comparability of individual measurements due to the uncertainty in mass determination. The difficulty of determining the deposited mass can be avoided if cantilever material, whose density is usually well known, is removed by FIB milling instead. However, depending on the position of the removed material, the effect of this modification on the cantilever stiffness can in many

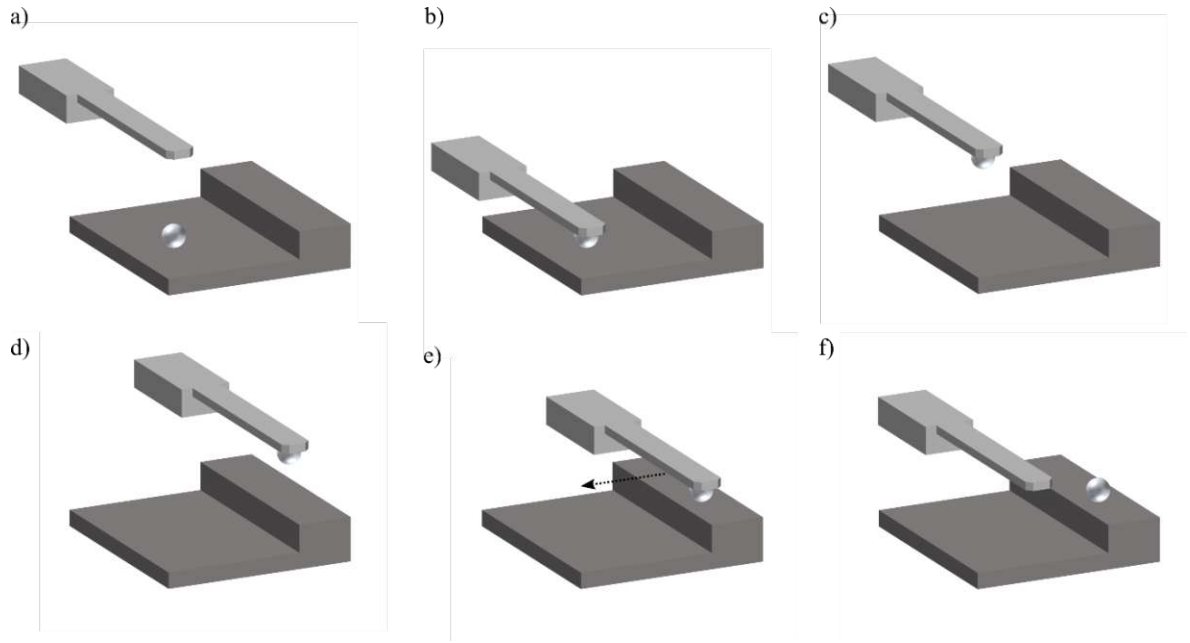

Figure 3-5: Manipulation of a microbead using a tipless AFM cantilever: The AFM cantilever is positioned above a microbead (a), and lowered to the surface (b), upon contact the microbead sticks to the cantilever due to surface adhesion forces and can be lifted up (c), the cantilever is moved to the target location (d), the cantilever with the adhering microbead is brought into contact at the new location (e). By dragging the cantilever parallel to the surface, the microbead is stripped off, the microbead is successfully transferred to a new location (f).

cases be greater than the resulting change in mass, making it difficult to separate the influence of these two effects on the resonant frequency. [180] [183] [184].

The drawbacks mentioned above can be avoided by using microbeads as probing mass. Several works used this technique to deposit mass on a resonator in a controlled manner [87] [185] [186] [187] [188]. The main advantages are the usually well-defined size and density of the microbeads and the possibility to remove and reposition the mass, allowing to use one device and one single microbead for multiple measurements. Additionally, the point-like contact between the bead and the cantilever eliminates all stiffness-related effects on the resonance frequency. Hence, this approach was chosen as probing technique for the position-dependent mass responsivity of the fundamental roof tile-shaped eigenmode. The beads used in this thesis were spherical silica microbeads with a nominal diameter of 10 µm, obtained as a powder from micromod Partikeltechnologie GmbH[4]. These particles can be manipulated and transferred to the cantilever surface with a commercial AFM setup, whereas a tipless microprobe serves as micromanipulation tool (Figure 3-5). The microbead powder is spread across a microscope slide and a suitable microbead is selected. The tipless microprobe is then positioned directly above the bead and brought into contact. Due to surface adhesion forces, the microbead sticks to the probe and can be transferred to another location, where the probe is again brought into contact with the surface. By moving the probe parallel to the surface, the microbead is stripped off and placed on the new position.

[4] micromod Partikeltechnologie GmbH, Rostock, Germany, https://www.micromod.de

By repeating this procedure several times, the attainable positioning precision of this manipulation technique was determined to approximately 2.5 µm.

3.2.1.2 Determination of the probing mass

As mentioned above, the precise knowledge of the probing mass, *i.e.,* the microbead, is of utmost importance when experimentally probing the mass responsivity of a resonant microcantilever. First, the beads were inspected using a scanning electron microscope to determine the diameter (Figure 3-6a) However, the beads showed shape irregularities and exhibited a porous structure, raising concerns regarding the validity of the density provided by the manufacturer. The calculation of the bead mass based on the measured diameter was therefore deemed to be too inaccurate. Hence, the bead mass was determined with the established approach of measuring the resonance frequency shift of the fundamental out-of-plane mode of microcantilevers induced by the addition of the microbead [185]. To ensure maximum accuracy, a set of six different microcantilevers, ranging from 300 to 500 µm in length and 50 to 75 µm in width, was prepared and the bead was successively transferred from one cantilever to another using the procedure as described above and accurately measuring the position of the cantilever (Figure 3-6b). The resonance frequency of each microcantilever was determined under vacuum conditions using a Laser-Doppler vibrometer before and after adding the bead to the surface, while simultaneously monitoring the resonance frequency of the remaining cantilevers to account for variations in vacuum quality. Figure 3-7 shows an example of such a measurement for a cantilever with a length, width and thickness of 300 µm, 50 µm and 20 µm. The resonance frequency shift induced by addition of the microbead is then used to calculate the microbead mass using equation 2.45 in section 2.1.4. Using the individual measurements of all six cantilevers, the mean bead mass and standard deviation was determined to $\mathbf{m_{bead} = 1.245 \pm 0.045\ ng}$. Using the nominal bead density of 1.8 g/cm^3 as

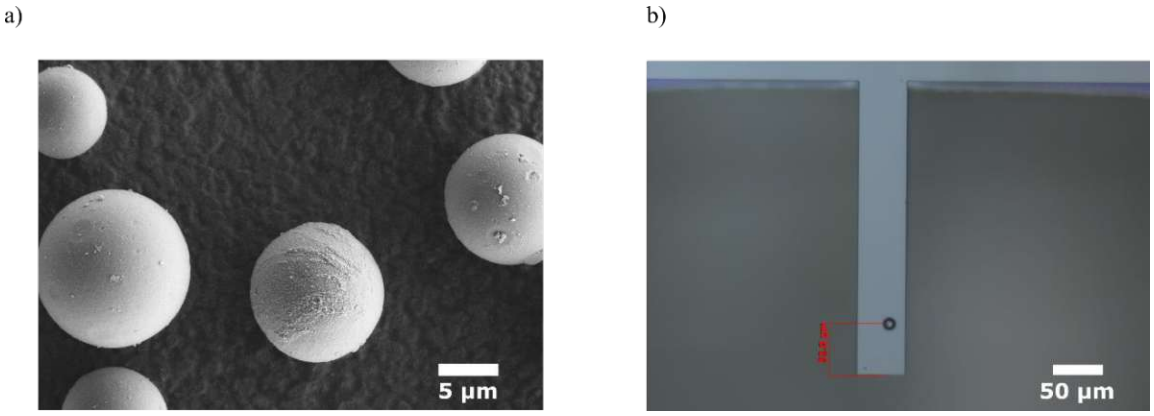

Figure 3-6: (a) SEM micrograph of the silica microbeads with a nominal diameter of 10 µm, (b) The bead is transferred to a cantilever and the bead position is accurately determined. The resulting resonance frequency shift is used to determine the bead mass.

given in the datasheet, this value corresponds to a particle with a diameter of approx. 11 µm, which is well within the size distribution of 10 µm ± 2.5 µm as specified by the manufacturer.

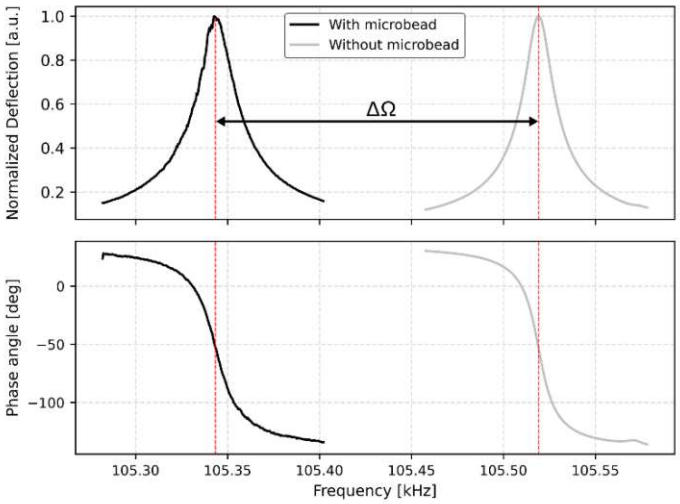

Figure 3-7: Process to determine the microbead mass using the measured amplitude and phase spectra of a microcantilever: The addition of the microbead to the cantilever surface causes a significant resonance frequency shift Δf, which is used to calculate the microbead mass.

3.2.2 Experimental details

3.2.2.1 Fabrication and characterization of the measurement devices

The devices to experimentally determine the mass responsivity of the fundamental roof tile-shaped mode were fabricated from a 4 inch silicon-on-insulator wafer. The (100)-orientated device layer had a thickness of 20 µm, defining the thickness of the cantilever. The dimensions of the microcantilevers were chosen to fit the dimensions used for the FEM-assisted derivation of the mode shape function (quadratic, side length: 1000 µm). The device geometry was defined by structuring the device layer with a deep reactive ion etching (DRIE) process. As described in section 3.1.2, the devices were aligned along the [110]-directions. The cantilevers were released by etching the handle layer with DRIE and subsequent removal of the buried oxide using hydrofluoric acid. Each die consists of two identical microcantilevers that are fixed to the same frame (Figure 3-8a). This design allows for a differential measurement scheme to cancel out any environmental impacts on the cantilever resonance frequency, such as temperature variations, as explained below.

After fabrication, the devices were characterized in a vacuum chamber to eliminate any damping due to the surrounding air. A diode laser (Thorlabs LPS-635-FC[5]) was focused on the free end of the cantilever and the power of the laser source was modulated with a chirp signal with a bandwidth of 125 Hz around the fundamental roof tile-shaped eigenmode's resonance frequency of approx. 205 kHz. The local expansion of the cantilever material due to the laser induced pulsed heating leads to the excitation of the cantilever oscillation in the targeted eigenmode, which is verified by using a laser Doppler vibrometer

[5] Thorlabs Inc., Newton, New Jersey, United States, https://www.thorlabs.com

(Polytec MSA-500[6]) to scan the cantilever surface with a spatial resolution of approximately 13 µm. Figure 3-8b shows the normalized measured displacement of the fundamental roof tile-shaped mode across the cantilever surface while the highlighted points in the figure show the position where the mass responsivity was experimentally determined, as described in the following section. The resonance frequency of the device is within 5% of the simulated resonance frequency showing good agreement with the results of the FEM-study in section 3.1.2.

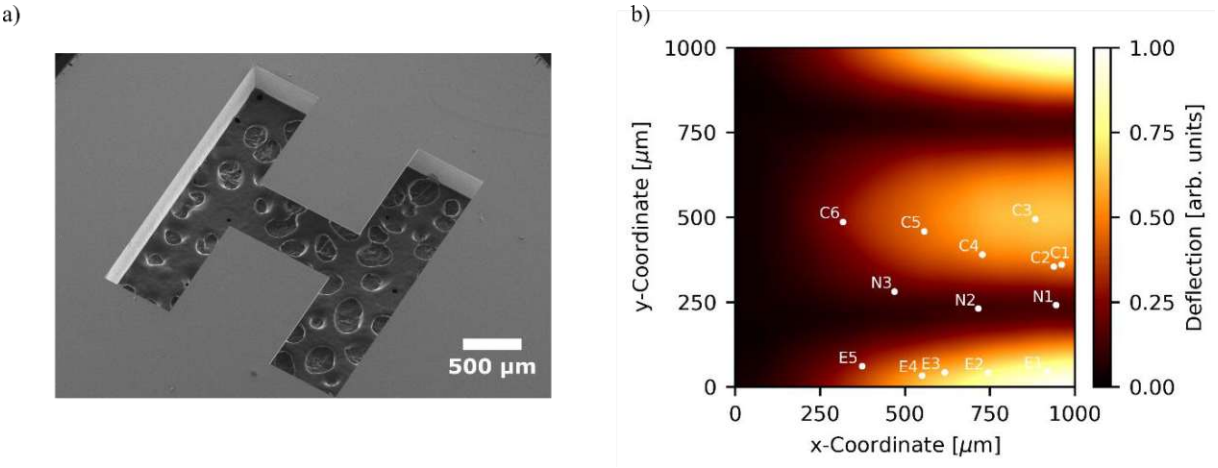

Figure 3-8: (a) SEM micrograph of the device used to map the mass responsivity: Two identical microcantilevers are fixed to the same substrate. (b) Laser Doppler scan of the fundamental roof tile shaped mode. To plot the data a Gaussian filter and a cubic interpolation scheme were applied. The highlighted points show the positions along the edge (E), on the nodal lines (N) and in the centre (C) where the mass responsivity $\mathcal{R}_{Meas}$ was experimentally determined.

3.2.2.2 Measurement procedure

The mass responsivity of a certain point on the cantilever surface was determined in multiple steps: In a first step, the amplitude and phase spectra of both cantilevers on one die (here called *active* and *reference* cantilever) were recorded with LDV using the thermoelastic excitation as described in section 2.4.2. Note that in this first step, no mass was attached to any of the cantilevers. The phase response function from section 2.1.1

$$\varphi(\Omega) = \varphi_0 + \arctan\left(\frac{2\zeta\left(\frac{\Omega}{\Omega_0}\right)}{\left(\frac{\Omega}{\Omega_0}\right)^2 - 1}\right) \qquad 3.5$$

with the phase offset φ_0 and the damping ratio ζ was fitted to the data to determine the resonance frequency Ω_0, which is labelled as $\Omega_{Act,0}$ for the active cantilever with zero added mass and $\Omega_{Ref,0}$ for the reference cantilever. The standard deviation of 10 subsequent measurements was determined as 0.17 Hz.

In the second step, the previously characterized silica bead as described above was transferred to a predefined position on the *active* cantilever surface using the aforementioned AFM micromanipulation

[6] Polytec GmbH, Waldbronn, Germany, https://www.polytec.com/de

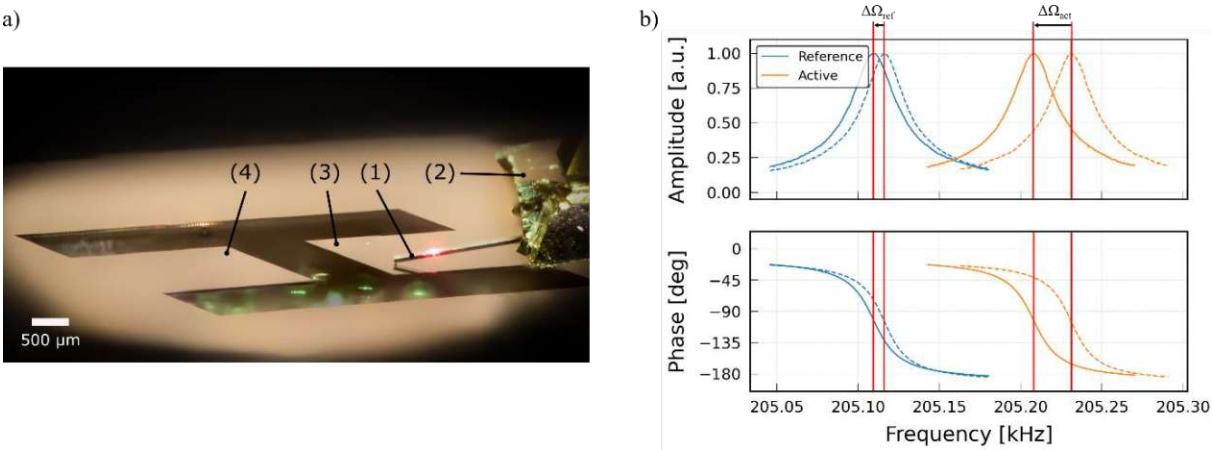

Figure 3-9: (a) Confocal micrograph of the microcantilever used for the experiments. An AFM cantilever (1), fixed to the AFM probe body (2) is used to transfer a silica microbead to a 1000x1000x20 µm³ silicon cantilever (3). An identical cantilever (4) is used as a reference during measurements to cancel out any parasitic temperature effects. (b) Amplitude and phase spectra of the active and reference cantilever before (dashed line) and after (solid line) placing the probing mass.

technique. Figure 3-9a shows a confocal micrograph of the cantilever during the bead transfer process. Note that also in this step, there is no mass attached to the reference cantilever. After bead placement, the measurement procedure as explained above was repeated, which resulted in the resonance frequencies $\Omega_{Act,1}$ and $\Omega_{Ref,1}$ for the mass-loaded active cantilever and reference cantilever, respectively. Figure 3-9b shows the amplitude and phase spectra of both the active and reference cantilever, before and after adding the microbead to the active cantilever. As expected, the resonance frequency of the active cantilever shifts to a lower value due to the added bead mass. However, also the resonance frequency of the reference cantilever shifts in the same direction, which is attributed to changes of the environmental conditions, such as the temperature during the measurement. The observed resonance frequency shift of the active cantilever is therefore not solely caused by the addition of the microbead, but also due to environmental impacts. The influence of the mass would be overestimated if the measurement was not corrected for this additional shift, demonstrating the importance of a differential measurement approach including a reference cantilever. To obtain the resonance frequency shift $\Delta\Omega_{res}$ solely caused by the probing mass, the resonance frequency shift of the reference cantilever $\Delta\Omega_{ref}$ is subtracted from the resonance frequency shift of the active cantilever $\Delta\Omega_{act}$

$$\Delta\Omega_{res} = \underbrace{\left(\Omega_{act,1} - \Omega_{act,0}\right)}_{\Delta\Omega_{act}} - \underbrace{\left(\Omega_{ref,1} - \Omega_{ref,0}\right)}_{\Delta\Omega_{ref}} \tag{3.6}$$

In the last step, the mass responsivity for a certain location (x_i, y_i) is calculated by

$$\mathcal{R}_{meas}(x_i, y_i) = -\frac{\Delta\Omega_{res}}{m_{bead}}\bigg|_{(x_i,y_i)}. \tag{3.7}$$

3.2.3 Results and Discussion

3.2.3.1 Mapping of the spatial mass responsivity distribution

The measurement procedure described above was repeated for fourteen different positions on the cantilever surface highlighted in Figure 3-8b. When choosing the locations to probe the mass responsivity, three key areas on the cantilever surface were identified. Six probing locations were in the center of the cantilever (C1-C6) as well as five points along the free edge (E1-E5). Additionally, three measurements were performed along the nodal line of the roof tile-shaped eigenmode to evaluate the effect of mass at these positions, which are usually not used for mass sensing. Due to the symmetry of the mode shape, it is sufficient to probe only one half of the cantilever.

The measured mass responsivity values $\mathcal{R}_{meas}$ are given in the first row of Table 3-1. The standard deviation of these values is given based on the limited accuracy of 0.17 Hz and 0.045 ng when determining the resonance frequency and probe mass, respectively. As already discussed in section 2.1.4, the mass responsivity at a certain position on the cantilever surface is closely connected to the corresponding vibrational amplitude. This trend was also observed for the experimentally determined mass responsivity $\mathcal{R}_{meas}$. The highest values are found in the edge regions of the free end of the cantilever, where the highest amount of kinetic energy is transferred to the bead and therefore the highest change in resonance frequency occurs. On the other hand, the mass responsivity close to the nodal points is negligible, as the amplitude is close to zero in these areas.

To prove the validity of the analytical expressions derived in section 3.1, equation 3.1 was used to calculate the mass responsivity $\mathcal{R}_{Analytic}$ for the previously defined positions and the values are compared to the experimentally probed mass responsivity. The corresponding results are found in the second row of Table 3-1. Additionally, the influence of the additional mass on the eigenfrequency was simulated using a FEM-model with an added mass on the predefined positions. The simulated resonance frequency shift was used to calculate the position-dependent mass responsivity of the FEM model $\mathcal{R}_{FEM}$, which is given in the third row of Table 3-1.

For both the analytically derived mass responsivity and the FEM model, good agreement with the measured values is found, whereas the largest relative deviations are found in areas of low mass responsivity. For the positions N1 and N2 the values differ by more than a factor of 5, which can be explained by limitations of the experimental setup. Since the resonance frequency shift is well below 1 Hz for these positions, the limited precision of about 0.17 Hz when experimentally determining the resonance frequency introduces a significant error to the measurements, thus dominating the overall precision. From the data in Table 3-1 it can be seen that the values for the analytic model and FEM-model fit almost perfectly. However, it is evident that the measured values differ noticeably for some positions. This error is mainly introduced by the inaccuracy when determining the bead position, as discussed in the following section.

Table 3-1: Values of the experimentally determined mass responsivity $\mathcal{R}_{Meas}$, the analytically derives mass responsivity $\mathcal{R}_{Analytic}$ and the FEM-model $\mathcal{R}_{FEM}$ for fourteen positions along the center (C), nodal lines (N) and edge (E) of the microcantilever. The last row shows the calculated maximal error $\Delta\mathcal{R}_{max}$ for an assumed spatial deviation of 2.5 µm when determining the position of the additional mass.

	Center						Nodal lines			Edge				
Positions	C1	C2	C3	C4	C5	C6	N1	N2	N3	E1	E2	E3	E4	E5
$\mathcal{R}_{Meas}$	3.90 (±0.20)	3.53 (±0.19)	6.78 (±0.28)	4.15 (±0.20)	3.84 (±0.19)	1.17 (±0.14)	0.11 (±0.14)	0.10 (±0.14)	0.60 (±0.14)	13.37 (±0.50)	10.31 (±0.40)	7.50 (±0.30)	6.10 (±0.26)	1.80 (±0.15)
$\mathcal{R}_{Analytic}$	3.50	3.21	6.72	3.93	3.87	1.18	0.02	0.02	0.48	13.37	10.12	6.69	5.73	1.48
$\mathcal{R}_{FEA}$	3.50	3.24	6.76	3.96	3.90	1.17	0.04	0.04	0.49	13.49	10.10	6.76	5.79	1.50
$\Delta\mathcal{R}_{max}$	0.11 (3.1%)	0.1 (3.1%)	0.02 (0.3%)	0.08 (2%)	0.04 (1%)	0.02 (1.7%)	0.02 (100%)	0.01 (50%)	0.03 (6.3%)	0.38 (2.8%)	0.29 (2.9%)	0.21 (3.1%)	0.18 (3.1%)	0.06 (4.1%)

(all values in Hz/ng)

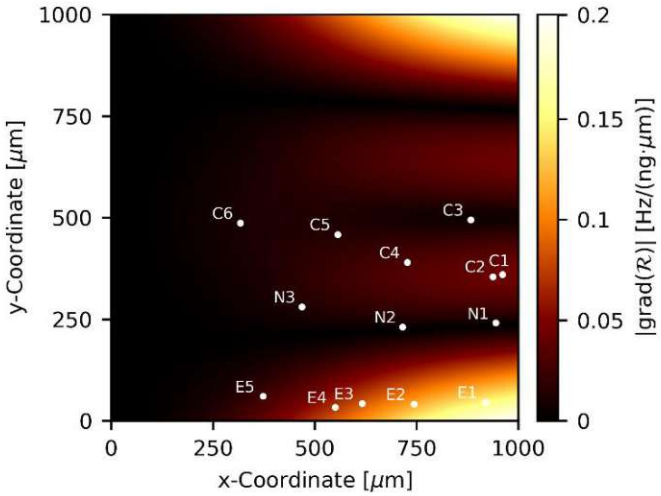

Figure 3-10: Spatial gradient of the analytically derived mass responsivity. The free end is located at x = 0 µm and the cantilever is fixed at x = 1000 µm. The values at the highlighted positions are used to calculate the maximal error of $\mathcal{R}_{Analytic}$ for a deviation of the measured lateral bead position of 2.5 µm.

3.2.3.2 Accuracy considerations

To determine the added mass with high accuracy, its position on the cantilever surface must be known precisely. To study the impact of limited spatial accuracy, the gradient of the analytically derived mass responsivity (Equation 3.1) was calculated and is depicted in Figure 3-10. Assuming a maximum spatial error of 2.5 µm measuring the location of the bead, the resulting maximum error $\Delta\mathcal{R}_{max}$ for all fourteen measurements can be deduced. The results are given in the last row of Table 3-1. The relative error is well below 5% for most positions, whereas it is significantly larger close to the nodal lines. Despite the low spatial gradient in these areas, the error has the same magnitude as the absolute mass responsivity, thus making these areas less attractive for mass sensing purposes. Even though the edge of the microcantilever exhibits the largest mass responsivity (position E1-E5), the high gradient leads to a significant error even for small deviations of the assumed mass position. The lowest error is found for position C3 being in the center of the cantilever. Since the gradient of the mass responsivity is close to zero in this area, the error introduced by the uncertainty of the exact mass position only accounts for an error of less than 0.3%. Hence, the error when determining the mass in these regions is mainly influenced by the achievable accuracy of measuring the resonance frequency.

The results of this section serve as valuable input for the design of resonant mass sensors based on non-conventional eigenmodes and is discussed in the next section.

3.2.3.3 Implications for the design of resonant mass sensors

Knowing the spatial distribution of the mass responsivity $\mathcal{R}(x, y)$ and the measured resonance frequency shift $\Delta\Omega$, an additional mass Δm located on the surface of the microcantilever can be determined using equation 3.1. Experimentally, however, the determination of the resonance frequency shift is always subjected to some uncertainty. In the case the mass is located in an area of small vibrational amplitude, and thus small mass responsivity, the resonance frequency shift may be of the order of this uncertainty,

making it impossible to accurately determine the additional mass precisely. Therefore, when designing a resonant mass sensor based on a microcantilever, special care must be taken to ensure that the mass deposition takes place in the high amplitude regions, thus maximizing the resonance frequency shift. For the fundamental roof tile-shaped eigenmode the most suitable areas for mass measurements are on the free end, well separated from the nodal lines. Hence, functional layers promoting the deposition of mass should therefore be located in these areas.

However, since the position of the mass can usually not be determined exactly, the gradient of mass responsivity must also be considered. The advantage of a high mass responsivity can be offset if the region chosen for mass sensing exhibits a high gradient of the mass responsivity. In these areas, even small errors in the determination of the mass position can lead to large deviations of the calculated mass value. For the fundamental roof tile-shaped eigenmode, the best position is therefore found in the center of the free end (position C3): With a mass responsivity of 6.78 Hz/ng, the error due to a position deviation of 2.5 µm is less than 0.3%, due to a gradient of the mass responsivity close to zero. Provided that the resonance frequency shift is significantly larger than the uncertainty when determining the resonance frequency, the added mass can be determined in this area with the highest precision. Therefore, when designing a resonant mass sensor based on a microcantilever, the spatial distribution of the mass responsivity, the expected magnitude of the mass, and the experimental capabilities for determining the resonant frequency shift should be considered.

3.3 Summary

In this chapter resonant mass detection with non-conventional eigenmodes was investigated, thus generalizing the theory for the commonly used flexural out-of-plane eigenmodes. As an example, the fundamental roof tile-shaped eigenmode was used. Since the mode shape function of this eigenmode cannot be determined analytically, a method was presented that allows the extraction of the mode shape function from a finite element model. It was found that special care must be taken when choosing the material model, because the shape of the simulated mode can deviate significantly from the shape of the real mode if the model does not correctly reflect the properties of the investigated material. Furthermore, the mass responsivity was experimentally determined at certain locations on the cantilever surface using a silica microbead as probing mass and the validity of the FEM-assisted derivation of the mode shape function was shown. Finally, the spatial distribution of mass responsivity and the resulting implications for mass measurements were discussed.

The results in this chapter lay the theoretical foundation for the application of roof tile-shaped eigenmodes in mass sensors, especially in liquid environments. In the next chapter two such sensors for lubricant condition monitoring are presented, whereby the findings of this chapter are used for the design of the sensors and the evaluation of the measured data.

4 MEMS resonators for the detection of particles in liquid environments

4.1 Characterization of roof tile-shaped modes in liquids

4.1.1 General considerations

The flow of viscous fluids is described by a set of partial differential equations, the so-called Navier-Stokes equations [189]. While the existence of a general solution has yet to be proven, these equations are used in everyday live. Discretized forms of the Navier-Stokes equations are the theoretical basis to model wind currents in meteorology, water flow in hydraulic turbines and to design cars and aircrafts, just to highlight some important applications. If the density ρ of the fluid is assumed to be independent of the pressure (incompressible flow), the Navier-Stokes equation states

$$\rho\left(\frac{\partial u}{\partial t} + (u \cdot \nabla)u\right) = -\nabla p + \mu\Delta u + F' . \tag{4.1}$$

Here, u denotes the fluid velocity vector, p is the pressure and μ is the dynamic viscosity of the fluid. The term F' summarizes all external body forces on the fluid, such as gravity, Coriolis force and similar.

The fluid flow field around an oscillating submerged body is highly dependent on the shape of the body, its surroundings and the vibrational mode. However, a typical example to study the flow created by an oscillating body is Stokes second problem. An infinite plane surface is located at x = 0, while the region x > 0 is filled with an incompressible, viscous fluid (Figure 4-1). We are looking for the resulting fluid flow when the plane carries out an oscillatory motion along the y-axis, described by the time-dependent function

$$\mathrm{v} = \mathrm{v}_y = \mathrm{Re}[\mathrm{v}_0 \exp(i\omega t)] = \mathrm{v}_0 \cos(\omega t) . \tag{4.2}$$

Here, ω denotes the angular frequency, $i = \sqrt{-1}$ and v_0 the amplitude of the oscillation. We assume a non-slip boundary condition at the plane surface, hence the fluid velocity u must satisfy

$$u_x = u_z = 0, \quad u_y = \mathrm{v}_y \text{ at } x = 0. \tag{4.3}$$

Due to the symmetry of the problem, the fluid velocity field is directed in the y-direction and only depends on the distance x from the plane surface and the time t. Hence, the convective term $((u \cdot \nabla)u)$ is equal to zero because the fluid flow is independent of the y-coordinate and the velocity in x and z-direction is zero. Also, the pressure is assumed to be constant, therefore $\nabla p = 0$. If all other body forces

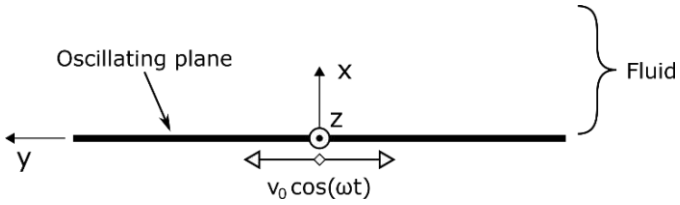

Figure 4-1: Stokes second problem: an infinite long plane oscillates along the y-axis, while the space x >0 is filled with fluid. The Navier-Stokes equations are used to deduce the fluid flow induced by the oscillating plane.

F' are omitted, the Navier-Stokes equation reduces to a one-dimensional heat equation for the fluid velocity in y-direction

$$\frac{\partial u_y}{\partial t} = \nu \frac{\partial^2 u_y}{\partial x^2} \tag{4.4}$$

using the kinematic viscosity of the fluid $\nu = \mu/\rho$. The solution of this equation is of the form

$$u_y = \mathrm{v}_0 \exp[i(\omega t - kx)]\,. \tag{4.5}$$

Inserting equation 4.5 in equation 4.4 results in $i\omega = \nu k^2$, therefore

$$k = \sqrt{i\frac{\omega}{\nu}} = \pm(i+1)\sqrt{\frac{\omega}{2\nu}} \tag{4.6}$$

with $\sqrt{i} = \pm(i+1)/\sqrt{2}$. Using the positive results of all possible solutions in the expression for the fluid velocity in y-direction results in:

$$u_y = \mathrm{v}_0 \exp\left(-\sqrt{\frac{\omega}{2\nu}}x\right)\exp\left[i\left(\omega t - \sqrt{\frac{\omega}{2\nu}}x\right)\right] \tag{4.7}$$

The solution describes a transverse wave that propagates in x-direction with an exponentially decreasing amplitude with respect to the distance from the plane surface. The penetration depth is defined as the distance over which the amplitude has fallen off by a factor $e^{-1} \approx 0.368$ and is given by

$$\delta = \sqrt{\frac{2\nu}{\omega}}\,. \tag{4.8}$$

Analog to the simple example stated above, a submerged oscillating body induces a flow in the liquid layers around it that shows an exponential decay with the rate δ^{-1}. The penetration depth can therefore be viewed as the distance in which the oscillating body interacts with the surrounding liquid [190].

For oscillating bodies of arbitrary shapes, the convective term cannot be neglected in general, unless some simplifications are made based on assumptions regarding the nature of the flow and oscillation. The oscillatory Reynolds number

$$Re = \frac{\omega \rho L^2}{4\mu}, \tag{4.9}$$

where L denotes the characteristic dimension of the oscillating structure, gives the ratio of inertial forces to viscous forces acting in the fluid [94]. For low values of Re, the inertial, *i.e.*, convective, term is negligible. The same reasoning applies when the amplitude of vibration is much smaller than any dimension of the oscillating body. Since this assumption is satisfied for many practical applications of submerged microcantilevers, the solution of Stokes second problem can be considered as a first-order approximation of the resulting fluid flow around the oscillating structure.

So far, only the nature of the induced fluid flow was discussed. However, the fluid interacts with the vibrating structure through a force that is dependent on the fluid velocity u at the surface:

$$F = (\beta_1 + i\beta_2)u = \beta_1 u + \frac{\beta_2}{\omega}\frac{\partial u}{\partial t} \tag{4.10}$$

with a complex constant $\beta = (\beta_1 + i\beta_2)$ [190]. The first term on the right side of 4.10 is proportional to the velocity and therefore represents the dissipative drag force. The second term is proportional to the acceleration and can therefore be interpreted as the inertial force of the displaced fluid around the moving structure. For flexural modes of microcantilevers, equation 4.10 is usually normalized to the cantilever length, resulting in the two coefficients

$$\begin{aligned} g_1 &= \frac{\beta_1}{L} \\ g_2 &= \frac{\beta_2}{\omega L} \end{aligned} \tag{4.11}$$

of which g_1 and g_2 are interpreted as the distributed damping coefficient and distributed effective fluid mass, respectively. These coefficients can be used to calculate the resonance frequency and quality factor of a microcantilever that is immersed in a viscous fluid [191]:

$$f_{liq} = f_0 \frac{1}{\sqrt{\left(1 + \frac{Lg_2}{m_c}\right)}} \sqrt{\left(1 - \frac{1}{2Q^2}\right)} \tag{4.12}$$

$$Q_{visc} = \frac{2\pi \sqrt{1 + \frac{Lg_2}{m_c}}}{\frac{Lg_1}{m_c}} f_0 \tag{4.13}$$

where f_0 denotes the vacuum resonance frequency, m_c is the cantilever mass and Q is the (total) quality factor. Equation 4.12 implies that the main impact on the cantilever's resonance frequency is due to the added fluid mass Lg_2. The last term, representing the influence of the viscous losses on the resonance frequency, can often be neglected given that $Q \gg 1/\sqrt{2}$. The quality factor due to viscous losses Q_{visc} in

equation 4.13 depends inversely on the viscous losses Lg_1, but increases with the fluid mass Lg_2. This is because the displaced fluid mass contributes to the total energy of the vibrating system. There are several studies on the derivation of the coefficients g_1 and g_2. Most of them focus on the flexural out-of-plane modes of cantilevers with a high aspect ratio (*i.e.,* length $L \gg$ width W). For this thesis, the theoretical calculation of the distributed damping and added mass coefficient is not of relevance, however, the added fluid mass will be derived from experimental data by rearranging equation 4.12 for $Lg_2 = m_{liq}$:

$$m_{liq} = m_c \left[\left(\frac{f_0}{f_{liq}} \right)^2 - 1 \right]. \tag{4.14}$$

4.1.2 Interaction with suspended particles

Microcantilevers are very sensitive to changes of the ambient conditions. For suspended microcantilevers the properties of the surrounding fluid have the greatest influence on their vibrational characteristics. Consequently, the parameters g_1 and g_2 (equation 4.11) depend significantly on the viscosity and density of the fluid. Since the sensors developed in this thesis are intended to operate in particle-contaminated liquids, it is necessary to investigate the influence of the particles on the vibrational properties of the microcantilevers used. In the following section, the most important theoretical aspects are explained and the influence of dispersed particles on the vibrational characteristics is investigated experimentally.

Dispersed particles change the physical properties of a liquid, most notably its viscosity and density. While the effect on the density is obvious (liquid is replaced by particles), the impact on the viscosity heavily depends on the particle size, shape and concentration. The particles act as an obstacle in the fluid flow resulting in an increase of viscosity of the liquid-particle system. In this configuration, the introduction of an effective density and an effective viscosity to describe the properties of the liquid-particle dispersion is reasonable to justify. If the fluid moves in relation to the particle with the velocity u, the so-called drag force

$$F_{Drag} = 3\pi\mu_{Liq} D u \tag{4.15}$$

acts on the particle. In this equation μ_{Liq} and D denote the dynamic viscosity of the fluid and the diameter of the particle, respectively. This additional force required to move the fluid manifests macroscopically as increased viscosity of the fluid-particle suspension. An approximate formula for the influence of the particle volume fraction φ in the range $\varphi < 0.15...0.2$ on the viscosity of the suspension μ_{susp} is given by

$$\mu_{susp} = \mu_{liq}(1 + 2.5\varphi + c_2\varphi^2) \tag{4.16}$$

The quadratic term accounts for the particle-particle interaction of the particles with each other, whereby the value of the constant c_2 depends, among other factors, on the type of fluid flow and the properties of the particles [192]. For example, it shows that the effective viscosity for a given particle concentration is higher for small particles than for particles with larger diameter. On the other hand, equation 4.16 shows that the influence of the particles for the particle concentrations occurring in practice (mostly in the ppm range) is negligible compared to other parameters such as temperature.

To study the influence of dispersed particles experimentally, several suspensions were prepared by dispersing hydrophobic trimethylsilyl (TMS)-coated spherical silica microbeads[7] with diameters of 50 nm, 200 nm and 1 µm in base oil using a vortex mixer and subsequent sonication. A relatively high concentration of 10 wt% was chosen for all particle sizes to induce a notable change of viscosity (cf. equation 4.16). In addition, a portion of the 1 µm suspension was diluted to 5 wt% to test the influence of lower concentrations. The device used for this study was a microcantilever with a size of 2524x1274x20 µm^3, which was connected to an impedance analyzer to measure the frequency-dependent electrical response characteristics of the piezoelectric layer, as explained earlier in section 2.2.3. The electrode design was tailored to excite the 10th-order roof tile-shaped mode (1B-mode). By varying the wiring of the electrodes, it was also possible to excite some of the lower order roof tile-shaped modes, namely the 12 to 16-modes, while the other modes were not detectable. The cantilever was submerged in the suspensions and the resonance frequency and Q factor were deduced from the impedance spectrum using the procedure explained previously. Because it cannot be avoided that some of the particles permanently adhere to the microcantilever, a measurement in pure base oil was carried out prior to the evaluation of each suspension. Doing so, the new "baseline" of the microcantilever is determined and the impact of the particle suspensions can be determined with high accuracy.

Figure 4-2 shows the measured Q factor and resonance frequency for all suspensions with (orange circles) and without (blue triangles) particles, where a significant impact on the resonance characteristics is found for the 10 wt% suspensions. On the other hand, the impact of the 5 wt% suspension is relatively low. To visualize the influence of the particles on the individual mode orders more clearly, Figure 4-3 shows the relative deviation of Q factor and resonance frequency in respect to the baseline value without particles. At 10 wt%, the frequency deviation decreases with increasing mode order, *i.e.,* resonance frequency, for all particle sizes. This behavior can be explained by the frequency-dependent penetration depth of the oscillation-induced fluid flow around the cantilever, as discussed in section 4.1.1. With increasing frequency, the penetration depth decreases, resulting in a lower interaction volume of the cantilever with the surrounding liquid. Hence, less particles are affected by the cantilever oscillation, reducing their impact on viscous damping. The effect of decreasing interaction volume was also

[7] Sicastar®, micromod Partikeltechnologie GmbH, Rostock, Germany

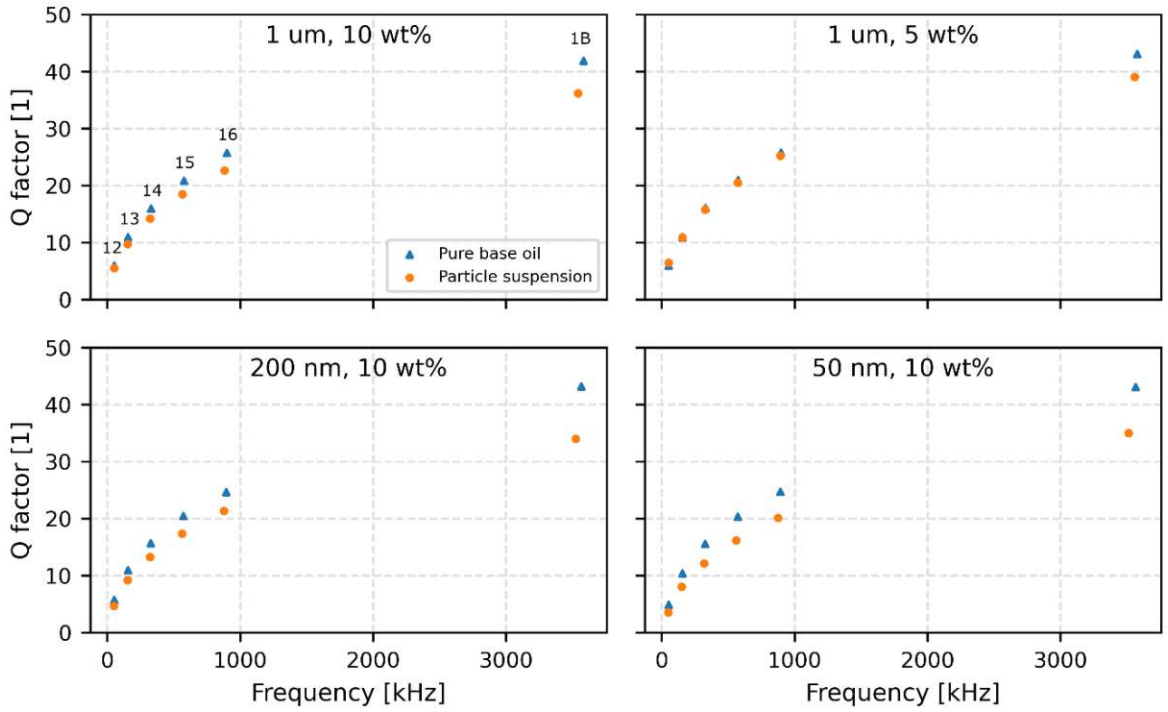

Figure 4-2: Measured resonance frequency and Q factor of an oscillating microcantilever (12-16 & 1B roof tile-shaped mode) for different particle sizes and concentrations in base oil (orange circles). For all tested concentrations and particle sizes a deviation of the resonance frequency and Q factor from the values in pure base oil (blue triangles) is measured.

observed for pure liquids, where the resonance frequency of the submerged cantilever asymptotically approaches the vacuum resonance frequency with increasing mode order [193].

In good agreement with the discussion above, the highest deviation in resonance frequency and Q factor was measured for the smallest particles with a size of 50 nm. However, for a given mode order there was only a small difference in the resonance frequency deviation for the 200 nm and 1 µm particles, whereas the Q factor showed a strong dependence on the particle size. This is in accordance with literature, where it was shown that the Q factor is much more sensitive to changes of the fluid viscosity and density, compared to the resonance frequency [131]. The Q factor deviation depicted in Figure 4-3b shows a distinct dependence on the mode order for the 50 nm and 200 nm particles, whereas no clear trend was observable for the 1 µm particles. However, the measurements of the 1B-mode suggest that the damping increases again for higher mode orders. This phenomenon was investigated in another study for the roof tile eigenmodes [132]. It was found that these additional losses are caused by the fluid compressibility (sound dissipation) when a fluid and geometry dependent critical mode order is exceeded. The results for the 5 wt% suspension showed no significant trend, hence the influence on the cantilever oscillation can be considered negligible in comparison to other effects, such as temperature variations of the oil.

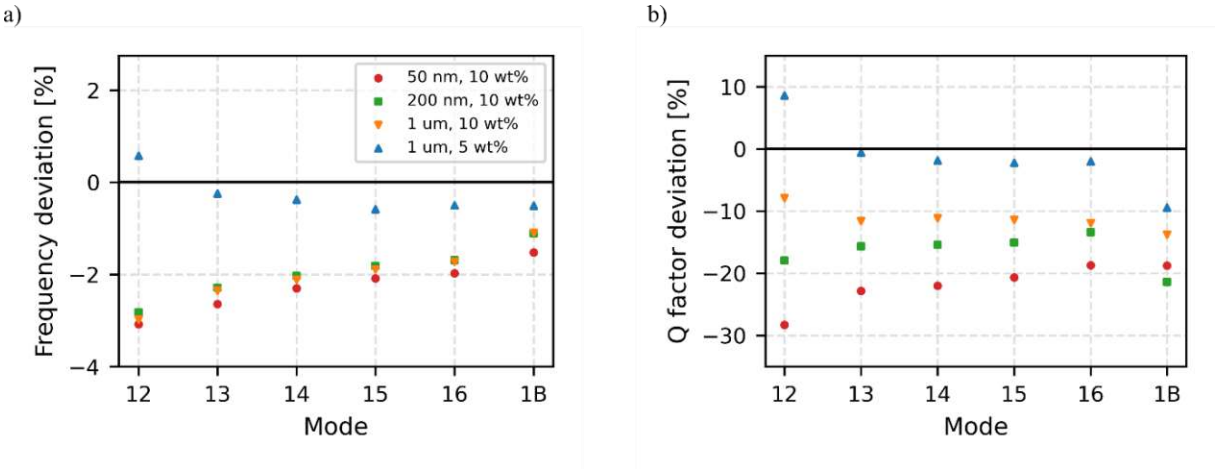

Figure 4-3: Measured deviations of the (a) resonance frequency and (b) Q factor due to the particles in the base oil, relative to the values in pure base oil.

The results in this section showed the effect of suspended particles on the resonance characteristics can be detected using the roof tile-shaped modes of microcantilevers. However, the concentrations used in these experiments are very high compared to what is expected in industrial applications. As an example, the typical concentration of wear particles in lubricating oils is in the range of a few parts-per-million [194]. Referring to equation 4.16, it can be concluded that the influence of suspended particles on the resonance characteristics is negligible in most practical applications and the particle-induced changes of viscosity and density cannot be used to detect the presence of particles in lubricating oils. New methods are needed to reliably detect suspended particles in lubricating oils using microcantilevers. The following sections present two novel sensors capable of selectively detecting metallic wear particles and thermally-oxidative varnish particles found in lubricating oils in typically encountered concentrations.

4.2 MEMS-based sensor for the detection of ferrous particles suspended in liquids

Parts of this section were published in [195], [196] *and* [197].

4.2.1 Introduction

While proper lubrication reduces friction between moving system components significantly, it cannot fully avoid wear during the operation of machinery. Especially during start-up and run-down, bearings, pistons and other machine parts may not be sufficiently lubricated due to lower oil pressure. This results in the formation of metallic wear particles that are flushed away by the oil stream and distributed in the oil circuit [21]. In the previous section it was concluded that the effect of particles on viscosity and density is too low for commonly encountered concentrations, so that monitoring these two parameters is not suitable to reliably detect particle contamination. Furthermore, especially the viscosity can be influenced by many other processes, such as temperature variations and fuel contamination of the oil, which makes it difficult to assign the measured variations of this parameter to a single source [198].

Because many machine parts are made of steel, ferrous wear debris is the most prominent type of wear particles found in lubricating oil. Depending on the degree of wear loading, the particle size can reach values up to several hundred micrometers [38]. For predictive maintenance, the detection of even smaller wear debris particles is of utmost importance for the early detection of abnormal conditions in lubricated machinery [36]. In this section of the thesis, a novel sensor for the detection of ferrous particles in liquids is presented. First, the basic sensor principle and underlying physical mechanisms are explained. An evaluation of the forces acting on the particles is given that allows for an estimation of the principle working range in terms of the detectable particle size. The functionality of the sensor is shown by exposing it to an artificially particle-contaminated liquid and measuring the mass-induced resonance frequency shift. These results allow for the determination of the accumulated particle mass, mass responsivity and limit of detection of the novel MEMS sensor.

4.2.2 Sensor principle and design

The sensor presented here is based on a resonantly excited microcantilever, which operates fully submerged in the liquid of interest. A planar electromagnetic coil is integrated on the cantilever surface to attract particles in the liquid via magnetophoresis. The accumulation on the sensor surface leads to a shift of the mechanical resonance frequency, which is used to deduce the accumulated particle mass. The following section gives a brief introduction to the principle of magnetophoresis, the design of the planar coils and a derivation of the theoretical detection range.

4.2.2.1 Manipulation of ferrous particles by magnetophoresis

The proposed sensor combines the principle of resonant mass detection with the accumulation of ferrous particles using magnetophoresis (MAP). Magnetophoresis is the phenomenon describing the force that is exerted on a magnetic particle in the presence of an external magnetic field gradient. The governing equation for the MAP force is

$$\vec{F}_{MAP} = \frac{1}{2}\frac{\Delta\chi V_P}{\mu_0}\vec{\nabla}B^2 \,, \tag{4.17}$$

with the particle volume V_P, the magnetic susceptibility of the particle relative to the surrounding fluid $\Delta\chi$ and the magnetic field constant μ_0 [199]. The last term $\vec{\nabla}B^2$ in equation 4.17 shows that the MAP force is proportional to the gradient of the magnetic flux density squared. Therefore, force is only exerted to the particle in case of local magnetic field inhomogeneities, whereas no force is observable for homogenous magnetic fields. The magnetic field needed to manipulate particles is usually generated by tailored magnetic micro-actuator elements, in the form of a planar coil, as depicted in Figure 4-4.

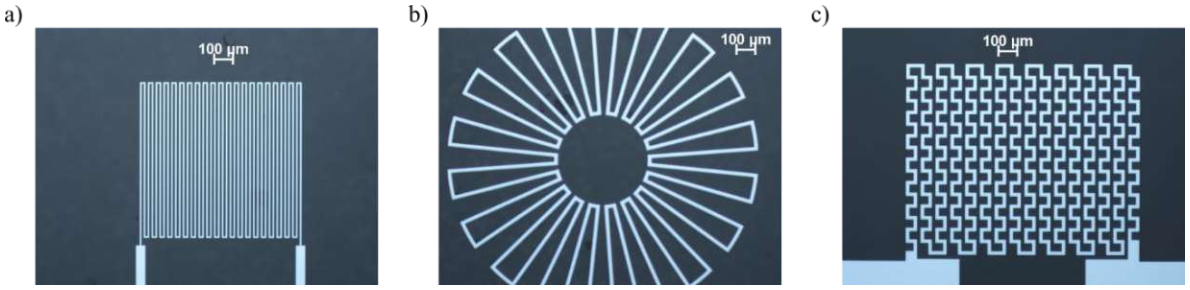

Figure 4-4: Typical planar coil geometries for magnetophoresis applications: a) meander design, b) Rosette-design, c) mesh shaped design [200].

One of the main applications for MAP is the manipulation of biological entities that are labeled with magnetic microbeads. This allows for the magnetic trapping of pathogens for diagnostics, the separation of substances from fluids or for the selective transport of substances utilized in magnetic drug delivery systems. The main advantages of MAP are the simple integration into a microfluidic system and the tunable magnetic field that can easily be adapted for the targeted application. In a comprehensive study, Ramadan *et al.* investigated the performance of different coil geometries for the accumulation of magnetic particles [200]. The highest field gradient and therefore magnetophoretic force was found for the mesh-shaped coil as depicted Figure 4-4c. Therefore, this design was adapted and integrated on the cantilever sensor surface, as presented in the next section (cf. Figure 4-6). Section 4.1 showed that the particle experiences a fluidic drag force when it moves through the liquid. The magnetophoretic force must therefore exceed this drag force to successfully accumulate particles on the sensor surface. To verify the feasibility of the proposed sensor concept, an assessment of the forces on the particles and an estimate of the sensor detection range is given below.

4.2.2.2 Evaluation of the sensor detection range

There are three main forces acting on a suspended particle: the drag force, induced by the movement of the particle, as well as the gravitational and buoyancy force, leading to sedimentation and ascending of the particles. However, in the typical experimental time span, no significant sedimentation or ascending of the particles was observed. Hence, to evaluate the sensor detection range, only the drag force and the magnetophoretic force were considered. The resulting force balance equation for a suspended particle of mass m_P

$$m_P \frac{dv}{dt} = F_{MAP} - F_{Drag} \tag{4.18}$$

implies that the magnetophoretic force F_{MAP} has to exceed the drag force F_{Drag} to successfully accelerate $\left(\frac{dv}{dt}\right)$ the particles towards the sensor surface in order to accumulate them (Figure 4-5a). While the drag force is proportional to the radius R of the particle ($F_{Drag} \propto R$), the MAP force scales with the particle volume ($F_{MAP} \propto R^3$). The drag force is therefore dominant for very small particles, inhibiting the accumulation due to the MAP-force. Hence, the lower size limit is given by the value of R, where both forces are equal.

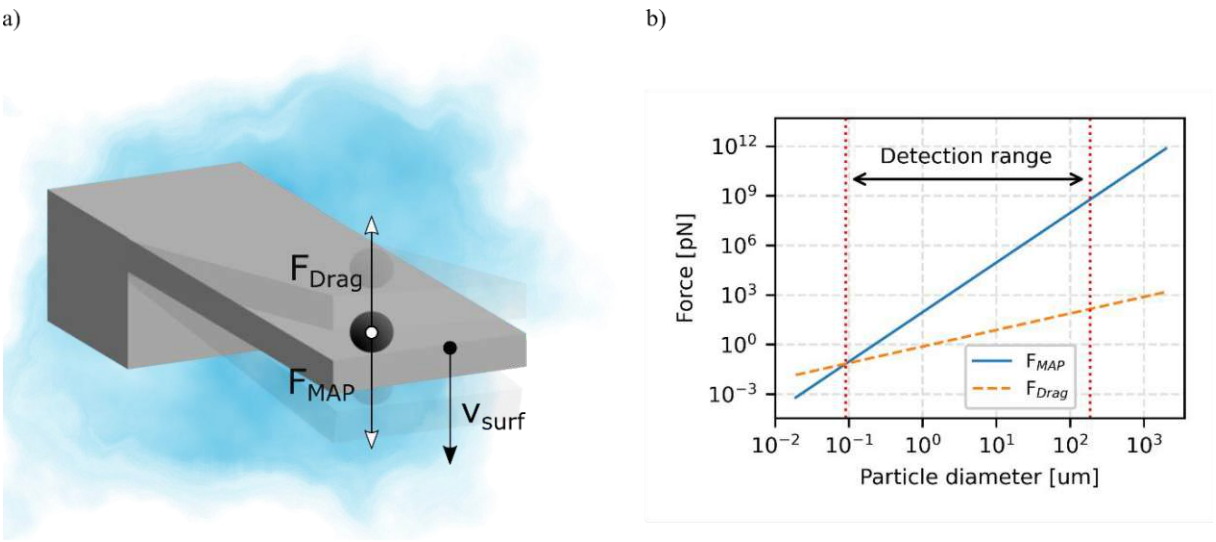

Figure 4-5: (a) Forces acting on a particle that is attached on the surface of a resonating microcantilever: The drag force F_{drag} is proportional to the velocity of the particle and hence cantilever surface. The magnetophoretic force F_{MAP} has to exceed the drag force to attract the particle. (b) Visualization of the size dependence of the magnetophoretic force (solid) and drag force (dashed) acting on a ferrous particle. The vertical doted lines show the particle size range where accumulation on the cantilever surface is possible from these basic considerations.

The magnetophoretic force was estimated by means of finite element analysis using the magnetic field interface of COMSOL Multiphysics. The magnetic field distribution of the coil as depicted in Figure 4-6b was analyzed for coil current of 150 mA, which was a typical value used in the experiments and is well below the experimentally determined maximum current load of approximately 200 mA. The magnetophoretic force directly above the coil surface was calculated in dependence of the particle diameter by applying equation 4.17 and using $\Delta\chi = 3.076$ for iron-oxide particles in deionized water. This material combination was later used as a model system for a particle-contaminated lubricant.

The counteracting drag force can be calculated by means of the relative velocity of the particle and the surrounding fluid. As depicted in Figure 4-5a, the relative velocity of a particle on the cantilever surface is approximately equal to the velocity of vibrating surface. To determine the latter value, the sensor was immersed in deionized water and was driven at resonance by a chirp signal with a bandwidth of 40 kHz and an amplitude of 500 mV, as described in section 4.2.3. For the 8th order roof tile-shaped mode, a maximum velocity of v_{surf} = 80 µm/s was found and is used to calculate the size-dependent drag force using equation 4.15.

Figure 4-5b shows the magnetophoretic force and the drag force in dependence of the particle diameter. The forces are equal for particles with a diameter of approximately 90 nm, defining the lower limit of detection. The upper limit of detection is given by the condition that the mass of the particle is negligible compared to the total oscillating mass ($\Delta m \ll M$). For particles that do not fulfill this condition, the relationship between the particle mass and resonance frequency shift is non-linear and therefore equation 3.1 cannot be applied. Given the oscillating mass M as derived later in section 4.2.3, the upper size limit for particles is calculated to be approximately 185 µm, ensuring that Δm is at least one order of magnitude lower than M. Based on these assumptions, the range where particles can be accumulated

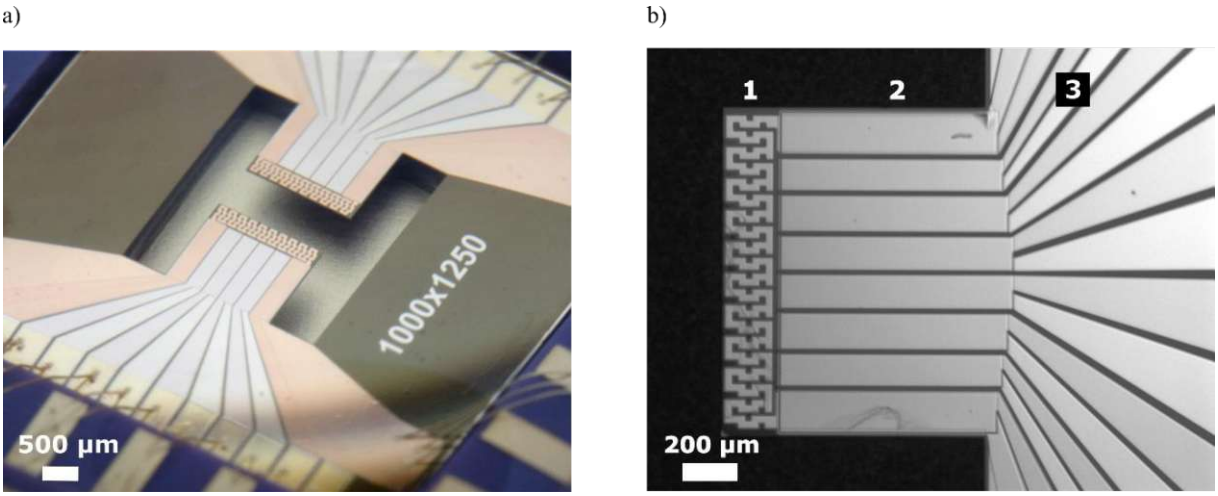

Figure 4-6: (a) Optical micrograph of the MEMS sensor, consisting of two identical microcantilevers with planar coils integrated close to the free end, (b) Detailed view: The microcantilever (2) is fixed to a substrate (3), where the electrodes are connected to the bond pads. The planar electromagnetic coil (1) accumulates the ferrous particles during operation.

spans over three orders of magnitude. However, this assessment does not consider the actual measurement of the resonance characteristics and only gives information about which particle sizes can be generally manipulated by MAP. In order to give an estimation up to which size particles can be detected individually, *i.e.,* the limit of detection, a closer look at the experimental setup is necessary and is presented in section 4.2.4

4.2.2.3 Sensor design and fabrication

This section describes the design and fabrication of the novel MEMS sensor. Figure 4-6a shows a micrograph of a finished sensor. The sensor chip (6x6 mm^2) consists of two identical piezoelectrically-driven silicon microcantilevers, fixed to one substrate. As explained in section 2.2.3, the patterned electrode design is optimized to excite the cantilever in the 8^{th}-order of the roof tile-shaped eigenmode (19 mode). The detailed view in Figure 4-6b shows the design of the mesh-shaped planer coil, located close to the free end of the cantilever. In the following, the process steps to fabricate the sensor are described.

The MEMS sensors were fabricated in the cleanroom at ISAS/TU Wien from a silicon-on-insulator (SOI) wafer with a device layer thickness of 20 µm, defining the thickness of the cantilevers. A 250 nm silicon oxide layer followed by 80 nm silicon nitride on both sides of the wafer, deposited by the manufacturer for stress compensation, acts as electrical insulation of the subsequently deposited functional layers to the substrate. The piezoelectric stack consists of a 620 nm reactive sputter-deposited aluminum nitride layer, sandwiched between vapor-deposited gold electrodes. To overcome the low adhesion of the gold electrodes to the silicon nitride insulation on the SOI wafer, a 50 nm titanium layer was deposited prior to the gold deposition. All elements of the piezoelectric stack were structured by standard lift off-technique, where the same resist pattern was used to deposit the AlN layer and the top gold electrode (Figure 4-7a-b).

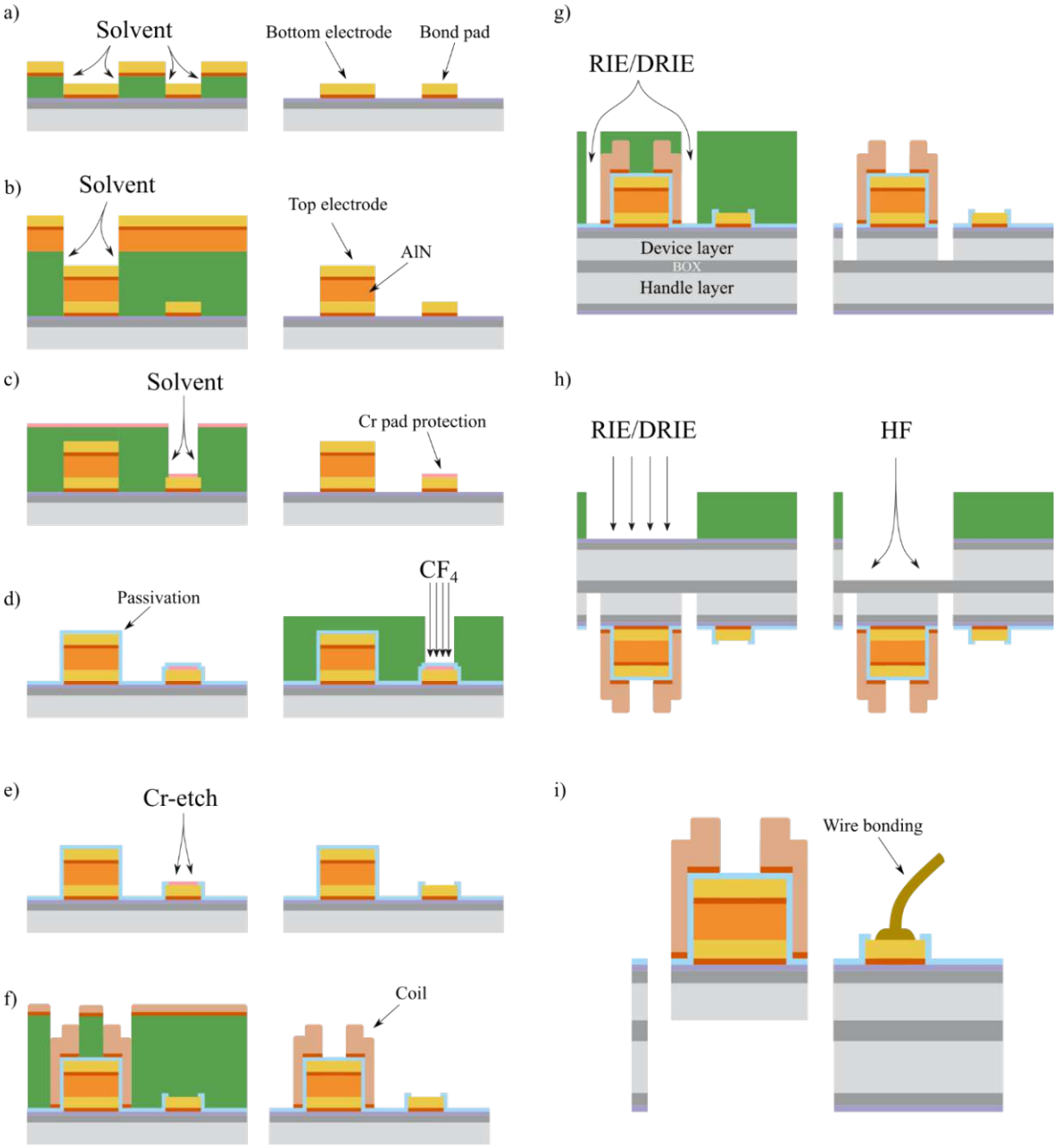

Figure 4-7: Cantilever fabrication process (for clarity, the fabrication of a cantilever without pattered striped electrodes is shown here): (a) Deposition of the bottom electrode and bond pads. (b) Deposition of the piezoelectric AlN layer and the top electrode. (c) Patterning of the chromium protective layer on the bond pads. (d) PECVD deposition of the passivation layer and subsequent removal on the bond pads. (e)Wet-chemical etching to remove the Cr pad protection. (f) Structuring of the planar coils on the cantilever surface via thermal evaporation of copper. (g) Front side release by Bosch etching the device layer of the SOI wafer. (h) Back side release by Bosch-etching and a subsequent removal of the buried oxide by HF. (i) The finished device is packaged and wire bonding is used to establish the electrical connections. Sizes not to scale.

A silicon nitride (SiN_x) passivation layer was deposited on top of the piezoelectric stack using a PECVD process to isolate the electrodes from the planar coil. Because the bond pads must not be passivated, a 100 nm Cr layer is used to cover the pads prior to the SiN_x depositon. After depositing the passivation layer, the passivation is opened, and the Cr layer is removed using perchloric acid and ceric ammonium nitrate to expose the bond pad (Figure 4-7c-e).

Because the planar coil must handle high current loads, a 1 µm copper layer was deposited on the passivation layer using thermal evaporation. Again, a 50 nm chromium layer is used prior to the deposition of copper to improve the adhesion to the underlying silicon nitride. The planar coil is capped with a 100 nm gold layer to protect the copper from oxidation (Figure 4-7f).

The length and width of the cantilevers were 1000 µm and 1250 µm, respectively, as defined by deep reactive ion etching of the SOI wafer device layer and subsequent patterning of the handle layer. Finally, the cantilevers were released by etching the exposed buried oxide using hydrofluoric acid (Figure 4-7g-h). After separating, the sensor chips are mounted in a 24-pin dual in-line package (DIP) and the electrodes and planar coils of both cantilevers were connected to the pins through wire bonding (Figure 4-7i).

4.2.3 Detection of ferrous particles in liquid environments

4.2.3.1 Sensor characterization setup and methods

The experimental setup used to test the sensor is depicted in Figure 4-8. The sensor was mounted in a 24-pin dual in-line package (DIP) and the electrodes and planar coils of both cantilevers were connected to the pins of the package using wire bonding. The MEMS sensor was positioned below a laser-Doppler vibrometer (LDV, Polytec MSA 500) and the electrodes of both cantilevers were connected to a signal generator to excite the 8th order roof tile-shaped mode (19 mode) using a chirp signal with a bandwidth of 40 kHz. The use of an optical measurement technique for determining the vibrational characteristics was necessary, because the crosstalk between the coil current and the piezoelectric elements rendered a piezoelectric read-out, as described in section 2.2.3, impossible. The planar coil of one cantilever was loaded with an electric current of 150 mA to generate the magnetic field for particle accumulation. This cantilever is called the *active* cantilever. The planar coil of the second cantilever on the sensor chip was not powered, which serves as the *reference* cantilever, as described below.

The liquid containing the particles was carefully prepared by dispersing iron oxide (Fe_3O_4) nanoparticles[8] with a hydrodynamic diameter of 250 nm in deionized water. This combination was chosen as a model system because (hydrophobic) iron oxide particles dispersed in oil were not available. By diluting the dispersion provided by the manufacturer with deionized water, the final concentration was adjusted to 350 µg/ml (350 ppm). Before starting the measurements, the dispersion was applied to the sensor with a pipette so that both, the active and the reference cantilever were submerged completely.

[8] Micromod Iron oxide particles, www.micromod.de, Rostock, Germany

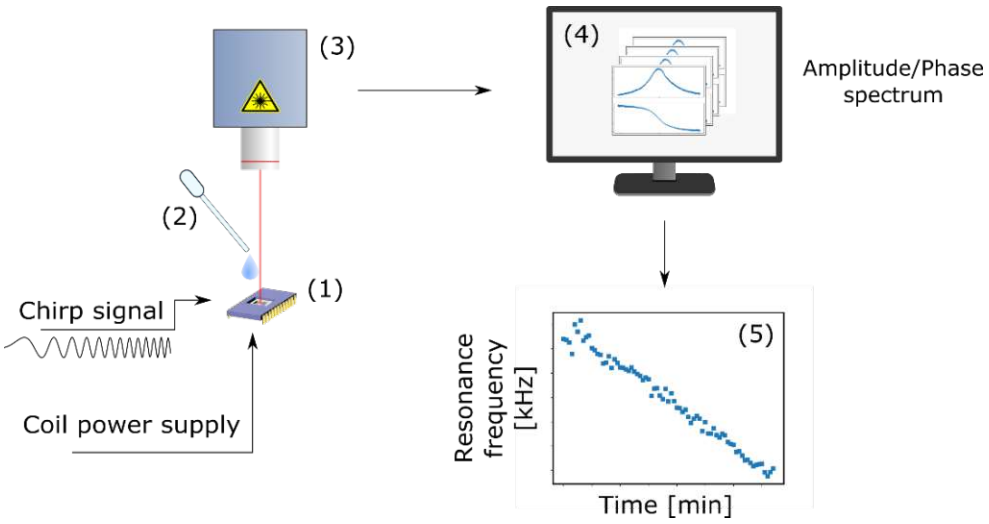

Figure 4-8: Experimental setup for the characterization of the ferrous particle sensor. The sensor chip is glued into a 24-pin DIP package (1) and a chirp signal is used to excite the vibration of the cantilevers while the planar electromagnetic coil of the active cantilever is connected to a DC voltage supply. The particle-loaded liquid is applied to the MEMS sensor using a pipette (2) and a laser-Doppler vibrometer is used to record the amplitude and phase spectrum to determine the resonance frequency (3) for a duration of approximately 120 min. The resonance frequency is then determined and plotted in dependence of the measurement time (5).

The LDV was used to record the amplitude and phase spectra of both cantilevers in intervals of 75 s. A least square algorithm was applied to fit the phase function from section 2.1.1

$$\phi(f) = \phi_0 + \arctan\left(\frac{2\zeta\left(\frac{f}{f_r}\right)}{\left(\frac{f}{f_r}\right)^2 - 1}\right) \tag{4.19}$$

to the measured phase spectra. By applying this procedure, it was possible to determine the resonance frequency of both cantilevers with a standard deviation of 50 Hz.

Besides active particle accumulation, the resonance frequency $f_{r,Act}$ of the active cantilever is also influenced by randomly adsorbed particles and temperature-induced variations of fluid properties. Hence, a differential measurement scheme was employed by taking the shift in resonance frequency $f_{r,Ref}$ of the reference cantilever into account. Since this cantilever does not actively accumulate particles but is influenced only by the spurious effects described above, it is possible to cancel them out during the measurement, especially as it is arranged close to the active cantilever. The difference of the resonance frequency shifts of the active and reference cantilever is the *differential* frequency shift, which is solely induced by the active accumulation of the ferrous particles:

$$\Delta f = \Delta f_{Act} - \Delta f_{Ref} \tag{4.20}$$

where Δf_{Act} and Δf_{Ref} are the *as-measured* resonance frequency shifts of the active and reference cantilever at a given time, respectively.

4.2.3.2 Sensor characterization in a particle-contaminated liquid

Using the measurement procedure described above, the sensor response to the above-mentioned Fe_3O_4-particle suspension was recorded for a duration of 120 min. The variation of the resonance frequency of the active and reference cantilever in dependence of the measurement time is depicted in Figure 4-9a. After immersing the sensor in the liquid, the accumulation of the ferrous particles was started at $t = t_1$ by powering the coil of the active cantilever with a current of 150 mA. The instantaneous shift of the resonance frequency of the active cantilever to higher values results from the heating effect of the electric current and the increase of the liquid temperature close to the sensor surface. By measuring the change of electrical resistance of the planar coil, the surface temperature was calculated using the temperature coefficient of resistance of the coil material (copper, $\alpha_{20} = 3.93 \cdot 10^{-3}\ K^{-1}$). At a feeding current of 150 mA, the temperature of the coil was determined to be approximately 30°C. Note that due to the heat distributed over the substrate, also a slight increase of the resonance frequency associated with the reference cantilever is observed. The effect of the temperature on the resonance frequency was verified by measuring the resonance characteristics of a sensor, which was placed submerged in deionized water in a climate chamber. The coils were left unpowered and the ambient temperature in the climate chamber was varied, which resulted in the same resonance frequency shift to higher values as observed when powering the coil.

The gap in the frequency data in Figure 4-9a between 15 min and 20 min is due to the rapid accumulation of particles, which resulted in a loss of reflectivity of the cantilever surface, so the laser of the LDV had to be repositioned. Figure 4-10 shows optical micrographs of the sensor during the measurement cycle. After turning on the coil current for the active cantilever (right), continuous accumulation of particles close to the free end was visible, leading to a linear shift of the resonance frequency. After a measurement time of approximately 100 min the area of the planar coil was homogeneously covered by particles and a total mass-induced differential resonance frequency shift of 5916 Hz (between t_1 and t_2) was calculated using equation 4.20. During the experiment the resonance frequency of the reference

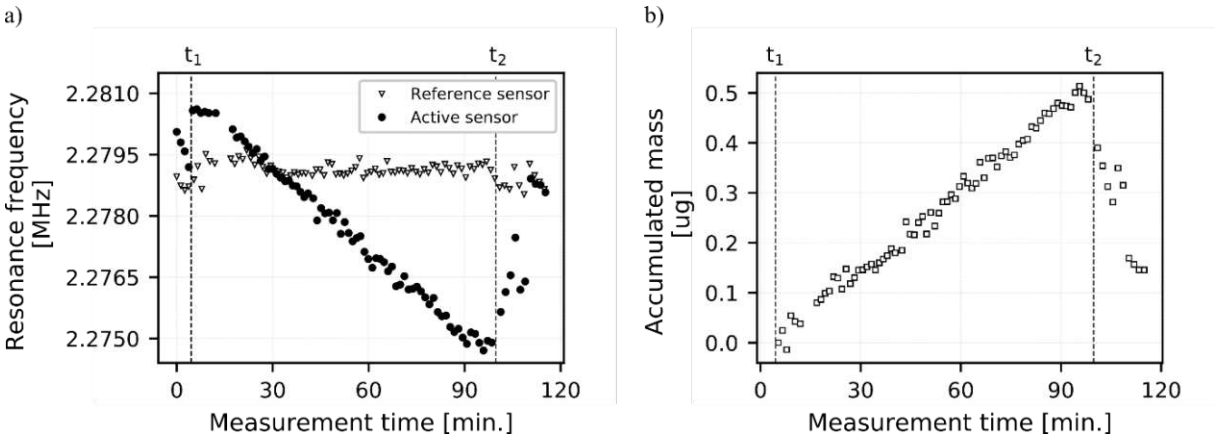

Figure 4-9 (a): Resonance frequency of the active (circle) and reference (triangle) cantilever in dependence of the measurement time. The accumulation of particles starts at t_1 by loading the planar coil with a current of 150 mA. After the current is turned off at t_2, the sensor is rinsed with fresh deionized water. (b) Accumulated particle mass during the experiment as derived by equation 4.20.

cantilever varied within a range of 825 Hz, assumably due to temperature-related changes in the viscosity. This underlines the necessity of applying a differential measurement procedure to precisely determine the mass-induced resonance frequency shift of the active cantilever. In addition, randomly distributed particle clusters are visible on both cantilevers.

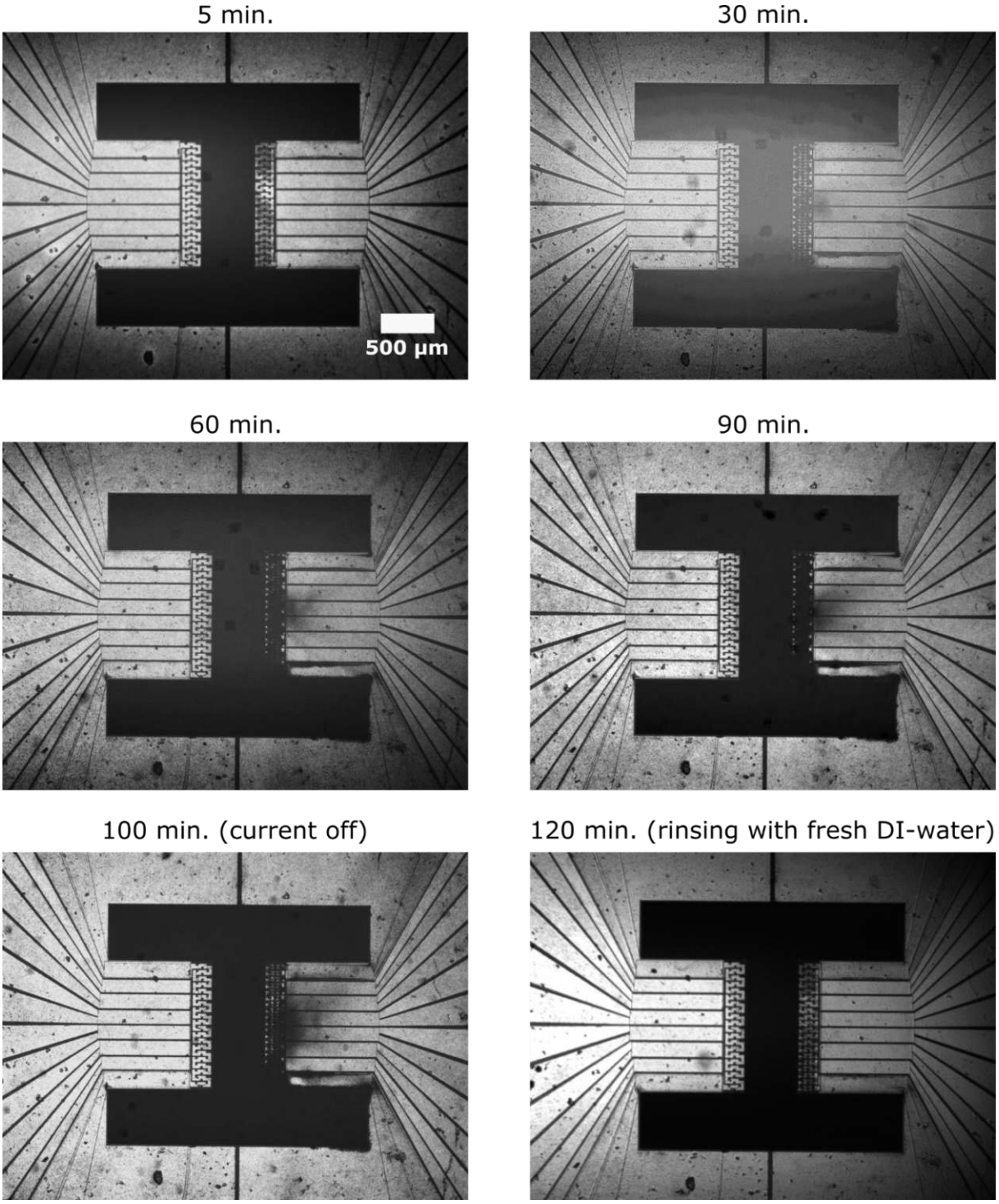

Figure 4-10: Optical micrographs of the MEMS sensor during the measurement cycle. The accumulation of particles at the tip of the active cantilever (right) is clearly visible, while the reference cantilever (left) is only covered by some randomly distributed particles.

At t = 100 min (t_2) the power supply for the planar coil was turned off and the sensor was rinsed with fresh deionized water. While most of the previously accumulated particles are washed away, some particles remained on the sensor surface, thus the resonance frequency was not fully restored to its initial value.

When using the sensor to monitor ferrous particles in liquids, the total mass of the accumulated particles is of particular interest. Because the measurement was conducted in a liquid environment, the total oscillating mass M consists of the mass of the cantilever and the mass of the fluid which is dragged along during the oscillation. As described in section 4.1.1, the resonance frequency of a cantilever which is immersed in a fluid is given by

$$f_{res} = f_{vac} \frac{1}{\sqrt{1 + \frac{m_{fluid}}{m_{cl}}}} \sqrt{1 - \frac{1}{2Q^2}} \,. \tag{4.21}$$

Here f_{vac} is the undamped resonance frequency of the cantilever in vacuum, Q is the quality factor of the oscillation, m_{cl} and m_{fluid} are the mass of the cantilever and of the dragged fluid, respectively. Because of the high quality factor ($Q \approx 250$) the last term in 4.21 can be neglected. By comparing the resonance frequency of the present sensor in deionized water f_{res} = 2.279 MHz and in vacuum f_{vac} = 3.543 MHz, the fluid mass is estimated to 106 µg which is approximately 1.4 times the mass of the cantilever, resulting in a total oscillating mass of $M \approx 180$ µg.

To derive the accumulated mass based on the measured resonance frequency shift, equation 3.1 was rearranged for Δm and the FEM-assisted procedure to derive the mode shape function $\phi(x, y)$ of the 19-mode was applied, as explained in section 3. As depicted in Figure 4-10 the particles can be assumed in a first approximation to be evenly distributed on the planar electromagnetic coil. To account for this distribution, the mode shape function was integrated across the coil area A_{coil} and the accumulated mass was derived by

$$\Delta m = -2 \frac{\Delta f}{f_{res}} M \left(\frac{1}{A_{coil}} \int_{A_{coil}} \phi^2(x, y) \, \mathrm{d}x \, \mathrm{d}y \right)^{-1} . \tag{4.22}$$

for all measurements of the resonance frequency shift and is depicted in Figure 4-9b. The accumulated mass increases linearly up to a maximum value of approximately 0.49 µg. After turning of the electromagnetic coil and rinsing the sensor with fresh deionized water, a residual mass of 0.15 µg remained on the MEMS sensor.

4.2.4 Discussion

The results in the previous section showed that the sensor is capable of detecting ferrous particles in a viscous liquid environment. A total particle mass of 0.49 µg was accumulated during a measurement

time of 100 min resulting in a differential resonance frequency shift of 5916 Hz, which corresponds to a mass responsivity $\mathcal{R}$ of 12.07 Hz/ng or 82.85 pg/Hz. Despite the large size and hence, mass of the sensor, the high resonance frequency and low viscous damping of the roof tile-shaped modes lead to a mass responsivity comparable to values of 57.2 pg/Hz and 5.5 pg/Hz at a resonance frequency of 750 kHz reported in other studies of resonant mass detection in liquid environments [79] [82]. Note that these values were obtained using a much smaller cantilever with a size of 500x100x1 μm^3, corresponding to a mass of only about 0.15% of the sensor presented in this work. This again underlines the outstanding performance of the roof tile-shaped modes for mass detection, especially in liquid environments.

For sensing purposes, the minimal detectable mass change is of particular interest. This limit of detection (LOD) can be derived by relating the smallest detectable resonance frequency shift Δf_{min} to the measured mass responsivity $\mathcal{R}$:

$$LOD = \frac{\Delta f_{min}}{\mathcal{R}_{Avg}} \tag{4.23}$$

As mentioned above, the uncertainty when determining the resonance frequency is about 50 Hz, resulting in a limit of detection of approximately 4 ng. This value corresponds to a single iron oxide particle with a diameter of about 11 µm. This value can be significantly improved by a closed loop detection scheme of the resonance frequency, *e.g.* a phase-locked loop (PLL). A first assessment using a lock-in amplifier with PLL-functionality (Zurich Instruments HF2LI) showed that the frequency resolution can be improved to 4.5 Hz, corresponding to a limit of detection of 370 pg or a single iron-oxide particle with a diameter of approximately 5 µm.

Based on these results, in order to evaluate the applicability of the novel MEMS sensor in an industrial environment, the typical particle sizes occurring in oil circuits must be examined. The size of wear debris particles is generally dependent of the machinery condition. During normal operation, the wear debris size is typically up to 10 µm [21]. When the machinery is in an abnormal condition, the size and concentration of the particles start to increase gradually. When particles of 100 µm and above are found in the lubricating oil, the machinery is in critical condition and immediate countermeasures must be taken to prevent complete failure. For predictive maintenance, that is the detection of emerging defects before they can compromise the machinery condition, it is therefore important to monitor wear debris particles well below that critical size. As described in section 1.1.1, many wear debris detection techniques were developed, which are based on the magnetic, electric, acoustic or optical properties of the particles [23] [31] [39] [201]. While some of these techniques have been commercialized, they generally offer low sensitivity which is in the range of 100 µm and above. High-sensitivity techniques such as the capacitive detection of wear debris consist of very complex structures with low throughput, limiting their feasibility for industrial applications. Compared to the techniques mentioned above, the sensor presented in this work offers a very high sensitivity down to the low µm level. It is therefore

possible to monitor wear debris particles well below the critical size of 100 µm, which allows for the early detection of abnormal wear for predictive maintenance.

However, the MEMS sensor presented in this paper has to be read out optically due to the electrical crosstalk between the integrated coil and the piezoelectric elements, hence its applicability in real industrial environments is currently limited. One possibility to minimize the crosstalk and thus enable a fully piezoelectric readout of the vibration properties is to spatially separate the integrated coil and the piezoelectric elements. This can be achieved, for example, by reducing the surface area of the electrodes, thus avoiding overlap with the coil. This approach is followed for the sensor described in the next section and achieved excellent results. Furthermore, the design of the integrated coil can be optimized to increase the magnetophoretic force and to concentrate the particles in areas of high oscillation amplitude. This leads to an extension of the application range of the sensor for even small particles and a reduction of the LOD.

In summary, this section showed the potential of using microcantilevers for the detection of ferrous wear particles in lubrication systems of industrial machinery. Because of its high mass responsivity as well as compact and robust design, the microcantilever sensor is predestined to be integrated in the harsh environment of lubrication circuits of industrial machinery, thus allowing for real-time determination of ferrous wear and abnormal operating conditions with a high local resolution due to its compact design.

4.3 MEMS sensor for monitoring oxidation-induced varnish particles in lubricating oils

Parts of this chapter were published in [202] *and* [203].

4.3.1 The varnish problem of lubricated machinery

The term "varnish" describes deposits that are created by the degradation of lubricating oils [48]. Varnish manifests itself as a thin, insoluble film that adheres to surfaces in contact with the lubricating oil. These deposits can cause various problems in lubricated machines. In bearings, varnish leads to increased friction and therefore premature wear and heat, reducing machine efficiency and accelerating the oil degradation process. Modern machinery often requires the use of oil coolers as the demand for higher efficiency and running speeds increases the thermal load of modern lubricating oils [204]. Varnish can severely restrict heat transfer in these elements, leading to an overall increase in oil temperature and thus rate of degradation. If the lubricant is used as hydraulic fluid to operate valves, the build-up of varnish in these elements can lead to total machine failure. In the worst case, the varnish can clog oil filters or supply lines, leading to unplanned shutdowns for repair.

The root cause of varnish formation is oxidative oil degradation as described in section 2.5.3. Initially, the oxidation products remain soluble in the lubricating oil, but begin to coalesce and form high molecular weight molecules as their concentration increases. Eventually, the saturation point is reached,

leading to precipitation of the now insoluble oxidation products in the form of varnish particles. Because these particles are polar by nature, they tend to agglomerate and adhere to metallic surfaces that are in contact with the lubricating oil. The tendency of an oil to form varnish deposits is directly linked to its ability of keeping impurities in soluble suspension. As described earlier, the highly refined group II and group III base oils used for modern lubricating oils show lower solubility compared to the group I-based lubricating oils used in the past. Although modern lubricating oils offer excellent oxidation resistance due to elaborated additive formulations, they are more prone to form varnish when antioxidant levels deplete during operation.

Due to the potentially disastrous consequences of varnish deposition, continuous monitoring of the oil parameters is necessary to ensure reliable and uninterrupted operation of machinery. However, the correlation of oil parameters as determined by conventional analysis techniques and the potential to form varnish deposits is still not fully understood. Several studies on the physical and chemical changes due to turbine oil degradation showed that the changes in viscosity and neutralization number are usually very small despite severe varnish deposition in the lubricated system. Changes of the infrared absorbance characteristics, as measured by FTIR, can be used to detect the formation of varnish precursors, *i.e.,* acidic species, in the oil [60]. However, due to the complex composition and interplay of the oil ingredients, the interpretation of the results is challenging for modern lubricating oils. Oxidation resistance tests such as RPVOT and TOST were initially designed for lubricants formulated with group I base oils, where good reproducibility and repeatability were found for RPVOT values of lower than 1000 min [205]. Although still used in the industry for modern lubricating oils, these oxidation resistance tests do not reflect the typical operating conditions in the field, where rapid temperature changes, localized hot spots and the entrainment of air can significantly affect the lubricating oils varnish potential. The direct detection of the varnish particles is a challenging task, as their size is usually in the range of a few micrometers and below [206]. Due to the difficulty to differentiate from other types of particles such as wear debris, conventional methods to determine the lubricant particle contamination, such as the particle-counting methods or measuring the weight of filter residues, are often not able to adequately determine the concentration of these oxidation products. Another difficulty arises from the temperature-dependent solubility of the varnish particles in the lubricating oil. Since the oil analysis is usually carried out at temperatures different from those in the machinery, the measured particle concentration may not correspond to the concentration that is found in the machinery during operation [207]. A relatively new procedure to determine the varnish potential of turbine oils is the MPC (Membrane Patch Colorimetry) test [208]. Oil is diluted with a non-polar solvent to decrease the solubility and promote the precipitation of the polar varnish particles. The oil-solvent mixture is then filtered through a membrane, where the insoluble varnish particles change the color of the membrane patch. The hue and intensity of the membrane color can then be used to determine the varnish potential of the filtered oil. Although this technique is used in industry, the results are dependent on the sample preparation prior to filtration, the temperature during filtration and the solvent

used to dilute the sample, resulting in poor repeatability [209]. Furthermore, since solubility changes as the oil is diluted, the results may not reflect the actual varnish potential of the oil during operation.

It is clear that the conventional oil analysis methods are not suited to quantitatively detect varnish particles with a quantitative approach in lubricating oils under the real conditions encountered during the operation of the machine. While useful for estimating the severity of oil deterioration, they cannot reliably determine the actual varnishing potential of the lubricating oil in use. A new sensor system for the detection of varnish particles should therefore meet two criteria. First, the sensor should detect the particles directly and not only changes in oil properties that are indicative of the formation of particles. Second, it should be able to work under the harsh operating conditions "on board" of the machine. This would allow the sensor to be integrated into the oil circuit, thus eliminating problems caused by varying solubility due to different temperatures during analysis and allowing for a real-time and continuous detection of varnish particles.

To meet the above requirements, a novel MEMS sensor for the detection of varnish particles in lubricating oils was developed. The sensor is based on a piezoelectrically excited microcantilever that operates fully immersed in the particle-contaminated fluid. The sensor is fabricated in standard silicon microtechnology and therefore offers high robustness even in harsh environments such as the oil circuit of lubricated machinery. Because the varnish particles are polar, they can be manipulated in an external electric field via the principle of dielectrophoresis (DEP) [48]. For this purpose, tailored interdigitated electrodes are integrated on the cantilever surface to promote the accumulation of particles. The additional mass introduced by the particles leads to a shift of the mechanical resonance frequency, thus indicating the particle contamination of the fluid time resolved, even during their emergence. In the following section, the controlled varnish deposition using DEP is explained in detail, followed by an in-depth characterization of the accumulated varnish particles using SEM-EDX. After presenting the specific sensor fabrication and design aspects, the detection of varnish particles in lubricating oil under harsh conditions is demonstrated in the lab and the sensor performance is benchmarked against state-of-the-art techniques for determining varnish potential.

4.3.2 Study of varnish formation mechanisms

4.3.2.1 Varnish affinity to materials used in MEMS technology

The discussion above shows that the oxidation products remain soluble in the oil until the concentration reaches the saturation point. At this point, the varnish particles precipitate and start to deposit in the lubricated system. To use a sensor for the early detection of such particles, their affinity to the sensor surface should be much higher compared to other components of the lubrication system. Otherwise, the sensor would not be able to respond until varnish deposition has already taken place in the rest of the system. To examine if there is any distinct affinity of the varnish particles to a particular material used in MEMS technology, four representative materials where chosen: silicon, silicon carbide, silicon oxide and silicon nitride. Of each material, four quadratic slices with a side length of 12 mm were prepared,

and their weight were determined using a microscale. The samples were then immersed in commercially available turbine oil and placed in a temperature-controlled climate chamber. For comparison, five steel plates were also immersed in the oil. The oil was heated up to 150°C to accelerate the aging process as described in section 2.5.5 for a duration of two weeks. After this temperature treatment, the samples were removed from the oil and rinsed thoroughly using n-heptane. This treatment removes residual oil, while the deposited varnish stays unaffected. The samples were weighted again to determine the mass of the deposited varnish. Table 4-1 shows that there is no distinct material with exceptionally high increase in mass compared to the steel sample. It can therefore be assumed that the deposition rate of varnish on a MEMS cantilever integrated into the oil circuit is the same as for the rest of the system. In order to ensure high sensitivity and thus detect varnish deposits at an early stage, the accumulation of varnish particles on the sensor surface must be promoted.

Table 4-1: Determination of the mass increase due to deposited varnish for materials applied in MEMS technology and a reference sample made of steel.

Sample	*Mass before [mg]*	*Mass after [mg]*	*Percent change*
Steel			
1	352.59	352.72	0.04
2	336.46	336.55	0.03
3	334.9	335.2	0.09
4	335.61	335.9	0.09
Mean	-	-	**0.063**
Si			
1	116.24	116.29	0.04
2	117.47	117.6	0.11
3	116.93	116.99	0.05
4	117	117.05	0.04
Mean	-	-	**0.06**
SiC			
1	120.1	120.14	0.03
2	119.67	119.69	0.02
3	120.06	120.19	0.11
4	120.13	120.13	0
Mean	-	-	**0.04**
SiO_2			
1	118.42	118.47	0.04
2	119.22	119.26	0.03
3	119.18	119.35	0.14
4	118.53	118.53	0
Mean	-	-	**0.053**
SiN_x			
1	117.77	117.87	0.08
2	118.28	118.29	0.01
3	118.12	118.14	0.02
4	117.56	117.65	0.08
Mean	-	-	**0.048**

4.3.2.2 Controlled varnish particle deposition using dielectrophoresis

The results of the last section suggest that the increase of the affinity of the varnish particles to the sensor surface significantly improves the early detection of an impending deposit formation. In the course of this thesis a novel way was found to accumulate varnish particles on the sensor surface in a controlled manner before the significant formation of deposits in the lubricated system. For this purpose, the principle of dielectrophoresis is used, *i.e.,* the phenomenon of a force being exerted on a dielectric particle that is exposed to an electric field gradient. When a dielectric particle is subjected to an external electric field it is polarized in a way that the induced electric dipole aligns with the electric field. In a uniform electric field, the Coulombic force on the positive and negative charge of the dipole is of equal magnitude and directed in opposite directions, hence no net force is observed (Figure 4-11a). On the other hand, if the external electric field is locally inhomogeneous, the force on one side of the dipole prevails, resulting in a net force acting on the particle (Figure 4-11b). The governing equation for the dielectrophoretic force on a particle with the radius R is

$$F_{DEP} = 2\pi\epsilon_{fl}R^3 Re[K(\omega)]\nabla E^2 \qquad 4.24$$

with the gradient of the external electric field intensity squared ∇E^2 and $Re[K(\omega)]$ being the real part of the frequency-dependent Clausius-Mossotti (CM) equation

$$K(\omega) = \frac{(\epsilon_p - \epsilon_{fl}) + {}^{i}/_{\omega}\,(\sigma_p - \sigma_{fl})}{(\epsilon_p + 2\epsilon_{fl}) + {}^{i}/_{\omega}\,(\sigma_p + 2\sigma_{fl})}. \qquad 4.25$$

ϵ_p and ϵ_{fl} denote the permittivity and σ_p and σ_{fl} denote the electrical conductivity of the particle and the surrounding fluid, respectively [210].

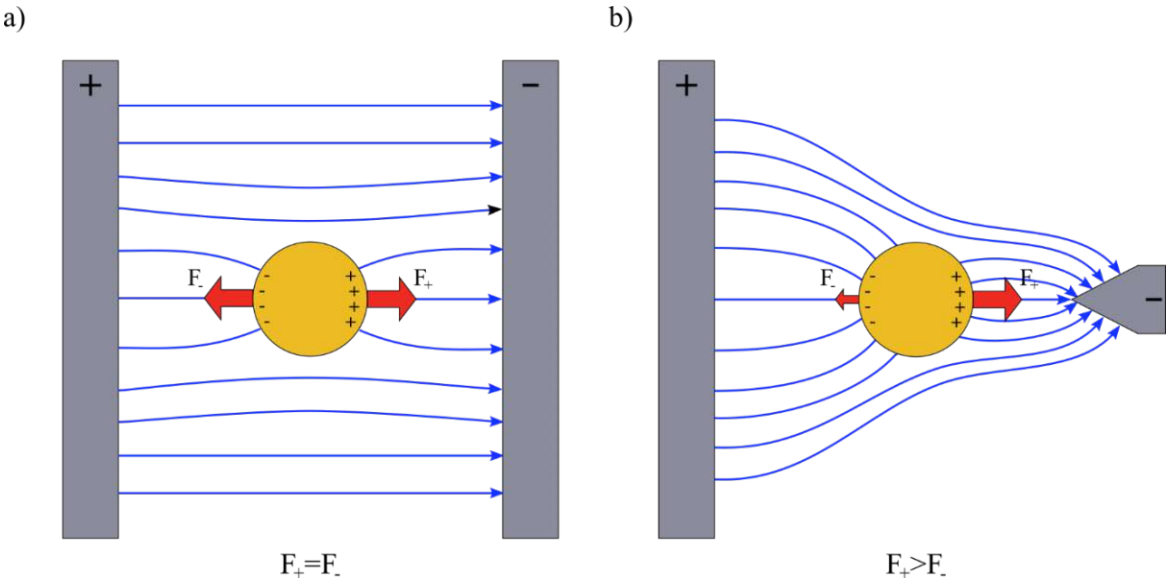

Figure 4-11: Visualization of the principle of dielectrophoresis: The particle is polarized due to the external electric field. (a): In a locally homogenous field, the forces on the positive and negative dipole charges are equal, hence no net force is exerted on the particle. (b): In a locally inhomogeneous field, the force on the force on one of the dipole charges is larger, resulting in a net force on the particle (depicted here is the case when the permittivity of the particle exceeds the permittivity of the surrounding fluid).

The electric field is generated by tailored electrode structures that are supplied with an electrical voltage. Depending on the application, there is a wide range of possible electrode arrangements, most of which can be produced using standard lithography processes. The principle of dielectrophoresis offers a wide range of applications, probably the most prominent being the separation of particles, such as biological cells, from liquids [210]. A special feature of this technique is that besides the permittivity of the particle and fluid, both magnitude and direction depend also on the frequency of the applied voltage (cf. equation 4.25). If the real part of the Clausius-Mossotti equation is negative, the particles move along the field gradient in the direction of decreasing field strength. This phenomenon is called negative dielectrophoresis, while the reverse is called positive dielectrophoresis. By appropriate choice of electrode design and electrical excitation it is therefore possible to manipulate and separate different particle types with only one structure. The principle of dielectrophoresis is ideally suited for use in the accumulation of varnish particles on a cantilever surface because the necessary structures can be easily produced using standard MEMS technologies, and the strength and type of interaction can be controlled by the applied voltage. An important point is that this technique is selective to the insoluble varnish particles and does not interact with any oil additives since the additives are found in the dissolved state within the base oil [211].

In this work a static electric field was used for accumulation of the varnish particles, hence the CM equation reduces to

$$K(\omega) = \frac{\sigma_p - \sigma_{fl}}{\sigma_p + 2\sigma_{fl}}. \qquad 4.26$$

For insulating particles ($\sigma_p \to 0$), the CM equation becomes -1/2, resulting in the final expression for the dielectrophoretic force exerted on varnish particles in a stationary electric field

$$F_{DEP} \approx -\pi \epsilon_{fl} R^3 \nabla E^2. \qquad 4.27$$

To show a proof of principle, an interdigitated electrode (IDT) structure (Figure 4-12a) was fabricated and immersed in oil that is artificially aged for 4 days at 150°C as described in section 2.5.5. A DC voltage of 30 V was applied between the interdigitated electrodes to produce an electric field and to accumulate varnish particles. After the aging process the IDT structure was removed from the oil and rinsed with n-heptane. The examination with an optical microscope shows strong deposits in the area of the electrode strips (Figure 4-12b).

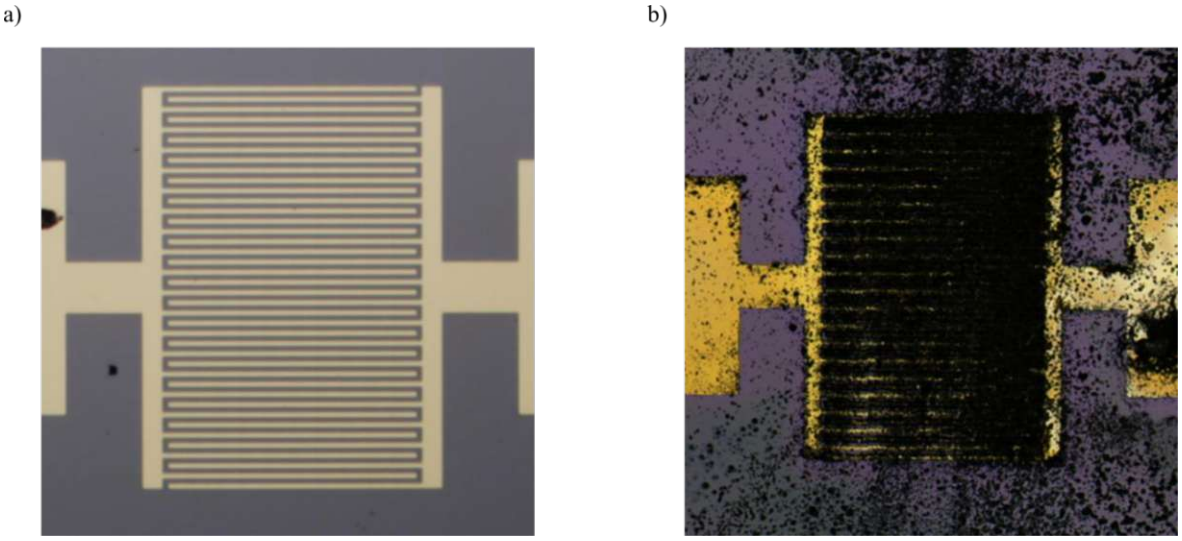

Figure 4-12: Proof of principle for the accumulation of varnish particles using dielectrophoresis: (a) a DC voltage of 30 V was applied between the strips of an interdigitated electrode structure. (b) After immersing the structure for 4 days in turbine oil at 150°C strong accumulation of varnish on and around the IDT structure is observed.

The collected particles were then examined by SEM/EDX to investigate their structure and chemical composition. In particular, it must be clarified whether the particles actually consist of oxidized oil components. The SEM micrograph in Figure 4-13 shows that the accumulated particles appear mostly spherical and form a "spongy" structure around the DEP electrodes with a narrow size distribution around a mean size of approximately 400 nm. In addition, larger deposits with an apparently denser structure are found on the electrodes. To study the chemical composition, EDX was applied at the highlighted areas in Figure 4-13a. The results are shown in Table 4-2. Both measurements show carbon and oxygen, both are attributed to base oil oxidation products. Silicon and gold, found in area 1, are attributed to the substrate and electrode material, respectively. The presence of sulfur and phosphorus is particularly noteworthy, as both elements are typical constituents of antioxidative additives. The EDX analysis therefore clearly shows the presence of oxidation products of the base oil as well as of additives, the latter, however, only in minor quantity. It was thus shown that the principle of dielectrophoresis is suitable for selectively accumulating varnish particles.

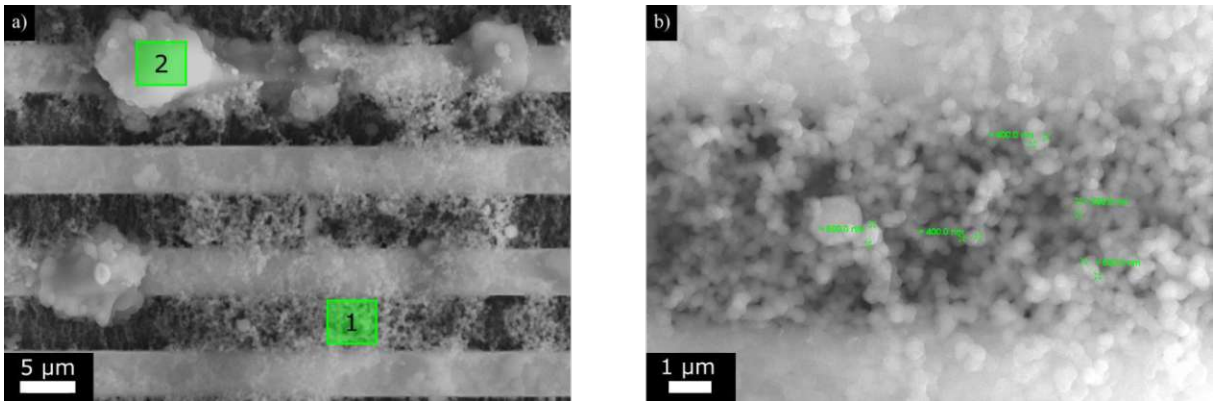

Figure 4-13: SEM images of the accumulated particles: (a) The particles appear mostly spherical and form a "spongy" structure around the DEP electrodes. EDX was used in the highlighted areas to study the chemical composition of the particles. (b) The detailed view shows a narrow size distribution around a mean size of approximately 400 nm.

Table 4-2: Results of the EDX analysis of the areas highlighted in Figure 4-13a.

Element	Area 1 (wt. %)	Area 2 (wt. %)
C	57.5	70.2
O	13.7	23
Si	19.9	1.2
P	1.9	1.2
S	0.4	4.4
Ca	0.3	-
Au	6.2	-

4.3.3 MEMS sensor design and fabrication

The MEMS sensor described in this thesis combines the principle of resonant mass detection and the manipulation of particles via dielectrophoresis, by integrating a tailored interdigitated electrode structure into the surface of a piezoelectrically driven microcantilever. During the fabrication of the sensor technical challenges occurred, which led to redesigns and gradual improvement of the MEMS sensor design. Starting from the initial design, this section presents all sensor designs and the encountered problems, respectively.

In the initial design, similar to the sensor described in section 4.2, the DEP actuator was integrated on top of the piezoelectric stack, separating both elements by an insulating SiN_x layer. The piezoelectric stack was fabricated on an insulated silicon-on-insulator (SOI) wafer by vapor deposition of gold electrodes and reactive sputtering of an AlN layer, followed by deposition of a 100 nm thick SiN_x layer using PECVD. In a last step, the DEP actuator was formed on top of the SiN_x layer by a lift-off process with gold as electrode material. As described in section 4.2, the electrical crosstalk between the integrated DEP actuator as well as occasionally occurring short circuits and low-resistance paths made the detection of the resonance frequency via impedance measurement impossible. Therefore, the SiN_x thickness was increased to 1 µm, followed by structuring the DEP actuator by a lift-off process (Figure 4.14a). However, during fabrication, partial delamination of the SiN_x layer was observed, which interferes with the subsequent processes and leads to holes in the insulation (Figure 4-14b).The poor adhesion was attributed to the high thickness of the layer of 1 µm, as similar behavior was not observed for a thickness of 100 nm, as described in section 4.2.

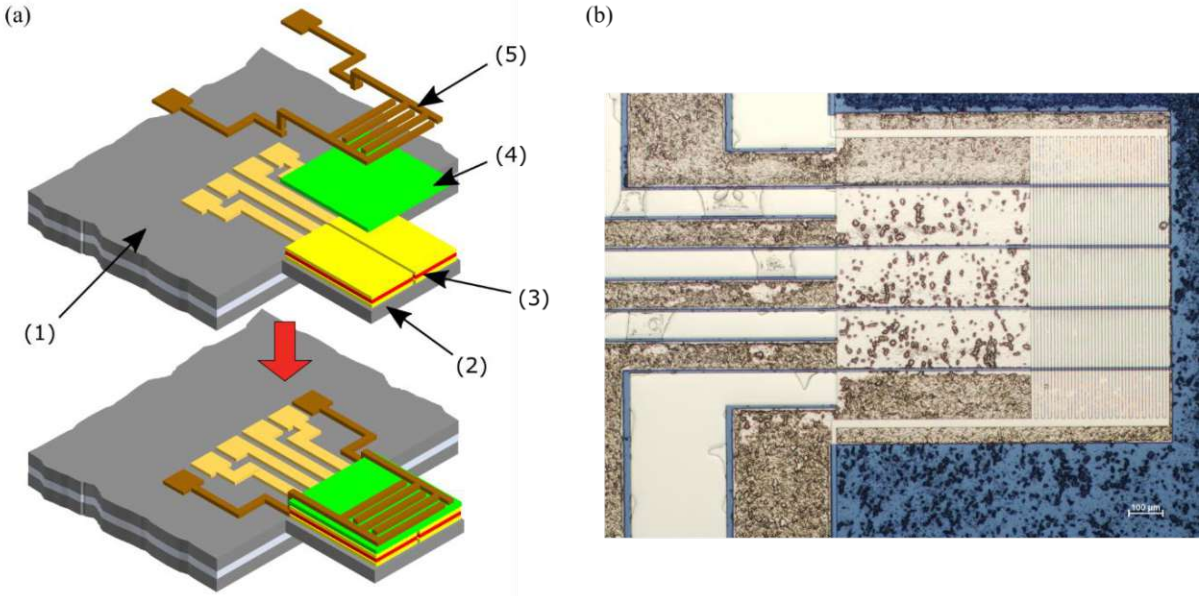

Figure 4-14: Initial design for a novel varnish particle sensor. (a) The MEMS sensor is based on a silicon microcantilever (2) that is defined by patterning the 20 µm thick device layer of a silicon-on-insulator wafer using deep reactive ion etching. The device layer is covered with an insulating 250 nm SiO_2 layer, followed by an 80 nm SiN_x layer (not drawn in figure). A piezoelectric stack, consisting of a 620 nm AlN layer that is sandwiched between 200 nm gold electrodes, is used to excite the oscillation (3). A 1 µm SiN_x layer (4) was deposited using PECVD to insulate the DEP actuator structure (5) from the gold electrodes. (b) During fabrication, the SiN_x layer locally peeled of due to internal stress, leading to electrical short-cuts between the DEP actuator and the gold electrodes.

Based on these findings, the manufacturing process was modified by discarding the full-surface insulation using SiN_x. Instead, the mask set for patterning the DEP actuator was used to structure an insulating 350 nm thick AlN layer by means of a lift-off process. The result is an insulating layer that is located exclusively below the DEP actuator (Figure 4-15). However, new problems were encountered during fabrication due to the poor adhesion of the DEP actuator material to the AlN layer, resulting in partial delamination of the DEP actuator.

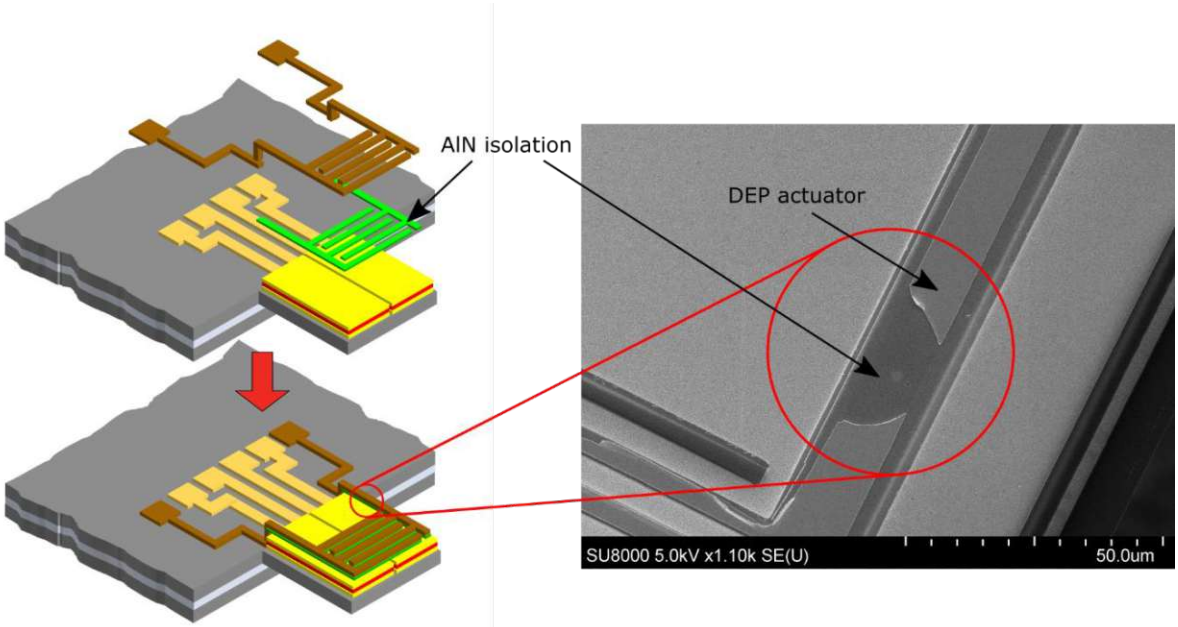

Figure 4-15: Modified sensor design with a sputtered AlN layer below the DEP actuator for electrical insulation from the gold electrodes. However, problems were encountered during fabrication due to the low adhesion of the DEP actuator material to the AlN layer, resulting in partial delamination of the DEP actuator.

Due to persisting problems regarding the electrical insulation between the piezoelectric stack and the DEP actuator, the MEMS sensor design was again revised. As a first step, any overlap between these two elements was removed by reducing the size of the piezoelectric stack. This eliminates the need for a dedicated insulation layer to electrically separate the DEP actuator from the piezoelectric stack (Figure 4-16a). Since the highest mass responsivity is found at the free end of the cantilever, the DEP actuator was integrated directly onto the silicon cantilever at this position. At the same time, the mechanical stress in this area is at a maximum, which results in the loss of a considerable part of the piezoelectric signal when the electrodes are reduced in size. Based on this trade-off, a design was chosen in which the DEP actuator covers 15% of the total surface area. By reducing the size of the piezoelectric stack, the latter is spatially separated from the DEP electrodes (Figure 4-16b). This modification simplifies the design significantly, eliminating the problems encountered with a dedicated SiN_x insulation layer.

The manufacturing process is similar to that described in section 4.2.2 except for the PECVD process to deposit the insulation layer, which is omitted in the current sensor layout. The MEMS sensor chip, consisting of two identical microcantilevers, is made from monocrystalline silicon that is patterned by deep reactive ion etching (DRIE) of a (100)-orientated silicon-on-insulator (SOI) wafer. The length and width of the cantilevers are 1000 µm and 1250 µm, respectively, while the thickness is defined to 20 µm by the SOI device layer. The cantilevers are actuated by a reactively sputter-deposited aluminum nitride (AlN) layer with a thickness of 620 nm, sandwiched between gold electrodes with a thickness of 300 nm each. The DEP actuator was deposited and structured during the fabrication of the bottom electrode, hence it consists of a 300 nm gold layer. For each DEP electrode size (see above) three designs

for the piezoelectric stack were integrated to excite the 6th (Leissa's notation: 17), 7th (18) and 8th (19) order of the roof tile-shaped eigenmode, so that a tailored electrode design is used to optimize the electrical read-out of the sensor, as depicted in Figure 4-16b.

During the redesign of the sensor, the layout of the DEP actuator was also revised. Equation 4.27 shows that the DEP force scales with the gradient of the electric field intensity squared. It is therefore desirable to promote local field inhomogeneities to maximize the force transferred to the particles. Figure 4-17a compares the ad-hoc design of the previous sensor versions with an improved design as used in the final version of the sensor. The ad-hoc design consists of interdigitated electrodes which are biased with a voltage difference between the alternating strips. In a first approximation, the electric field distribution of this geometry is uniform in the plane between the fingers, leading to a lower field gradient above the structure, therefore limiting the dielectrophoretic force. The improved device shows a significant increase of the local field inhomogeneity and therefore dielectrophoretic force by additional interlocking of the individual electrode strips. Figure 4-16b shows the improved DEP actuator design integrated at the free end of the microcantilever. An optical micrograph of the finished sensor chip in the final design is depicted in Figure 4-17b.

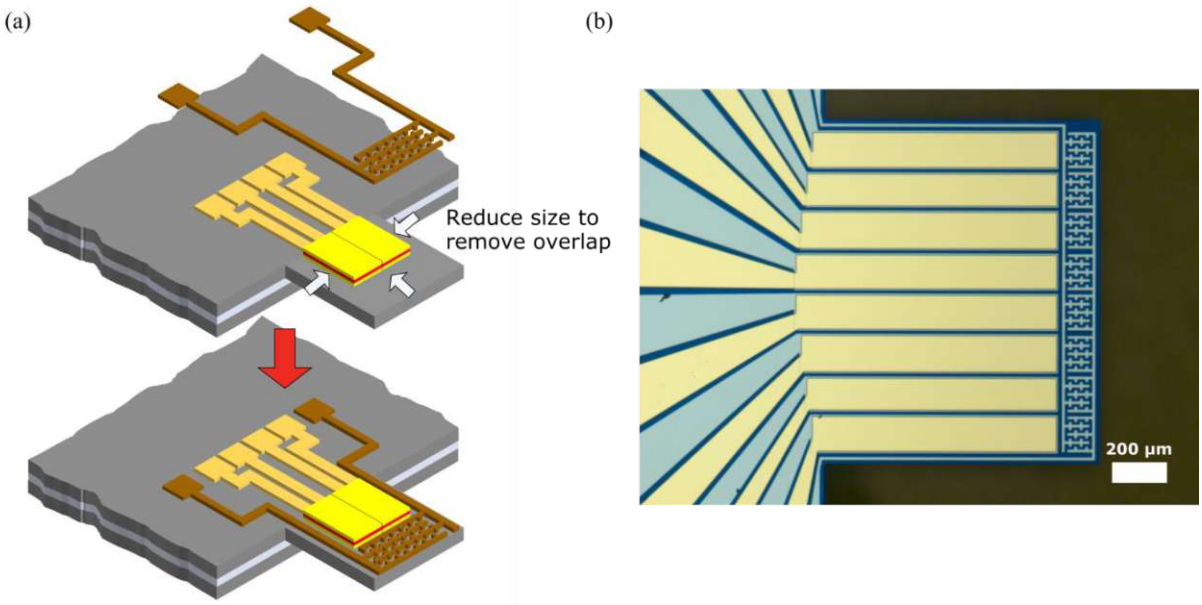

Figure 4-16: Final sensor design: (a) the size of the piezoelectric stack was reduced to eliminate any spatial overlap with the DEP actuator. This eliminates the problematic manufacturing of a dedicated insulation layer and avoids adhesion problems. (b) Optical microscope image of the finished microcantilever where the DEP electrode takes up approximately 15% of the total surface area. The patterned electrode design is optimized to excite the 8th order (Leissa's notation: 19) of the roof tile-shaped eigenmode. Additionally, the design of the DEP actuator was revised to maximize inhomogeneities in the electric field and thus the DEP force.

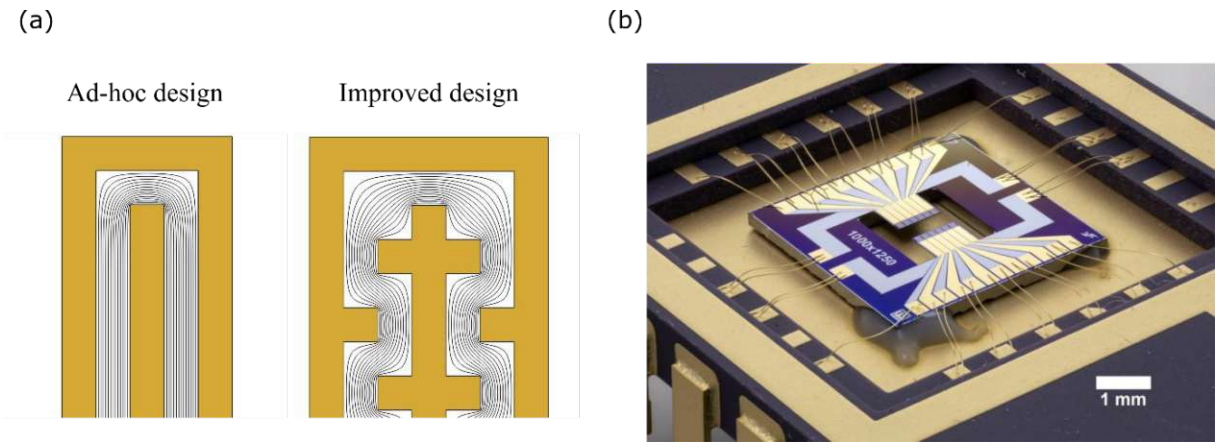

Figure 4-17: (a): Qualitative comparison of two electrode designs to accumulate particles. The ad-hoc electrode design on the left shows an almost uniform field distribution (black lines represent isopotentials) between the electrodes (coloured areas). The improved design enhances the local field inhomogeneities, thus maximizing the force on the particles. (b) Optical micrograph of the sensor chip, glued in a 24-pin dual-inline package. The electrodes are connected to the pins via wire bonding.

4.3.4 Detection of varnish particles in lubricating oils

4.3.4.1 Preparation and analysis of the oil samples

In this section, the proof of principle is demonstrated for the developed sensor by monitoring the sensor characteristics in deteriorated lubricating oil. For this purpose, commercially available turbine oil was artificially aged using the method described in section 2.5.5. Four samples were prepared, which differ in the duration of artificial aging: 12 hours (*12H*), 24 hours (*24H*), 48 hours (*48H*) and 96 hours (*96H*). The resulting oil samples were analyzed for changes in viscosity, acidity (expressed by the neutralization number) and infrared absorption to determine the effects of thermal-oxidative oil degradation due to the aging process (Table 4-3). In comparison to the untreated fresh oil used as a reference, all four samples showed a slight increase in kinematic viscosity at 40°C and 100°C measured by the SVM 3000 Stabinger viscometer (Anton Paar GmbH, Graz, Austria) according to ASTM D7042. These changes in viscosity can be attributed to oxidation reactions resulting in degraded oil constituents. Regarding the neutralization number, the measured changes are too low for a reliable assessment of the lubricant condition based on oil acidity. However, studies showed that the significance of the latter two parameters is limited for evaluating the oil condition regarding the formation of varnish particles. This is especially true for group II and group III base oils, where the limited solubility of contaminants leads to precipitation of particles before a significant change in acidity or viscosity is detected [48] [162]. In order to quantify the thermo-oxidative oil degradation, the infrared spectrum of the aged samples was obtained with FTIR [60]. For this purpose, the IR absorption of the aged oil samples was compared with that of a fresh sample at a wavenumber of 1710 cm^{-1} (carbonyl band) and good correlation to the duration of the temperature treatment was found. Figure 4-18 shows the measured FTIR spectra of the aged oil samples along with the fresh, untreated oil, where the calculated absorbance values at 1710 cm^{-1} gradually increase up to a value of 1 A/cm. This indicates an increasing level of oxidation and hence varnish potential for the four oil samples with increasing aging time.

Table 4-3: Analysis of the oil samples to determine the thermal-oxidative deterioration due to the temperature treatment in comparison to fresh oil.

Oil sample	Kinematic viscosity (40°C) [mm²/s]	Kinematic viscosity (100°C) [mm²/s]	Neutralization number [mg KOH/g]	FTIR absorbance at 1710 cm^{-1} [A/cm]
Fresh oil	44.035	7.073	0.083	-
12H	44.495	7.150	0.039	0.3
24H	44.863	7.179	0.050	0.4
48H	45.426	7.242	0.037	0.5
96H	46.201	7.319	0.036	1.0

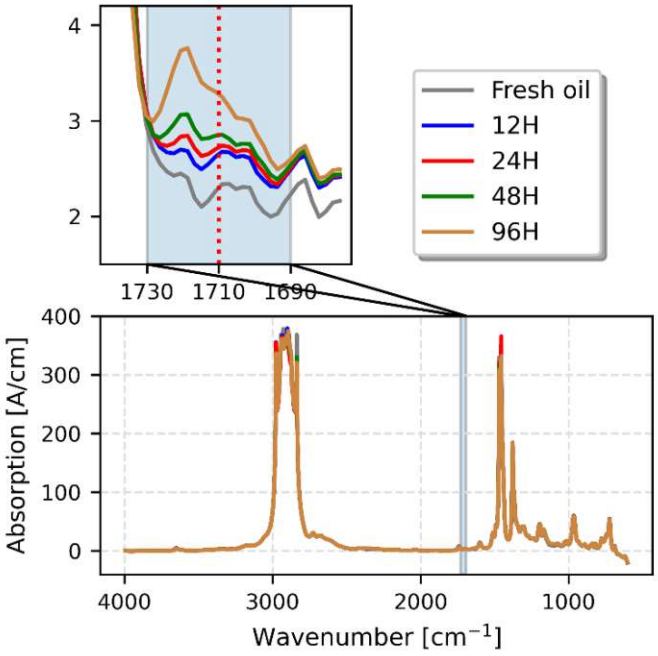

Figure 4-18: FTIR spectra of the aged oil samples and fresh oil. The adsorption in the carbonyl band (1710 cm^{-1}) increases with a longer duration of the temperature treatment, indication rising oxidation levels of the oil constituents.

4.3.4.2 Experimental setup and measurement procedure

The experimental setup to evaluate the sensor performance is depicted in Figure 4-19. The MEMS sensors were fully immersed in the previously aged oil samples and placed in a temperature-controlled climate chamber. The oil was heated to a temperature of 90°C to simulate typical operating conditions inside lubricated machinery. It must be noted that at this temperature, no further relevant oil aging is expected during the experiment duration of 24 hours.

As described above, the sensor chip consists of two identical microcantilevers, connected to the same substrate. This offers the possibility to apply a differential measurement scheme as described in section 4.2.3. The DEP electrodes of one cantilever on the sensor chip were biased with a DC-voltage of 15 V to accumulate the varnish particles. Therefore, this component is labeled as *active* cantilever. The other

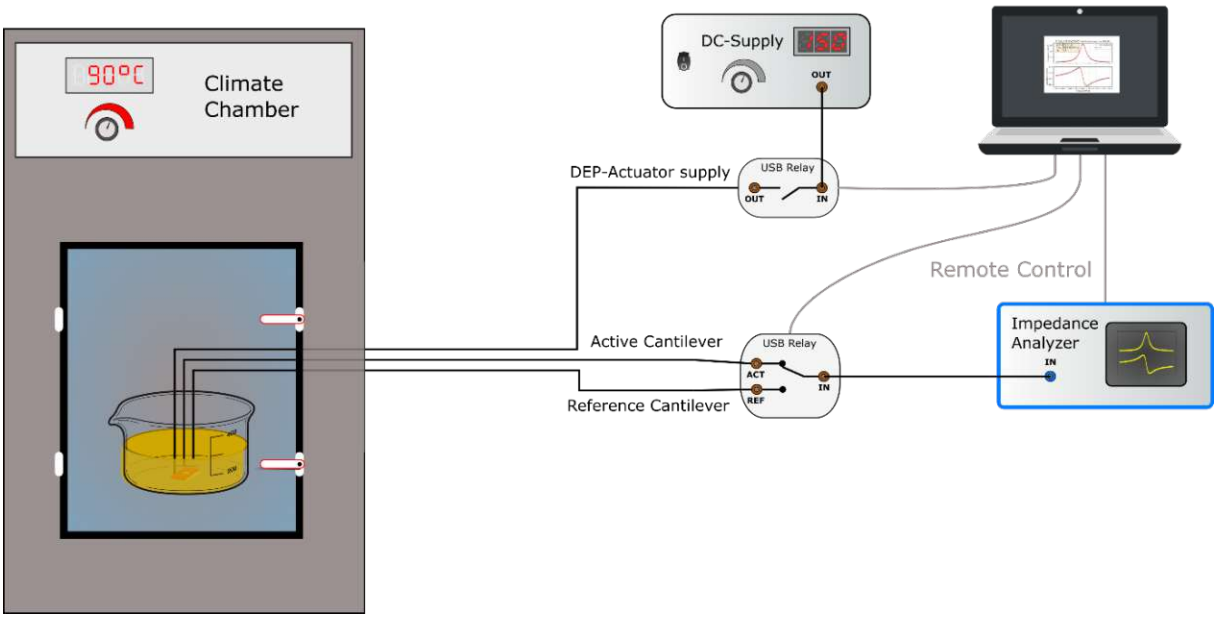

Figure 4-19: Setup for evaluating the MEMS sensor performance: The sensor is immersed in a beaker containing lubricating oil and is placed in a climate-controlled chamber. USB-controlled relays are used to connect the cantilevers to the impedance analyser and DC-actuator supply. A laptop is used to control the relays and store the admittance data measured by the impedance analyser.

cantilever served as a *reference* because its DEP actuator was not connected to the voltage source and hence does not actively accumulate particles on the surface. Because the oil viscosity is highly dependent on temperature, even a small change of the ambient conditions has an impact on the resonance frequency f_{act} of the actively particle-accumulating microcantilever, giving rise to misinterpretations. This parasitic effect is canceled out by monitoring the resonance frequency f_{ref} of the reference cantilever. Because the DEP electrodes are not voltage loaded, the resonance frequency of the reference cantilever is predominantly influenced by temperature-related changes of the oil viscosity and density. To account for this effect, the measured resonance frequency shift of the reference cantilever Δf_{ref} is subtracted from the resonance frequency shift Δf_{act} of the active cantilever. This differential measurement scheme allows for the determination of Δf, which is solely a result of the accumulation of particles

$$\Delta f = \Delta f_{act} - \Delta f_{ref} \,. \tag{4.28}$$

A USB-controlled relay was used to subsequently connect the piezoelectric stack of the active and reference cantilever to an impedance analyzer during measurement. The frequency-dependent admittance of the piezoelectric layer was then used to determine the mechanical resonance frequency and Q factor, as described in section 2.2.3. Despite using DC-voltage for the DEP actuator supply, it interfered with the measurement, rendering the determination of the layer impedance difficult. Therefore, a second USB-relay was used to disconnect the DEP actuator from the DC-voltage source during the measurement. However, due to the strong adhesion forces, no detachment of varnish particles was observed during the measurement cycle. In fact, the particles can hardly be removed from the sensor

surface, even when using strong solvents, such as toluene. Using this technique, the resonance frequency of both the active and reference cantilever can be determined with a standard deviation of 45 Hz. The sensors were exposed to the oil samples for a total duration of 24 hours, while the admittance spectra of both the active and the reference cantilever were recorded in 15 min intervals.

4.3.4.3 Results and proof of principle

Using the measuring procedure described above, the sensor response to the four oil samples with different degrees of degradation was determined. For each experiment a fresh, "as fabricated" sensor was used to achieve the high comparability between the measurements. Figure 4-20a shows the resonance frequency characteristics of both the active and reference cantilevers for all four oil samples as a function of the measurement time. Note that due to minor fabrication tolerances, the resonance frequencies of the individual microcantilevers are not identical at the beginning of the experiment but deviate by a few Hz. However, this has no impact on the sensing characteristics, as the sensor principle is based on measuring the resonance frequency shift rather than the absolute value of the resonance frequency. The total resonance frequency shift of the active particle-accumulating microcantilevers (colored symbols) showed a strong correlation to the duration of the aging procedure prior to the sensor evaluation. For easier comparison, this is visualized in Figure 4-20b by plotting the relative resonance frequency shift of the microcantilevers related to their corresponding initial value at the beginning of the experiment, thus clearly demonstrating that the total shift in resonance frequency is dependent on the condition of the lubricating oil. On the other hand, the resonance frequency of the reference microcantilevers seems to be unaffected by the lubcricant condition and shows a constant drift toward lower values up to approximately 590 Hz (260 ppm) during the measurement duration of 24 hours. This drift is attributed to randomly adsorbed particles on the sensor surface, thus it is reasonable to assume that this effect influences both the active and the reference cantilever equally. Therefore, the resonant frequency of the reference sensor can be used as a stable baseline to detect changes of the oil properties due to external influences, such as viscosity changes caused by temperature variations. Finally, equation 4.28 is used to calculate the resonance frequency shift that is solely induced by the active accumulation of varnish particles using DEP, as depicted in Figure 4-20c. After 24 hours, a total resonance frequency shift of to -707 Hz, -1259 Hz, -3842 Hz and -7283 Hz was measured for the four oil samples *12H*, *24H*, *48H* and *96H*, respectively. Since the repeatability is important for practical use of the sensor, the measurement of the *96H* sample was conducted simultaneously with two independent sensors. Figure 4-20d shows very good agreement of both measurements, with an average deviation of the measured resonance frequency shift of about 5%.

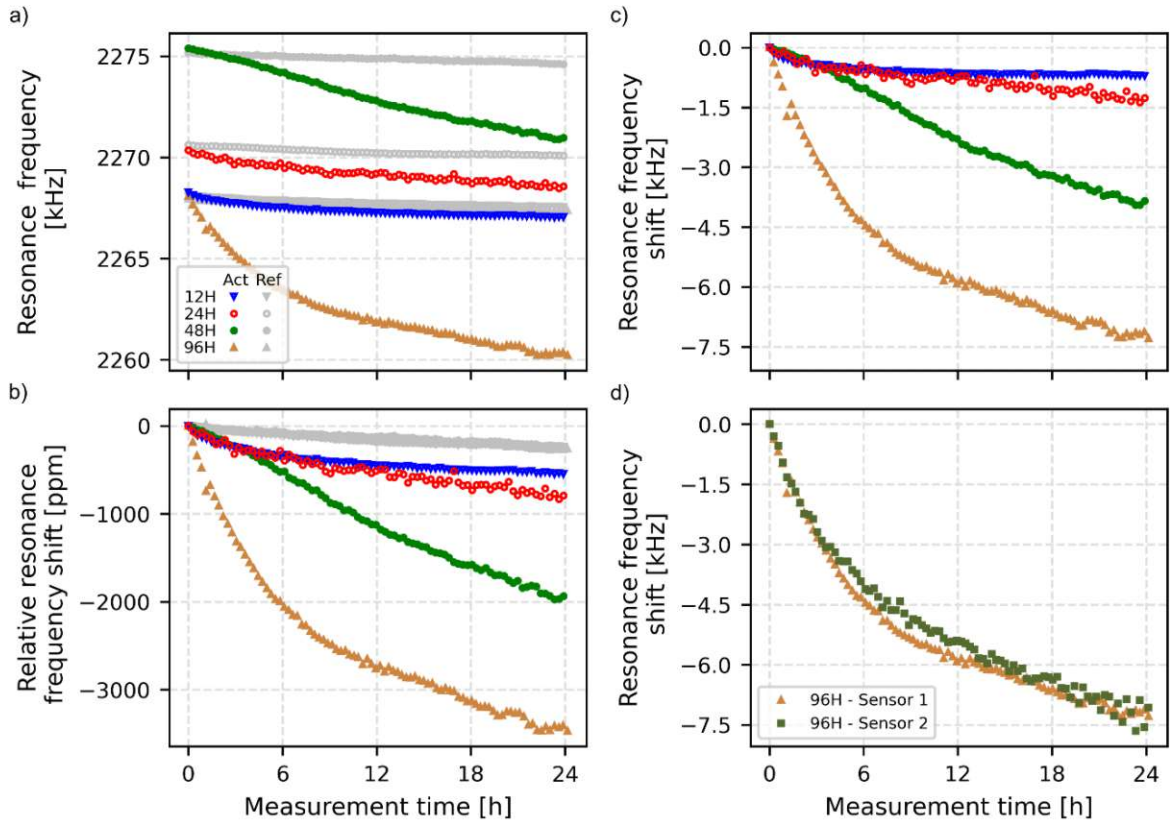

Figure 4-20: Response of the microcantilever sensor to four differently aged oil samples measured at an oil temperature of 90 °C: (a) Resonance frequency for the active (colored) and reference (grey) cantilevers. (b) Relative resonance frequency shift, whereas the initial value at the start of the measurement cycle serves as base value. (c) Total resonance frequency shift induced by the accumulation of particles on the sensor surface. (d) Comparison of two independent measurements of the 96H oil sample using two different sensor elements.

In addition to the resonance frequency, the measured impedance spectra were used to determine the Q factor for all measurement points, as depicted in Figure 4-21. As already observed for the resonance frequency, variations during fabrication lead to slightly different values of the Q factor at the beginning of the experiments, ranging from approximately 100 to 120. In agreement with the resonance frequency characteristics, the Q factor of the reference elements did not show a significant change over time. In contrast, the active cantilevers showed a Q factor response depending on the aging duration of the oil. While the Q factors of the *12H* and *24H* sample only slightly decreased by approximately 5%, the *48H* sample showed a decrease of about 15%. A drop of approximately 38% was measured for the *96H* sample, which is attributed to the strong accumulation of particles on the sensor surface, as a considerable energy fraction needed to deform the particle layer is lost during each oscillation cycle, thus leading to a significant reduction of the Q factor. This effect is more pronounced for thick particle layers, *i.e.,* higher particle concentrations when the oil is aged longer. In addition to the resonance frequency shift, the change of the Q factor can therefore serve as a second parameter to evaluate the particle contamination of the fluid.

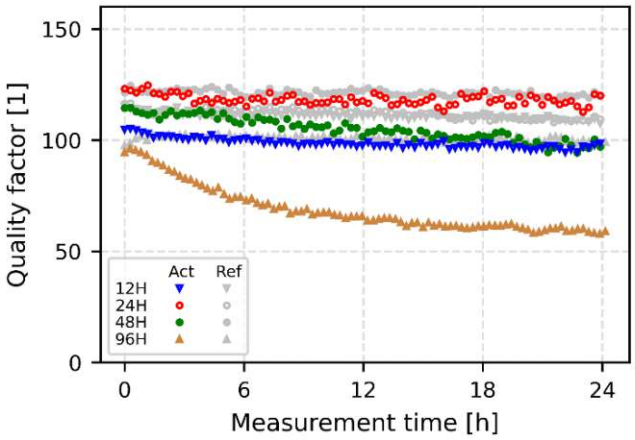

Figure 4-21: Quality factor of the active (colored) and reference (grey) microcantilevers at an oil temperature of 90°C for all four oil samples during the measurement for 24 h.

To verify the successful accumulation of particles, the microcantilever surfaces were examined after the experiments. The MEMS sensors were thoroughly rinsed with n-heptane to remove the residual oil without affecting the particles on the surface. First, the surfaces of the microcantilevers were examined using an optical light microscope, as depicted in Figure 4-22. A clear correlation between the degree of particle loading and the measured resonance frequency shift is found. This can be seen for example in the detailed view of the DEP electrodes of the sensors that were exposed to the *12H* and *96H* oil sample. Note that the accumulation predominantly takes place in regions of high electric field gradients, as expected by equation 4.27. In contrast, the reference elements are only sparsely covered by randomly distributed particles. To characterize the morphology and chemical composition of the accumulated particles in detail and compare them to the results found in section 4.3.2, the sensor surface was examined with a SEM-EDX (JEOL JSM-IT500). Figure 4-23 shows a SEM micrograph of the DEP actuator of the sensor that was immersed in the *96H* sample. The particles tend to arrange themselves in chains during accumulation, an effect that is often observed in dielectrophoresis. The investigation of the chemical composition of the accumulated particles using EDX (20 kV acceleration voltage), as shown in Table 4-4, showed the presence of the same elements as measured in section 4.3.2. These results prove the successful accumulation and detection of oxidation-related varnish particles using oscillating microcantilevers with an integrated DEP electrode structure.

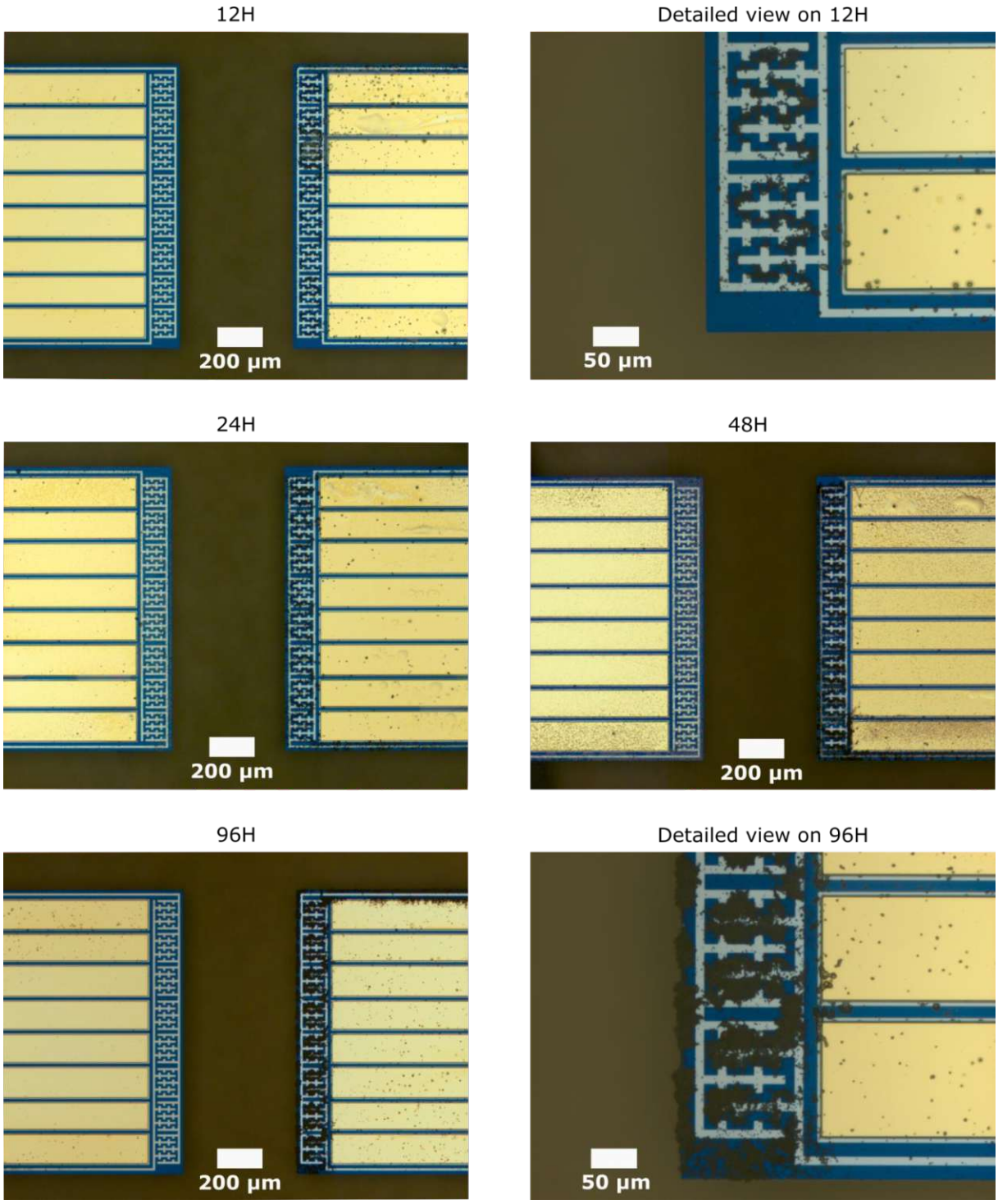

Figure 4-22: Optical micrographs of the active (right) and reference (left) microcantilever surfaces after the measurement cycles in the four oil samples and a detailed view of the DEP electrodes of the 12H and 96H sensors. The DEP electrodes of the active cantilevers are covered with particles, while the reference cantilever is only sparsely covered by randomly distributed particles.

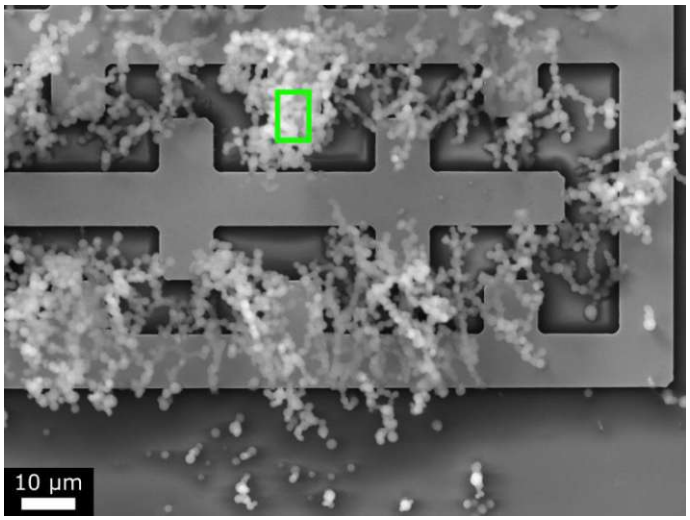

Figure 4-23: SEM micrograph of the accumulated particles. The chemical composition of the particles inside the green rectangle was studied by EDX and is given in Table 4-4.

Table 4-4: EDX results for the particles in the highlighted area in Figure 4-23

Element	At %
C	79.7
O	6.0
Al	0.1
Si	10.3
P	2.1
S	0.7
Ti	0.03
Sn	0.1
Au	0.9

Based on the measured resonance frequency shift Δf, the accumulated particle Δm mass can be estimated. For the ferrous particle sensor in section 4.2, equation 3.1 was integrated over the entire coil area when deriving the particle mass, since the accumulation was almost homogeneous there. However, the examination of the sensor surface of the varnish sensors (Figure 4-22) showed that the accumulation is not homogeneous and therefore integration must only be executed for areas where accumulation was observed. For this, equation 3.1 is rearranged for Δm and integrated only over the area $A_{acc}$where the accumulation of particles is observed:

$$\Delta m = -2\frac{\Delta f}{f_{res}} M \left(\frac{1}{A_{acc}} \int_{A_{acc}} P(x,y)\phi^2(x,y)dA \right)^{-1} \qquad 4.29$$

using

$$P(x,y) = \begin{cases} 1, & \text{if a particle was accumulated at (x,y)} \\ 0, & \text{otherwise} \end{cases}.$$

For the evaluation of equation 4.29 it would therefore be a tedious task to manually determine the particle covered areas of the surface. Therefore, the detection of particles was automatized by applying a machine learning algorithm with a random forest regressor [212]. This algorithm uses manually classified training data to create a set ("forest") of decision trees. The algorithm is therefore trained to detect certain features in a dataset and classify them accordingly. The automated determination of the particle positions was implemented in Python, using the Scikit-learn[9] library. The training data consists of a small subset (312x184 µm or 212x125 px.) of the cantilever surface in which the areas with particles have been manually selected. After the initial training phase, the algorithm is now able to automatically detect the position (x, y) of all particles on the cantilever surface. The positions were used to calculate the values of the mode shape function $\phi(x, y)$, which was integrated over the area of particle accumulation (cf. equation 4.29). For an in-depth explanation and other examples of application, the reader is referred to literature [213] [214] [215] [216]. By comparing the automated detection to manually classified fractions of the images for false-positive and false-negative classified pixels, a total error rate of approximately 5% is found. As these wrongly classified pixels are scattered across the surface and are not concentrated to regions of high vibrational amplitude, their contribution to the integral in equation 4.29 is negligible. The accumulation predominately takes place on the DEP electrodes, so that the analysis as described above is restricted to these areas. Note, that in this first-order approximation, any variations of, *e.g.,* the thickness or the mechanical properties of the accumulated particle layer are not considered.

Before applying equation 4.29, the total oscillating mass M, consisting of the cantilever mass m_{cl} and the effective mass m_{fl} of the displaced fluid during oscillation, must be deduced. This is done by correlating the cantilever vacuum resonance frequency $f_0 = 3.508\ MHz$ to the resonance frequency of the submerged cantilever $f_{res} = 2.271\ MHz$,

$$\left(\frac{f_{ref}}{f_0}\right)^2 = \underbrace{\frac{m_{cl}}{m_{cl} + m_{fl}}}_{\hat{M}}\left(1 - \frac{1}{2Q^2}\right) \qquad 4.30$$

resulting in a total oscillating mass of approximately 173 µg. Due to the low viscous losses (Q ≈ 100), the last term in equation 4.30, representing the influence of the dissipative energy losses on the resonance frequency, can be neglected.

The calculated mass of the accumulated particles for all four oil samples is given in the first column of Table 4-5. A total mass of 531 ng was found for the *96H* oil sample, which is substantially lower than the mass of the sensor, a necessary requirement for the applicability of the linear relationship between the accumulated mass and measured resonance frequency shift, as given in equation 4.29. The calculated mass values can be used to determine the mass responsivity $\mathcal{R}$ = -Δf/Δm of the sensor for each

[9]https://scikit-learn.org/

experiment, as given in the last column in Table 4-5. Because the position of the accumulated particles only varied slightly between the experiments, the corresponding mass responsivity values are comparable for all sensor elements exposed to the four oil samples. For comparison, the theoretical mass responsivity in the case of homogenous accumulation, *i.e.,* integration over the whole area of the DEP actuator in equation 4.29, is given in the last row of Table 4-5. This value is very close to the actual measured mass responsivity values, what can be explained by the distribution of the particles: the mass responsivity for a homogeneously distributed particle layer can be understood as the mean value for the corresponding cantilever surface area. A deeper study of the particle positions revealed that the particles accumulated locally in regions with a mass responsivity close to this mean value, hence the observed mass responsivity only differs slightly from that of a cantilever with evenly coated DEP electrodes. This finding has important implications for the application of the sensor in an industrial environment. Since the position of the particles for an exact calculation of the accumulated mass cannot be determined during operation, it is therefore a reasonably good approximation to assume a homogenous accumulation of particles when applying equation 4.29. Using this mean mass responsivity value, the accumulated particle mass at every measurement point during the measurement cycle was calculated and is depicted in Figure 4-24.

Table 4-5: Accumulated mass and calculated mass responsivity for the sensor elements exposed to the four oil samples. The last row shows the theoretical mass responsivity for homogeneously distributed particles on the whole DEP electrode.

Sample	Accumulated mass [ng]	Mass responsivity Hz/ng
12H	49	14.4
24H	99	12.7
48H	298	12.9
96H	531	13.7
Homogeneous particle distribution on DEP electrode	-	13.0

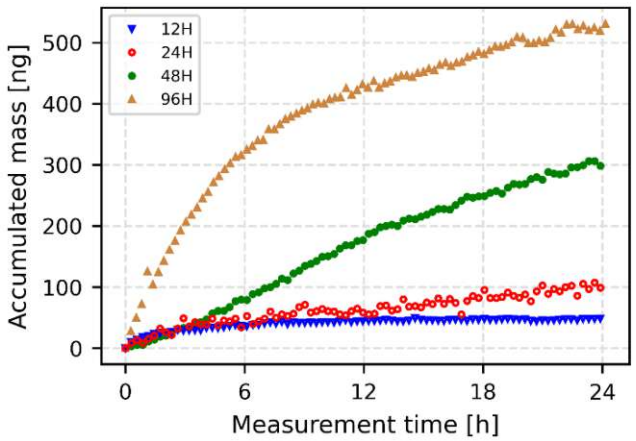

Figure 4-24: Accumulated particle mass on the sensor elements during the measurement cycles for all four oil samples, as obtained by equation 4.29.

4.3.5 Discussion

4.3.5.1 Correlation with lubricant condition

The results in the previous section show that the novel sensor is capable of detecting thermal-oxidatively formed varnish particles in lubricating oils. In this section, these results are correlated with the lubricant condition and the new sensor principle is compared with existing methods used to determine the lubricant quality regarding oxidative degradation.

Conventional testing methods to determine the lubricant quality are based on measuring characteristic oil parameters such as the viscosity and acidity of the oil. Using for example MEMS cantilevers or microacoustic devices to determine the viscosity of a liquid is an established technique nowadays [6] [7] [5] [217]. However, because of the complex composition of lubricating oils and the mostly only minor change in viscosity due to oil degradation, the measurement of solely this parameter to monitor the lubricant condition is not sufficient [198]. Additionally, other factors such as fuel dilution and temperature variations can have a major influence, making it difficult to reliably assess the oil's varnish potential solely based on viscosity [9]. Additionally, the low solvency of the commonly used group II and group III base oils leads to early precipitation of degradation products before a significant change in the oil viscosity is detected. Besides classical methods like oil titration, oil acidity can be determined by means of resonant sensors, such as, *e.g.*, a quartz crystal microbalance (QCM). By covering the surface of the QCM with a chemical-sensitive layer, acidic species in the oil are adsorbed and lead to change in the device's resonance frequency. Studies showed a strong correlation between the resonance frequency of such modified QCMs and the oil's neutralization number [57] [59]. However, another study implies that the neutralization number cannot be used as a direct indicator of the lubricating oil's varnish potential [50]. Oil oxidation testing methods used in the industry, such as RPVOT, measures the oxidation stability of the turbine oils but gives no insight on the actual deposit formation tendency of the oil [50] [204].

The comparison to conventional testing procedures such as viscosity, neutralization number and FTIR analysis shows the advantage of the proposed microcantilever sensor. Due to the measurement principle, the direct detection of the varnish particles is possible, rather than monitoring changes of oil parameters that indicate the formation of particles. As described above, the changes in viscosity and neutralization number of the oil are too low to reliably indicate the formation of varnish particles. The FTIR measurements show a gradual increase of the absorbance in the carbonyl band around 1710 cm^{-1}. The novel developed MEMS sensor showed a distinctive response to the *48H* sample (0.5 A/cm) with respect to the *24H* sample (0.4 A/cm). Although the FTIR measurements indicate only a minor increase of the carboxylic groups, the microcantilever sensor response shows the formation of a large number of particles. It can be concluded that the detection method of the novel MEMS sensor offers considerable advantages compared to conventional "indirect" oil analysis techniques, as the particles are detected directly via their mass. The measurement result is therefore independent of variations in temperature

and viscosity, as well as no knowledge of the oil chemistry is necessary for interpretation. Even though only the proof of principle was shown in this work, the developed sensor has potential for utilization in an industrial environment. This is demonstrated in chapter 5 with two test rigs in which the sensors are used for monitoring the formation of varnish particles under conditions found in the lubrication system of industrial machinery.

4.3.5.2 Detection limit and sensor performance

The limit of detection (LOD) is the lowest detectable mass change, which is an important figure of merit for resonant mass sensors. It is determined by the ratio of smallest detectable change of the cantilever-related resonance frequency and the mass responsivity of the sensor. As described in the previous sections, the mass responsivity on the cantilever surface is strongly position-dependent. For an estimation of the LOD, the results in the last section showed that it is valid to assume an effective mass responsivity for homogenously distributed particles on the surface ($\mathcal{R}_H$ = 13 Hz/ng):

$$LOD = \frac{\Delta f_{min}}{\mathcal{R}_H} \tag{4.31}$$

With a standard deviation of approximately 45 Hz when determining the resonance frequency using the piezoelectric read-out, the resulting LOD is approximately 3.5 ng.

4.3.5.3 Possible sensor improvements

An essential improvement was already implemented during the development of the final sensor design. By eliminating any overlap between the DEP actuator and the piezoelectric stack, the previously occurring short circuits and low-resistance paths were avoided, which made a solely piezoelectric readout of the vibration state possible. Nevertheless, the DEP actuator had to be disconnected from the power supply temporarily before each measurement, since the electric field interferes with the charges created in the piezoelectric thin film. A possible solution is to increase the spatial distance between these two elements, for example by further shrinking the piezoelectric stack. The resulting reduction of the piezoelectric signal can be compensated by using materials with higher piezoelectric constants, *e.g.,* by doping the AlN with transition metals such as scandium and yttrium. Furthermore, the use of a grounded metallic shielding around the piezoelectric stack can be considered in order to minimize the influence of the electric field of the DEP actuators.

Furthermore, the measurement of the *96H* sample showed a significant reduction of the Q factor as a result of the accumulated particles (Figure 4-21). The accuracy of the determination of the resonance frequency can therefore be reduced if the oil is heavily contaminated with particles. A possible solution is to reverse the function of the active and reference cantilever at a defined Q factor threshold. As a result, particles are now accumulated at the former reference cantilever and the former active cantilever serves as a reference. This prevents the Q factor from dropping to a point where it becomes impossible to determine the resonance frequency.

4.4 Summary

In this chapter, two novel MEMS sensors were presented that are capable of detecting typical particle species found in lubricating oils. Both sensors are based on tailored actuators on the cantilever surface that promote the accumulation of particles via magnetophoretic and dielectrophoretic forces, respectively. The active accumulation of the particles on the sensor surface is necessary because the particle-related changes in the measurable fluid properties, such as viscosity and density, are negligible due to the low concentrations. Furthermore, it can be ensured that the respective particle type is selectively detected. The use of a differential measurement method with a passive reference cantilever has proven useful to compensate for other influences on the resonance frequency, such as temperature variations or impurities in the oil.

Both sensors were tested in liquids with a high particle load and showed consistent performance over several hours. It can therefore be assumed that the principle of active accumulation is suitable for long-term measurements of oil quality regarding particle contamination. The measured shifts of the resonance frequency can be measured reproducibly with standard laboratory equipment, whereby the limit of detection is between 3.5 - 4 ng. This allows to detect increasing particle contamination of the oil in an early stage. This is particularly important for predictive maintenance, as discussed in section 1.1.

The design of the sensors served to provide a proof of principle in a laboratory setting and certainly still has to go through several iterations before the sensors can be used commercially. Thus, some possible sensor improvements have already been addressed in this section. Nevertheless, the sensors have impressively demonstrated the possibilities of MEMS cantilevers for measuring oil quality. The next chapter goes a step further into the industrial application, where the sensors are installed in test rigs that simulate real-world conditions in the oil circuit of industrial machines and hence, the aging process.

5 Monitoring of oxidative lubricant degradation in industrial-type test rig setups

The previous chapter showed that the sensor developed in this thesis can be used to detect oxidation-related varnish particles in lubricating oils. However, for these experiments the oil was artificially aged prior to the characterization of the sensors in order to produce oil samples in different states of degradation. This approach is well suited to demonstrate the sensor functionality but does not reflect the real conditions found in lubricated machinery. Under real operating conditions the oil undergoes a continuous aging process, leading to a gradually increasing particle contamination. Additionally, the oil is in constant motion, hence the sensor experiences a steady stream of particle-contaminated oil. To investigate the sensor performance under these more application-oriented conditions, two test rigs were developed, which simulate the conditions found in the oil circuit of a lubricated machinery. The sensor was integrated in these test rigs and two potential modes of operation were evaluated, both of which are presented in the following sections.

5.1 Intermittent varnish monitoring

5.1.1 Description of the measurement procedure

The first possible operating mode of the sensor is called "intermittent" measurement. The sensor is integrated in the oil circuit to solely accumulate varnish particles while the vibration characteristics of the sensor are not monitored in real-time. After a defined period of time, the sensor is removed and the accumulated particle mass is determined in a separate measurement of the resonance characteristics, while a new sensor is installed in the oil circuit for further monitoring the varnish particle contamination. The measurement procedure is depicted in Figure 5-1 and described in detail below.

Prior to the integration in the test rig, the resonance frequency for both microcantilevers on the sensor chip is determined in air using an impedance analyser. This value serves as a baseline of the fresh sensor to which the resonance frequency shift is related after the experiment. After this initial characterization, the first sensor is integrated into the oil circuit of the test rig. However, only the DEP actuator of one microcantilever (“*active* cantilever”) is supplied with a voltage to accumulate particles, while the second microcantilever serves as a reference without being connected to the power supply. Note that in this mode of operation, the cantilevers are not excited to oscillate during the accumulation of varnish

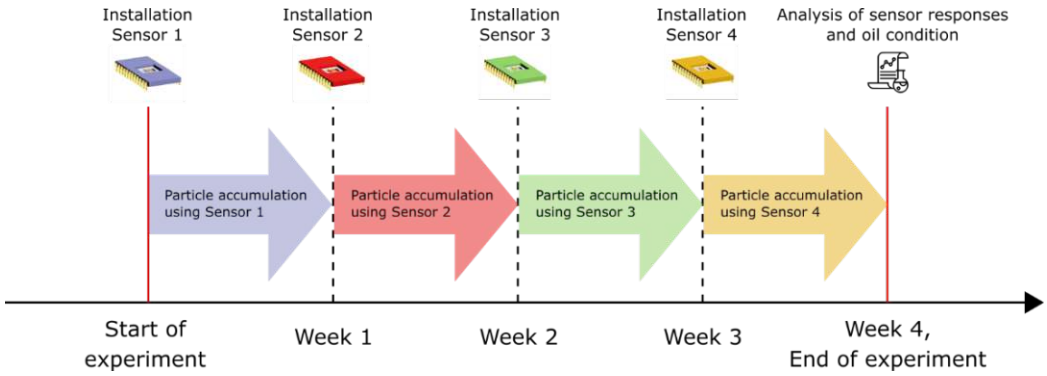

Figure 5-1: Visualization of the intermittent operating mode. At the start of the experiment Sensor 1 is integrated into the oil circuit of the test rig, where it accumulates varnish particles for 7 days. After this period, the sensor is removed, and replaced by a new sensor that accumulates particles again for 7 days. Additionally, an oil sample is taken before replacing the sensor. This procedure is repeated three times up to a total measurement time of 4 weeks. After the experiment, both the resonance characteristics of the sensors and the oil condition are analyzed and compared among each other.

particles, as the characterization of the resonance characteristics is carried out after the experiment. After a fixed period of 7 days the sensor is removed from the oil circuit and the new sensor is installed, which again accumulates particles for 7 days. Additionally, an oil sample is taken to determine the current oil condition. This procedure is repeated three times up to a total experimental time of 4 weeks.

After the experiment, the sensors are thoroughly rinsed with n-heptane to remove residual oil from the sensor surface while leaving the accumulated varnish particles unaffected. The resonance characteristics of the sensors are again determined in air using an impedance analyser. While the resonance frequency of the actively accumulating microcantilever shifts due to the accumulated varnish particles, the resonance frequency of the reference element is only affected by randomly adsorbed particles and residual oil. To account for variations of ambient conditions (such as temperature) during the determination of the resonance characteristics, the measured resonance frequency shift of the reference cantilever is subtracted from the measured shift of the active cantilever, in the same way as done in sections 4.2 and 4.3. Figure 5-2 shows a typical measurement taken before and after the accumulation period in the test rig. The sensor is optimized to excite the 19-mode and show a resonance frequency of approx. 3.55 MHz and a Q factor of approx. 1700 prior to the measurement. After the 7-day particle accumulation period, the resonance frequency of the active cantilever decreased by approx. 92 kHz, while the resonance frequency of the reference cantilever only decreased by 12 kHz. The Q factor of the active cantilever dropped down to approx. 525, while the Q factor of the reference cantilever remains relatively stable at approx. 1400.

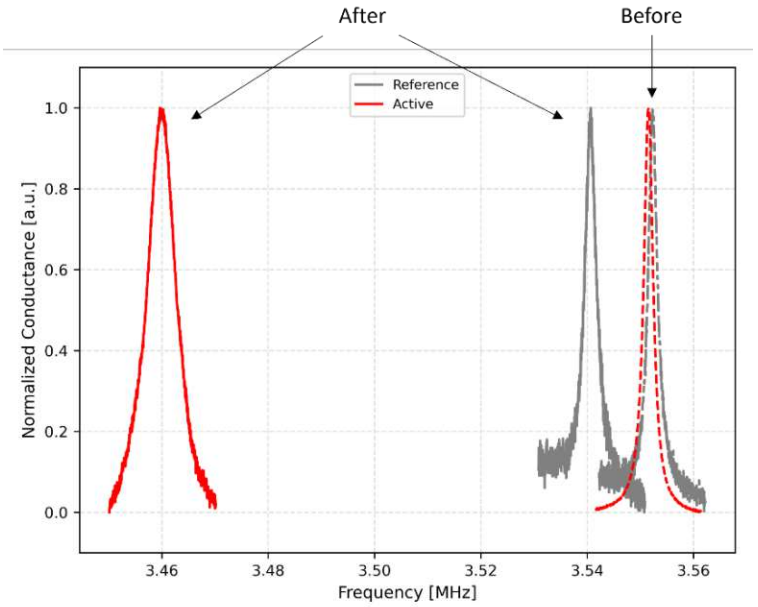

Figure 5-2: Conductance spectra of the active and reference cantilever before and after accumulating particles in the test rig for 7 days. As expected, the resonance frequency shift of the active cantilever is much more pronounced than for the reference due to the active accumulation of varnish particles on the sensor surface.

5.1.2 Experimental setup and sensor integration

The test rig for simulating an oil circuit is shown in Figure 5-3. In the *hot zone* an oil volume of approximately 300 ml is heated to 120°C in a glass beaker while injecting 3 litres per hour of pure oxygen to promote oxidative deterioration. Additionally, copper and iron wires serve as catalysts to accelerate oil aging. This zone simulates hotspots in the oil circuit, such as lubricated bearings and combustion chambers. The *cold zone* on the other hand corresponds to the oil sump of the lubricated machinery, where the oil is approximately at room temperature. These two zones are coupled by tubing, in which the oil is pumped in a loop by peristaltic pumps. To simulate an oil cooler in the oil circuit, the oil is cooled down to 10°C before being fed back to the cold zone. The sensor is integrated into the oil circuit using a special cover for the DIP package that was fabricated by 3D printing using polylactide (PLA). This cover directs the oil flow across the sensor chip and is equipped with sockets on both ends for the inlet and outlet tubes. A transparent window allows the sensor to be inspected by eye during the measurement cycles and ensures bubble-free filling of the cover. After the cover was pressed to the DIP package by applying rubber bands, a PCB board was used for electrical connection and to supply the DEP actuator of the active cantilever with a constant voltage of 15 V.

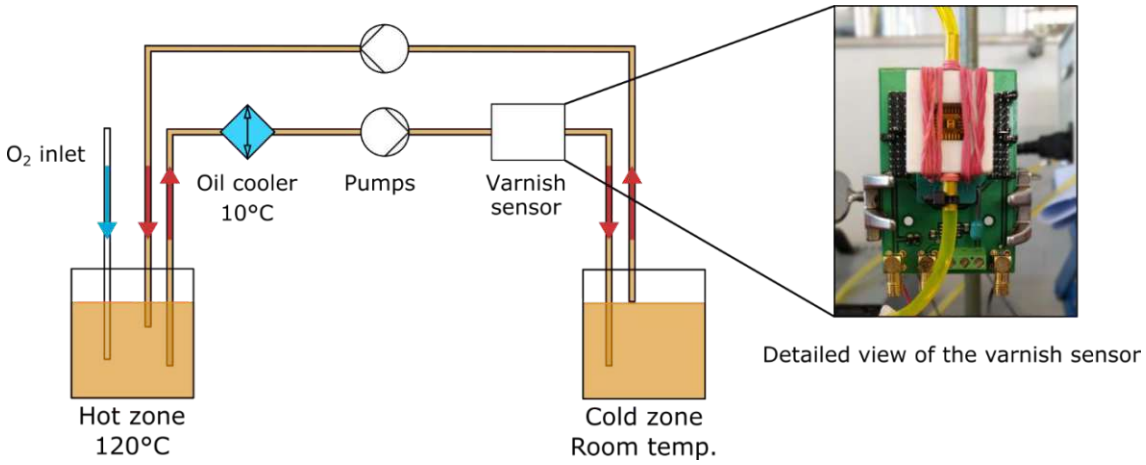

Figure 5-3: Schematic of the test rig to mimic the oil circuit of a lubricated machine (left): The hot zone simulates hot spots in the machine, such as roller bearings or combustion chambers. The cold zone represents the oil sump, where the oil is at or close to room temperature. Both zones are connected via tubing where the oil is moved in a loop using pumps. To simulate an oil cooler, the oil is cooled to 10°C after leaving the hot zone. The varnish sensor is integrated in the circuit with a 3D-printed cover for the DIP package (right).

5.1.3 Results

Using the procedure described in section 2.2.3, the frequency-dependent impedance spectrum was used to determine the resonance frequency of both the active and reference cantilever on the four sensor chips, respectively. Based on the baseline values before the experiment, the resonance frequency shift due to the accumulated particle mass was determined. The results for each week are given in the first column in Table 5.1. The magnitude of the resonant frequency shift increases with the duration of the aging process, which indicates an increasing particle contamination of the lubricating oil. As seen in section 4.2 and 4.3, the measured resonance frequency Δf shift can be used to calculate the accumulated particle mass

$$\Delta m = -2\frac{\Delta f}{f_r} m_{cl} \left(\frac{1}{A_{DEP}} \int_{A_{DEP}} \phi^2(x,y) dA \right)^{-1}. \qquad 5.1$$

Here the integral in the last term is evaluated across the surface A_{DEP} of the DEP actuator. In contrast to the previous sections, only the mass of the pure cantilever mass m_{cl} must be considered since the measurement takes place in air. The values of the accumulated mass Δm are given in the second column of Table 5.1. Note that each of these values represents the accumulated particle mass during a 7-day period and is not the cumulative sum of masses originating from previous weeks. The accumulated particle mass increases by 25%-40% each week, up to a maximum value of 1.63 µg, indicating progressive deterioration of the lubricating oil. The microscopic images of the sensor surface, depicted in Figure 5-4, show an increasing deposition of varnish on the actuator element with aging duration. After the first week, only a few areas are covered with varnish. The optical micrograph of the sensor used during week 2 shows that the varnish has already covered the entire actuator surface. As expected from the measured frequency shifts, the sensors used in weeks 3 and 4 show a progressive increase in varnish coverage.

Table 5.1: Measured resonance frequency shift and respective accumulated mass for each week during the experiment using the test rig depicted in Figure 5-3.

Period	Frequency shift [kHz]	Accumulated mass [µg]
Week 1	32.98	0.66
Week 2	44.98	0.90
Week 3	62.72	1.27
Week 4	79.88	1.63

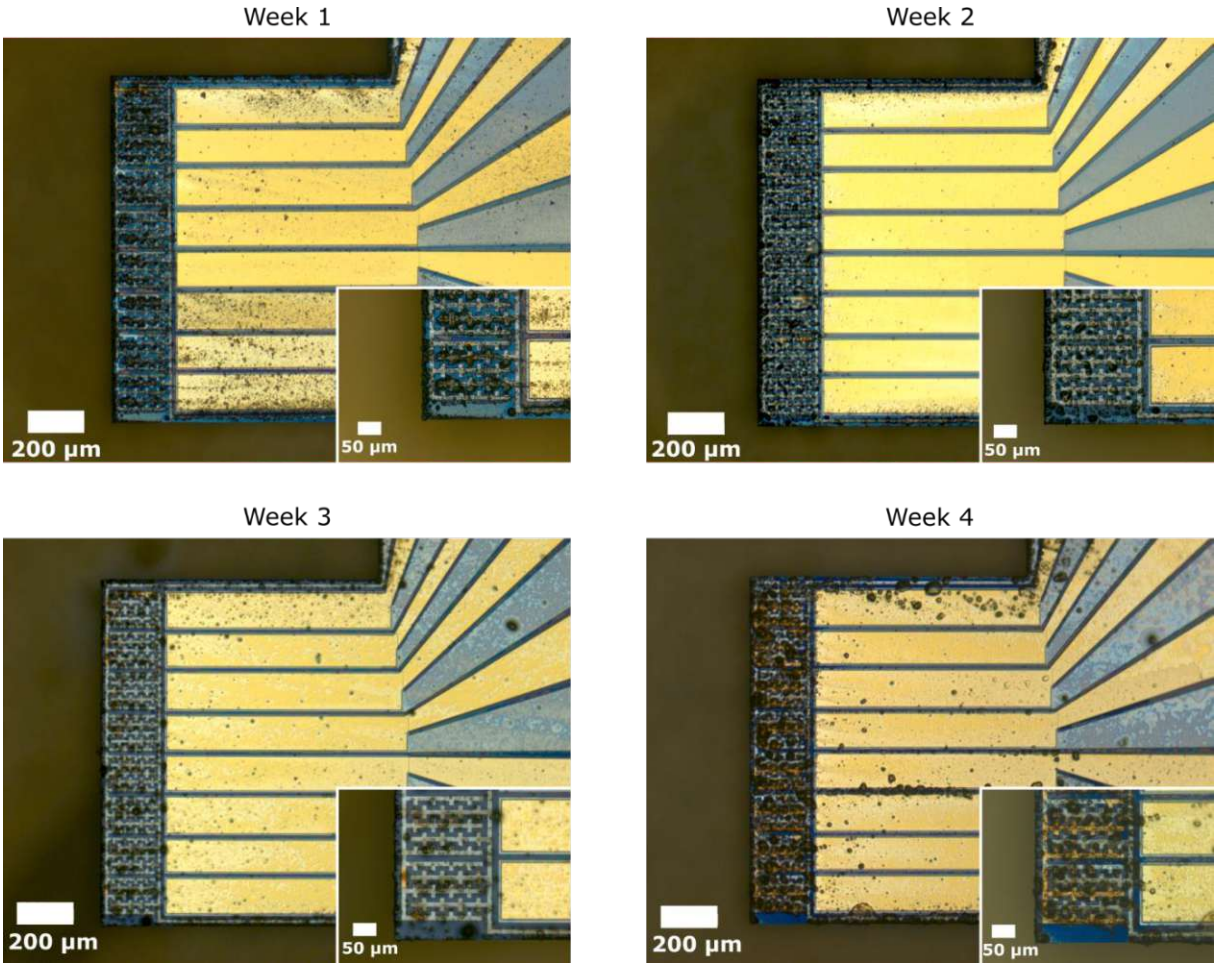

Figure 5-4: Optical micrograph of the sensor surface for each week. The insets show a detailed view of the DEP actuator. The increasing coverage of the surface is in accordance with the measured resonance frequency shift.

To correlate the results of the varnish sensor with the oil condition, oil samples were taken during the replacement of the sensors each weak and were subsequently analysed (Table 5.2). Viscosity values slightly increase with aging time, indicating the formation of high molecular weight oxidation products. In addition, the oxidation number shows a significant increase in the first week, which can be attributed to the formation of acidic constituents due to the oxidation process. As observed in the last chapter, an increase in IR absorption in the carbonyl band during oil ageing is measured, indicating a progressive oxidation of the oil components [60]. However, during the first three weeks the IR absorption varies between 0.3-0,5 A/cm and only increases after week 4 to 0.7 A/cm. This slow progression in IR absorption might be explained by the lower oil aging temperature of 120°C used in this experiment, compared to section 4.3. As explained in section 2.5.3, the oxidation typically tends to increase rate increases two-fold for every 10 K temperature increase, hence significantly slower oxidation is expected for the aging experiment in this section [48]. Additionally, gravimetric analysis was performed for two oil samples, where a significant increase of the filter residues in the fourth week compared to the second week was found, indicating the gradual build-up of insoluble varnish particles [165].

Table 5.2: Analysis of the oil samples to determine the oxidation-related degradation in comparison to the fresh oil.

Period	Kinematic viscosity (40°C) [mm^2/s]	Kinematic viscosity (100°C) [mm^2/s]	Neutralization number [mg KOH/g]	FTIR absorbance at 1710 cm^{-1} [A/cm]	Gravimetric analysis (filter residue) [mg/kg]
Fresh oil	44.035	7.0727	0.083	0	-
Week 1	44.454	7.1277	0.121	0.5	-
Week 2	44.691	7.1514	0.137	0.3	64
Week 3	44.888	7.1639	0.14	0.5	-
Week 4	44.998	7.1672	0.134	0.7	136

5.1.4 Discussion

The intermittent mode is probably the simplest operating mode of the sensor. After an initial characterization in air, the sensor is integrated into the oil circuit, where it accumulates particles for a defined time. After replacing the sensor, it is washed with n-heptane and the accumulated particle mass is determined based on the measured resonance frequency shift in air. This measurement can be carried out without much effort in a laboratory setting, thus avoiding disturbances during the measurement.

In this experiment it was shown that the particle mass accumulated in a time span of one week correlates with the oil condition. The sensor is therefore able to detect ongoing oxidation of the oil under realistic conditions. Since the measurement is performed offline, *i.e.*, the oil quality is only determined in fixed intervals, the analysis procedure is similar to conventional laboratory analysis. However, by using mass sensitive microcantilevers the presence of particles is directly detected by their influence on the sensor's resonance frequency. This contrasts with the conventional oil condition parameters such as viscosity and neutralization number that can only indicate a change in the oil chemistry that might lead to the formation of particles. Therefore, the information provided by the sensor allows conclusions on the

particle load of the oil, independent of the measurement of other oil parameters. This is in contrast to conventional laboratory methods, where the individual measurement results have to be correlated in order to make an estimate of the varnish potential.

Based on the above discussion, the intermittent sensor can be regarded as suitable for non-critical applications where testing the oil condition at fixed intervals is sufficient. Together with conventional oil analysis methods, this measurement method can help to get a more complete picture of the oil quality, especially regarding the varnish particle contamination of lubricating oil in use.

5.2 On-line lubricant condition monitoring

In the previous section, the intermittent operating mode was presented, in which the particle contamination of the oil is only determined at regular intervals. For many industrial applications, real-time monitoring of the oil condition is of particular interest, as it allows for the detection of inappropriate operating conditions and premature oil degradation without any time delay ("predictive maintenance"). In this section the real-time capability for the detection of varnish particles of the developed sensor is shown. For this purpose, a test rig was constructed, which allows for the accumulation of particles while simultaneously measuring the resonance characteristics under realistic conditions. The sensors were integrated in the oil stream and the resonance frequency was monitored for a total duration of approximately 110 hours while oil samples were taken and analysed every 12 hours using conventional laboratory methods. After the experiment, the resonance characteristics of the microcantilevers and the results of the laboratory analysis were correlated to gain insight on the sensors behaviour under these realistic aging conditions. The following section describes the experimental setup and measurement procedure to test the sensors real-time monitoring capabilities.

5.2.1 Test rig setup and measurement procedure

The test rig setup for evaluating the sensor is shown in Figure 5-5. A glass beaker is filled with approximately 1.5 litres of standard turbine oil and heated to 150°C in a temperature-controlled climate chamber. To promote oxidation of the oil constituents, pure oxygen is introduced in the oil at a flow rate of 3 litres per hour. A peristaltic pump transfers oil into an external glass beaker that holds a total volume of approximately 500 ml in which three varnish sensors are immersed. In section 4.3 it was seen that the build-up of varnish leads to a significant decrease of the measured Q factor. Since a pronounced resonance peak is necessary to measure the resonance characteristics with high precision, the oil in the beaker was heated to a constant temperature of 90°C [218]. The lower viscosity of the oil at this temperature ensured a Q factor in the range of 50-100 at a resonance frequency of approx. 2.35 MHz (19-mode) even in later stages of the experiment. Additionally, a magnetic stirrer ensures appropriate mixing of the oil and homogenous distribution of the varnish particles in the beaker. Like in previous measurements, the DEP actuators of the active cantilevers are supplied with 15 V, while the reference cantilevers are not powered to use their resonance frequency shift to correct for external influences such

as temperature fluctuations. A Python script triggers a measurement of the conductance spectra every 20 min, by subsequently connecting the piezo stacks of the microcantilevers to an impedance analyser using a switching matrix. During this measurement, a USB relay separates the DEP actuators from the voltage source to minimize crosstalk to the piezoelectric stack. Additionally, oil samples are taken every 12 hours, which are then analysed in the laboratory using conventional oil characterization methods to determine the viscosity, acidity, FTIR absorbance and filter residual weight. After the experiment, the sensors are removed from the test rig and thoroughly rinsed with n-heptane to remove any residual oil to inspect the surfaces of the cantilevers using an optical microscope.

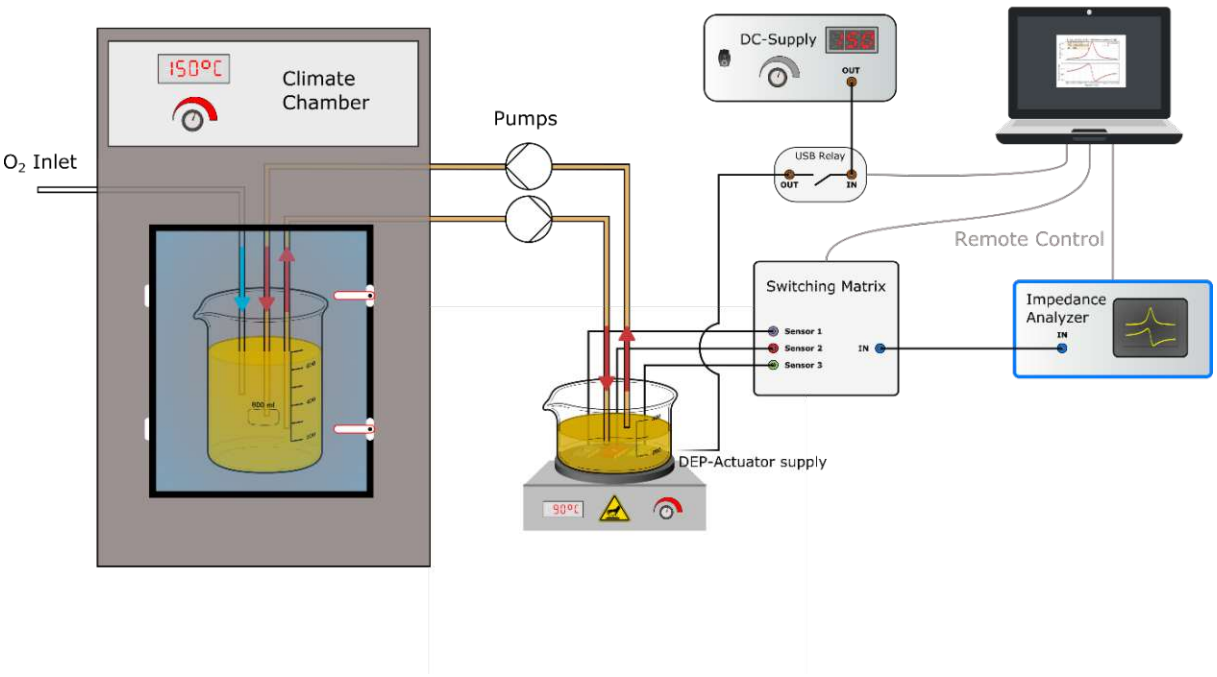

Figure 5-5: Experimental setup to show the on-line lubricant condition monitoring capability of the varnish particle sensor: A glass beaker is filled with turbine oil and heated to 150°C in a temperature-controlled climate chamber. Pure oxygen is introduced at a rate of 3 l/h to promote the oxidation of the oil. A peristaltic pump transfers oil into an external glass beaker in which three varnish sensors are immersed. The oil is kept at a constant temperature of 90°C with a hot plate. The sensors are subsequently connected to the impedance analyser by a switching matrix to determine their resonance frequency. An USB-controlled relay separates the DEP actuators from the DC voltage source during the measurement. The devices are remote controlled, and the data is recorded by a laptop running a Python script.

5.2.2 Varnish sensor results and lubricant condition

After the experiment, the recorded conductance spectra were analysed to determine the resonance frequency and Q factor. Initially, the procedure described in section 2.2.3 was used to fit the BvD-Model to the data. Due to size of the test setup and resulting cable lengths, the influence of parasitic elements, such as the capacitance and resistance introduced by the feed lines and switching matrix, rendered it impossible to use this method with satisfactory precision (Figure 5-6). However, the resonance frequency and Q factor can be determined using an alternative evaluation method described by Marshall *et al.* (Figure 5-7) [219]. The frequency dependent susceptance $B(\omega)$ is divided by the angular frequency

ω and plotted over the frequency f. The local maxima and minima of this function are called f_- and f_+, respectively and are related to the resonance frequency and Q factor by

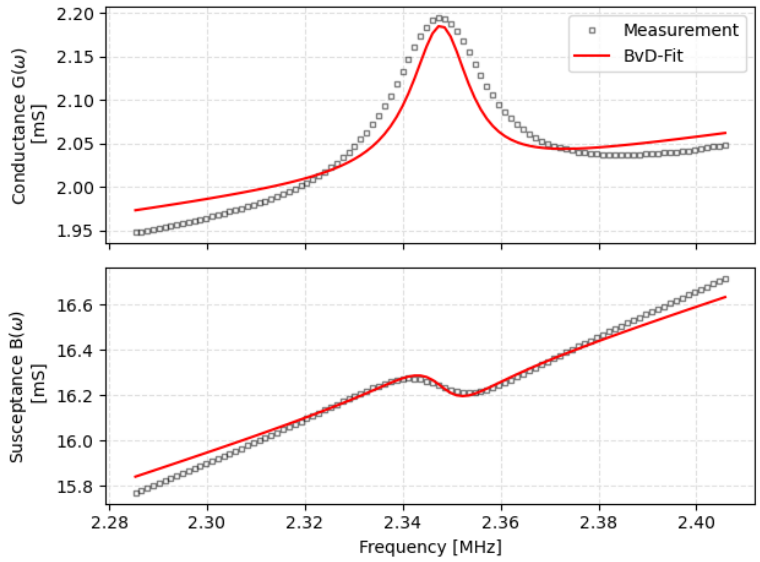

Figure 5-6: BvD-Model fitted to measurement data of Sensor 1. The fit quality is not satisfactory due to the influence of parasitic influences that are not included in the BvD-Model.

$$f_r = \sqrt{\frac{f_+^2 + f_-^2}{2}} \tag{5.2}$$

$$Q = \frac{2f_r^2}{f_+^2 - f_-^2}. \tag{5.3}$$

Using this method, it was possible to determine the resonance frequency and quality factor of all sensors even in later stages of the experiment.

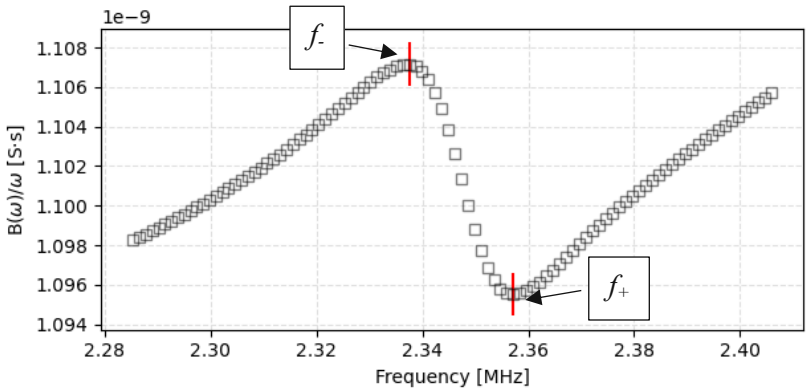

Figure 5-7: Local minima and maxima of the function B(ω)/ω are used to calculate the resonance frequency and Q factor, as described by Marshall et al [219].

The results are depicted in Figure 5-8. The top row shows the resonance frequencies for the active and reference cantilever of the three sensors, respectively. The bottom row depicts the corrected resonance frequency shift, which was calculated in the same way as in the previous chapter by subtracting the measured shift of the reference cantilever from the shift of the active particle accumulating cantilever. Since this calculation involves the subtraction of similar-sized quantities (resonance frequency shift of the active subtracted by the resonance frequency shift of the reference cantilever), even small deviations due to measurement uncertainties lead to a relatively large deviation of the calculated corrected resonance frequency shift (bottom row of Figure 5-8). However, the trend of the corrected resonance frequency shift allows to distinguish five different regions during the experiment:

1. *Stabilization phase* (0 hours - 4 hours): System heats up, DEP actuators not powered.
2. *First rapid decay* (4 hour - 12 hours): DEP actuators are powered, rapid decay of 1-2 kHz.
3. *Plateau* (12 hours - 30 hours): Resonance frequency shift rate is reduced.
4. *Second rapid decay* (30 hours - 60 hours): Rapid decay of resonance frequency.
5. *Saturation* (60 hour – end of experiment): consolidation phase around a final value of 8 kHz (Sensor 1 & 3) or 5 kHz (Sensor 2).

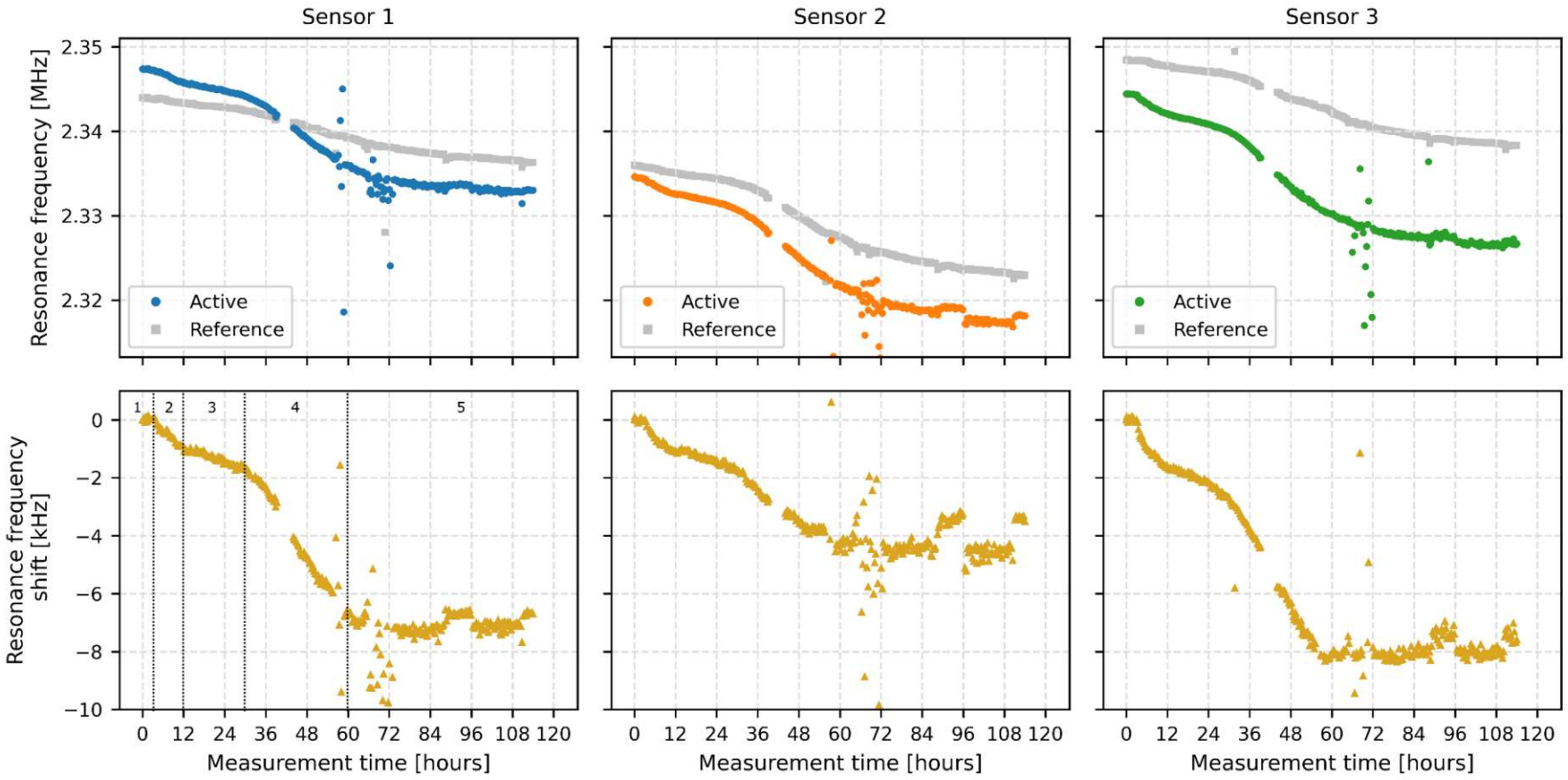

Figure 5-8: Experimental results for the varnish particle sensors in the test rig: The upper row shows the as-measured resonance frequencies for the active (blue) and reference (orange) cantilevers of each sensor, respectively. The bottom row shows the corrected resonance frequency shift, which is calculated by subtracting the shift of the reference cantilever from the active cantilever data. The dashed lines in the graph on the lower left marks five distinguishable regions in the trend of the resonance frequency shift (see text): 1 – Stabilization, 2 – first rapid decay, 3 – plateau, 4 – second rapid decay, 5 – saturation.

During the first four hours, the test rig was heated up and allowed to reach thermal equilibrium. As no voltage was applied to the DEP actuators of the active cantilevers, no resonance frequency shift is observed in this period.

After four hours, the voltage supply for the DEP actuators was activated, resulting in a rapid decay of resonance frequency of 1 to 2 kHz in eight hours, followed by a plateau where the rate of resonance frequency decay and hence particle accumulation rate is significantly lower. There are several scenarios which must be considered to explain this behaviour. The decay of accumulation rate after the first rapid decrease indicates that less particles are accumulated in a given period of time. This can be due to (a) lower particle count in the oil, (b) less particles are accumulated while the particle count in the oil remains constant or, (c) same particle accumulation rate but the adsorbed particles have less influence on the cantilever's resonance frequency. The latter would indicate that the particle mass approaches the cantilever mass so that it no longer operates in a linear regime. This explanation can be ruled out, since after 30 hours another rapid decay of the resonance frequency is observed, showing that the mass responsivity has not been affected by mass overloading. A similar reasoning can be applied to the assumption that the particle count in the oil stays unchanged and the reduced resonance frequency shift is attributed to a lower accumulation rate of the DEP actuators. This would imply that the particles accumulated during the first 12 hours shield the electric field and hence, reduce the DEP force acting on the still suspended varnish particles. However, the observed rapid decay of the resonance frequency after 30 hours suggests that the DEP force remains unaffected by the previously accumulated particles on the sensor surface. Therefore, the change in the resonance frequency shift is likely caused by a lower number of particles in the lubricating oil. A possible explanation is that unstable oil components are rapidly oxidised in the first hours of the experiment and initially form a large number of varnish particles. As these particles are suspended by the detergent and dispersant additives of the oil, the number of free polar varnish particles decreases until additive levels are depleted [161]. However, due to the complex composition and interactions of the additives with the base oil, a detailed investigation of this behaviour must be conducted on the molecular level using, *e.g.*, mass spectroscopy and is not within the scope of this thesis [220].

In the later phase of the experiment, additive levels are exhausted and the lubricating oil oxidizes, leading to the rapid resonance frequency shift observed after 30 hours. This interpretation is supported by the increased slope of the measured infrared absorption in the carbonyl band (1710 cm^{-1}) in dependence of the experiment duration, indicating a faster progressing oxidation of the lubricating oil (Figure 5-12). The decay of resonance frequency persists until an experiment duration of 60 hours, where abrupt saturation is observed. Depending on the sensor, the measured total resonance frequency shift after 60 hours was approximately 8 kHz (Sensor 1 & 3) and 5 kHz (Sensor 2). A closer inspection of the resonance frequency graph of Sensor 2 shows that the magnitude of the active cantilever's resonance frequency shift is similar to that of the other sensors. However, also the resonance frequency

shift of the reference cantilever is much more pronounced leading to a corrected resonance frequency shift ($\Delta f_{act} - \Delta_{ref}$) of only 5 kHz. This is attributed to the installation position of Sensor 2 during the experiment which was located close to the oil inlet in the external beaker. The direct exposure of the sensor to the particle-contaminated oil flow led to a higher amount of randomly deposited particles than for the other sensors that were not located in the direct flow field of the inlet. This circumstance can clearly be seen in the optical micrographs of the cantilever surfaces depicted in Figure 5-9, where the reference cantilever of Sensor 2 is subjected to many randomly distributed particles across its entire surface. In comparison, the reference cantilever of Sensor 1 is only sparsely covered by particles. The gaps in the measurement data between approx. 36 h and 48 h were due to a forced operating system update of the laptop used for controlling the relays and impedance analyser, leading to the loss of the measured conductance spectra. However, the relays of the DEP actuators are normally closed, hence varnish particles where still accumulated during this period.

Assuming a sensor mass responsivity of 13 Hz/ng for the sensors (cf. section 4.3), the accumulated mass for each sensor was calculated and is depicted in Figure 5-10. The calculated mass values are shown as semi-transparent circles, while solid lines are used to illustrate the overall trend and serve as a guide to the eye. Sensor 1 and Sensor 3 show a very similar behaviour and saturate around a value of 600 ng after a measurement time of 60 hours. As explained above, Sensor 2 is subjected to many randomly adsorbed particles which led to a lower corrected resonance frequency shift and hence a calculated accumulated mass of only approximately 350 ng.

The Q factor of the three sensors is depicted in Figure 5-11. As for the resonance frequency shift, the calculation of the Q factor involves the subtraction of similar-sized quantities (cf. Eq 5.3) leading to a sometimes erratic behaviour of the deduced Q factor, due to uncertainties when determining the local minima and maxima of the function B/ω. This loss of precision was also noted by Marhsall *et al.* [219]. However, the quality of data is sufficient to detect a significant decrease in Q factor for all three sensors. At the start of the experiment, all cantilevers exhibit a Q factor in the range of 105-120. As accumulation proceeds, the Q factor of the active cantilevers of Sensors 1 and 3 decrease to a value approximately 60 and a value of 40 for Sensor 2. This decrease in Q factor can be attributed to the dampening effect of the accumulated particle layer (cf. section 4.3.4). This is in agreement with the trend of the Q factors of the reference cantilevers, showing a less pronounced decrease, as they are mainly influenced by the oil's changing liquid properties.

A detailed study of the lubricant condition by conventional analysis techniques is given in Table 5.3 and Figure 5-12. The viscosity shows an initial sharp rise above average within the first 12 hours and increases linearly after. The initial jump can be attributed to the evaporation of light ends (short chain hydrocarbons with a low boiling point) and the formation of particles due to the oxidation of thermal-oxidatively instable oil components (as described above) [50]. However, the change of viscosity affects both the active and reference cantilever, hence the influence on the corrected resonance frequency shift

is negligible. A similar trend is seen for the neutralization number, where an initial increase is measured followed by an only slight increase. This behaviour is consistent with other studies, where no clear correlation between the neutralization number and the formation of varnish was found [50]. The gravimetric analysis of the residues after filtering the oil shows no clear trend, underlining the questionable applicability of this analysis technique for the determination of varnish particles due to their temperature-dependent solubility in oil [207]. There is, however, a significant increase of the IR absorption in the carbonyl band (1710 cm^{-1}). The absorption increases linearly to approx. 1.7 A/cm after 111 hours. However, during the first 24 hours, the slope of the FTIR absorbance graph is lower compared to the region of 36 hours and above. As explained above, this is consistent with the measured resonance characteristics of the varnish sensors, where a fast increase in resonance frequency shift was measured after approximately 30 hours. The slower increase of FTIR absorbance during the first hours of the experiment can be attributed to the antioxidant additives, that effectively decompose degradation products such as varnish precursor molecules, therefore counteracting the formation of varnish particles. The steep increase in FTIR absorbance after 36 hours indicates a depletion of the antioxidant levels progressively increasing oxidation of the bulk oil [221].

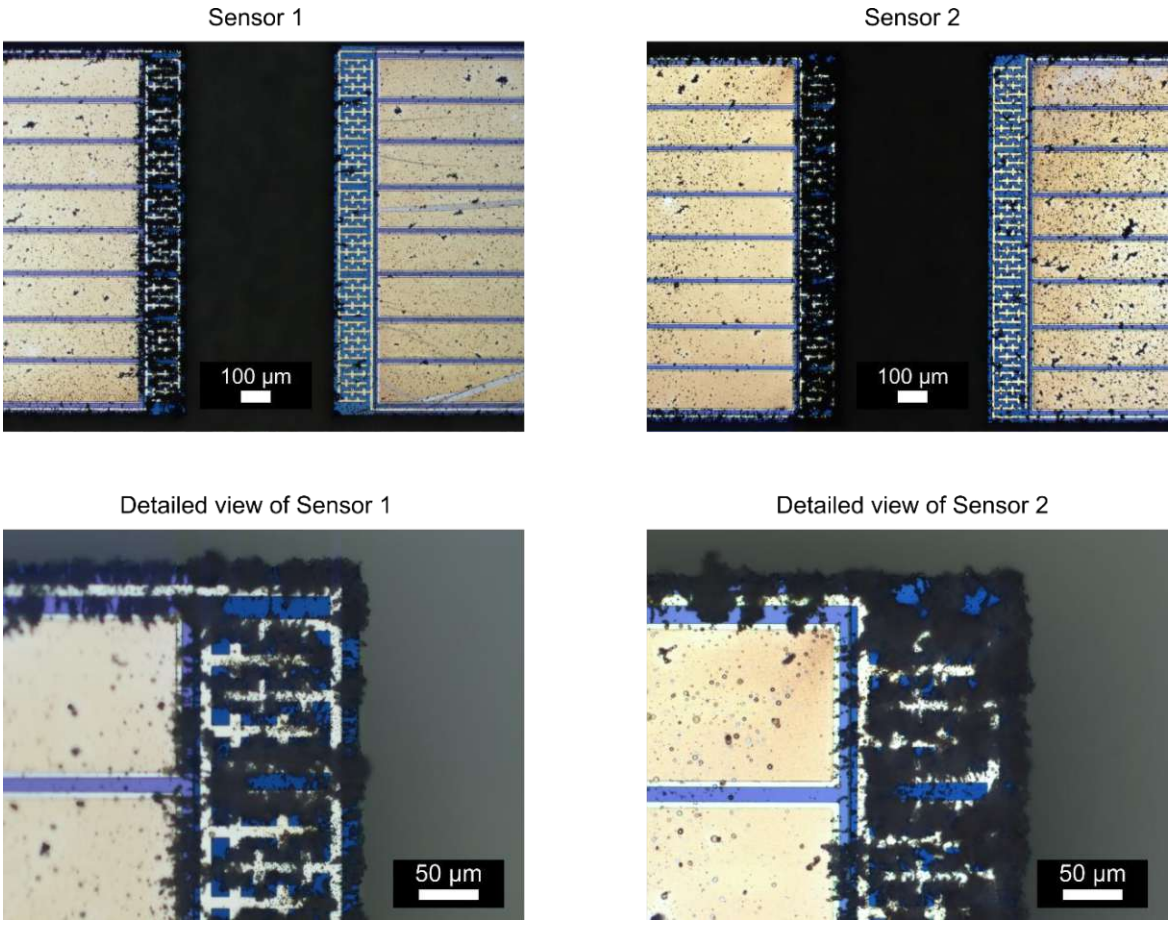

Figure 5-9: Optical micrograph of the active (left) and reference (right) cantilever after 120h. The DEP actuators of the active cantilevers are covered by particles, as seen in the detailed view of the sensors. Additionally, randomly distributed particles are visible on both cantilevers.

Table 5.3: Results of the laboratory analysis of the oil samples that were taken during the experiment.

Experimental time [hours]	Kinematic viscosity (40°C) [mm²/s]	Kinematic viscosity (100°C) [mm²/s]	Neutralization number [mg KOH/g]	FTIR absorbance at 1710 cm^{-1} [A/cm]	Gravimetric analysis (filter residue) [mg/kg]
0	43.702	7.0571	0.083	-	-
12	44.183	7.1124	0.135	0.14	250
24	44.308	7.1269	0.120	0.21	342
36	44.437	7.1416	0.110	0.39	262
48	44.579	7.1626	0.115	0.60	213
60	44.778	7.1807	0.111	0.87	177
72	44.903	7.1931	0.143	1.08	336
84	45.121	7.2166	0.135	1.34	323
96	45.275	7.2349	0.177	1.49	203
111	45.452	7.2514	0.177	1.73	202

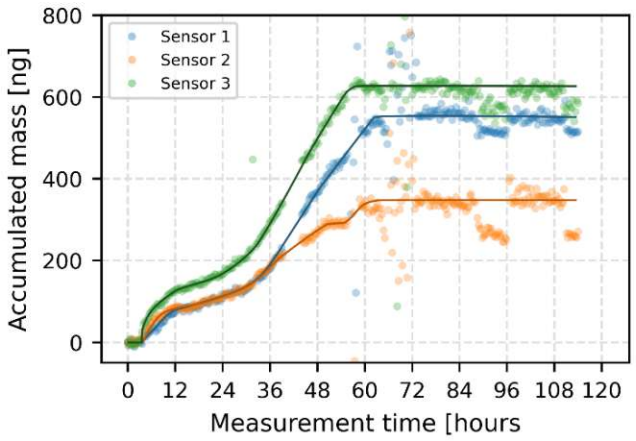

Figure 5-10: Accumulated mass over time for the three sensors. The coloured circles depict the mass values as calculated using a mass responsivity of 13 Hz/ng. The solid lines are intended as a guide to the eye.

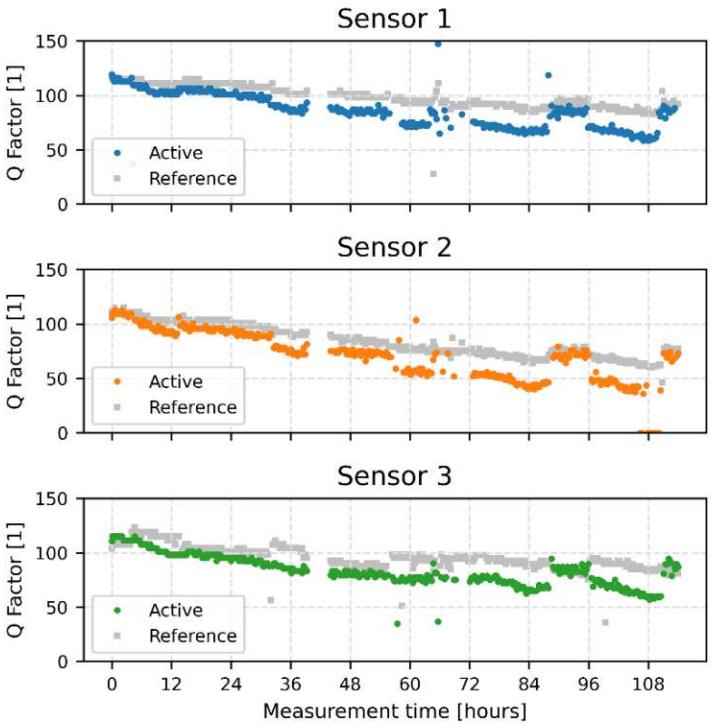

Figure 5-11: Deduced Q factors in dependence of the measurement time for the active and reference cantilever of Sensors 1-3.

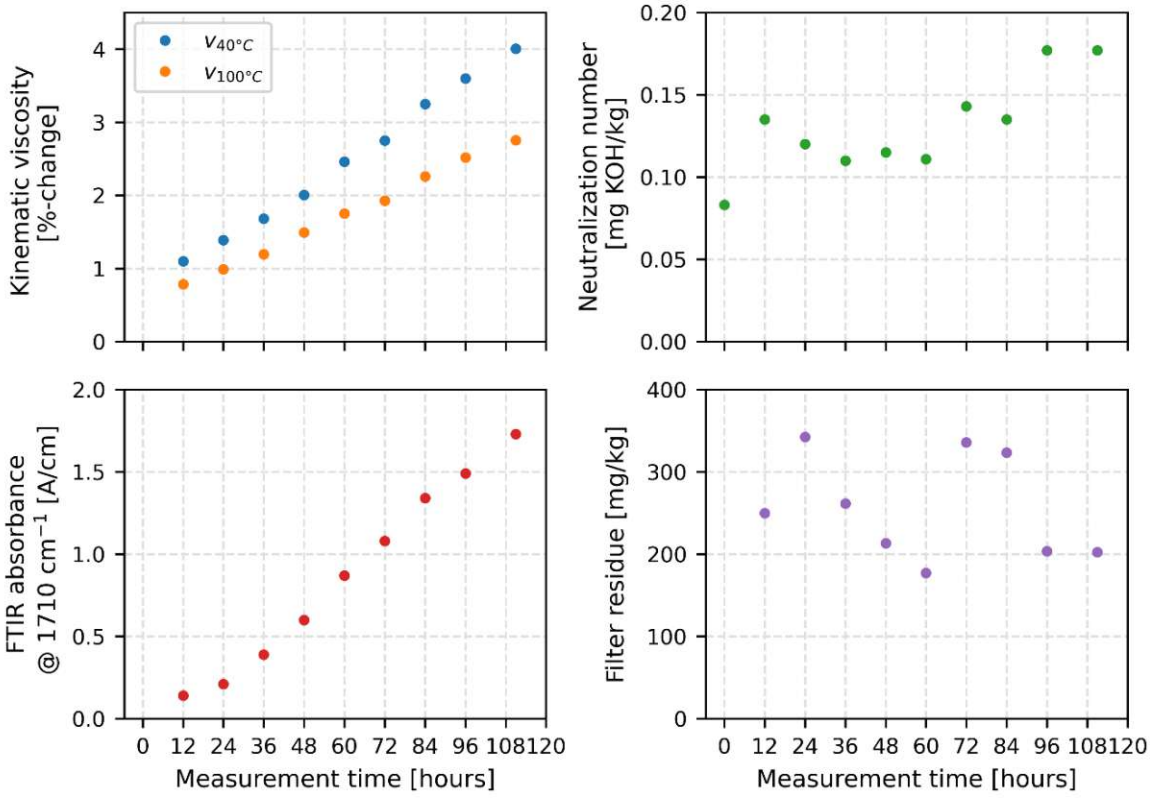

Figure 5-12: Graphical representation of the laboratory analysis results of the oil samples taken during the operation of the test rig.

5.2.3 Discussion

The results of this chapter validate the real-time monitoring capabilities of the sensor under realistic conditions. All three sensors showed a clear response to the changes in oil quality, with two out of three sensors giving comparable results. The measurement of the third sensor showed a similar trend, but a significantly lower resonance frequency shift. This was attributed to unsuitable positioning in the oil aging setup and hence, strong influence of randomly adsorbed particles on the reference cantilever.

All sensors showed sudden saturation after 60 hours, after which no significant change of the resonance frequency characteristics was observed. This behaviour was attributed to the shielding effect of the inhomogeneous electrical field by accumulated particles which impeded further depositing of suspended particles in the oil. It should be noted that the test rig was designed to simulate the entire operational lifetime of the oil within a few days. In a real industrial environment, the rate of oil deterioration is much lower, therefore the expected lifetime of the sensor is much longer than shown in this experiment. Ideally, the sensor should be replaced before saturation is reached, as it is not possible to correlate the resonance frequency shift with particle loading after that point. In the later stages of the experiment, difficulties sometimes arose in reliably determining the resonance frequency of the cantilevers. As already explained earlier, this is due to reduction of the Q factor with increasing particle coverage in combination with parasitic elements introduced by the long feed lines and switching matrix. A possible solution could be to swap the roles of active and reference cantilever above a certain Q factor threshold, whereby the possible operating time can theoretically be doubled. Additionally, the long feed lines could be avoided by integrating the interfacing electronics needed for exciting and reading the sensor on the sensor die (application-specific integrated circuit ASIC).

Apart from FTIR, the conventional oil analysis techniques show no clear trend that indicates the formation of varnish particles in the oil. This again underlines the advantage of the novel developed varnish particle sensor. Due to the accumulation of particles, the particles are directly detected by their influence on the cantilever's resonance frequency, which is in contrast to the conventional oil analysis techniques that can only indicate an oil condition, where varnish built-up can probably happen.

6 Summary and Outlook

In this thesis the application of resonant MEMS cantilevered sensors for condition monitoring of lubricating oil was studied. The work focused on the real-time detection of suspended particles in the lubricating oil, which is an important enabler for inline monitoring of lubricant condition for, *e.g.*, predictive maintenance of critical infrastructure such as gas turbine and other heavy industrial machinery. For such applications, two types of particles are of particular interest and defined the scope of this thesis:

1) *Ferrous metallic particles created by wear processes within the lubricated machinery:* this type of particle is always present during normal operation of lubricated machinery. However, a sudden increase in particle size and concentration is indicative for abnormal wear process caused by, *e.g.*, a broken bearing or a loss of lubrication in moving machine parts. Since the immediate detection of such abnormal wear is of utmost importance for critical infrastructure such as gas turbines and other heavy industrial machinery, a novel sensor offering real-time monitoring capabilities was developed.

2) *Dielectric oxidation-related varnish particles due oil degradation:* these particles create deposits on metallic surfaces in the machinery, leading to stuck valves, increased friction in bearings and clogged oil filters. The presence of such particles can remain undetected for a considerable time, as the complex processes involved in their formation are difficult to identify using conventional methods for determining oil quality. Therefore, a novel sensor was developed to enable the detection of oxidative deterioration of oil.

The basis for this study are piezoelectrically-driven MEMS microcantilevers excited in the so-called roof tile-shaped eigenmodes. These two-dimensional modes exhibit excellent vibrational characteristics (high quality factor, *i.e.,* low damping) in fluids, allowing for precise determination of the resonance frequency, even in high-viscous fluids such as lubricating oils. The general assumption is that suspended particles can be detected when they adhere to the cantilever surface and therefore change the cantilever's vibrational characteristics, namely the resonance frequency and Q factor. For mass detection applications, the relationship between the measured resonance frequency shift and added mass is needed. Since the mass responsivity (resonance frequency shift per unit mass change) depends on the exact position of the added mass on the cantilever, an exact knowledge of the vibrational mode shape is necessary. For conventional one-dimensional eigenmodes found in MEMS cantilevers the mode shape functions can readily be derived with analytical expressions. However, no such expression is available for the roof tile-shaped eigenmodes. An alternative procedure was used in this thesis to derive the mode

shape function using the finite element method (FEM) and the results where experimentally verified by adding a probing mass (silica microbeads) to the cantilever surface subsequently to multiple locations. The resulting resonance frequency shift was measured and used to map the position-dependent mass responsivity of the fundamental roof tile-shaped eigenmode of a 1000x1000x20 μm^3 microcantilever. Using the FEM-derived mode shape function, the comparison with an analytical expression to calculate the resonance frequency shift showed excellent agreement for most positions, demonstrating the validity of this approach. However, in regions of low vibrational amplitude and/or high spatial gradient of the mass responsivity larger deviations were detected. This result implies that these areas shall not be used for resonant mass sensing as small errors in determining the mass position lead to large deviations of the deduced mass values. Based on these findings, two novel MEMS microcantilever sensors for the detection of particles in lubricating oils were developed.

For the detection of ferrous wear particles, a piezoelectrically-driven MEMS cantilever with an integrated planar electromagnetic coil on the free end was designed. The sensor operates fully submerged in the lubricating oil and utilizes the magnetic field generated by the coil to accumulate the particles on the cantilever surface. Every sensor chip consists of two identical cantilevers that allow for a differential measurement scheme. While one cantilever actively accumulates particles using the integrated coil, the coil of the second cantilever is left unpowered, hence it does not actively accumulate wear particles on the surface. Doing so, the second cantilever serves as a reference to detect changes in the environmental conditions. This measurement procedure allows to correct the detected resonance frequency shift of the actively accumulating cantilever for environmental influences on the resonance frequency, such as temperature variations of the surrounding liquid. Initially it was planned to excite the cantilever using the piezoelectric stack while simultaneously determining the resonance characteristics by measuring the complex admittance spectrum with an impedance analyzer. However, due to the sensor design having overlaps between the coil supply lines and the piezoelectric stack, severe crosstalk was generated, so an optical method to detect the resonant frequency during the experiments had to be used. The MEMS sensor concept was validated by submerging the sensor in a suspension consisting of 250 nm Fe_3O_4 particles in deionized water at a concentration of 350 ppm. This suspension was used as a model system because hydrophobic ferrous particles dispersed in oil were not available at that time. The coil of the active cantilever was powered with an electrical current of 150 mA and the resonance frequency was monitored for approximately 120 min. The sensor showed a distinct response to the ferromagnetic particles and successful accumulation was verified with an optical microscope. A total particle mass of 490 ng was accumulated, resulting in a resonance frequency shift of 5916 Hz. This corresponds to a mass responsivity of 12.07 Hz/ng. This value is comparable to values found in other studies concerning mass detection in liquid environments and underlines the outstanding performance of the roof tile-shaped modes for mass detection in liquid environments. The theoretical sensor detection range spans three orders of magnitudes from 90 nm up to 185 µm, making the sensor applicable for in-line detection of ferrous wear debris in lubricated machinery.

Oxidation-related varnish particles pose a great problem for lubricated machinery as they adhere to surfaces that exposed to the oil, leading to build-up of thick deposits. However, an early experiment in this thesis showed that the accumulation of varnish particles on the sensor surface must be actively promoted in order to be able to detect the formation of particles at an early stage. For this purpose, tailored interdigitated electrodes were integrated on the sensor surface to create an electric field that interact with varnish particles due to their polar characteristics. Using SEM/EDX it was verified that this method can promote the deposition of varnish particles on the sensor surface. The design of the MEMS sensor was revised several times due to problems in the fabrication of the insulation between the interdigitated electrodes and the piezoelectric stack. In the final sensor design the need for a dedicated insulation was eliminated by avoiding overlaps between the interdigitated electrodes and the piezoelectric stack. Again, two identical cantilevers were integrated on the sensor chip to allow for a differential measurement scheme. The sensor concept was validated by exposing the sensor to a set of artificially aged turbine oils at various stages of oil deterioration while continuously measuring its resonance characteristics using an impedance analyzer. The sensor response in terms of resonance frequency and Q factor was compared to the results of conventional oil analysis techniques and showed a clear correlation with the oil condition. Based on the results a mass responsivity of 13 Hz/ng, and a limit of detection of approximately 3.5 ng was determined. The comparison to conventional analysis procedures such as viscosity, neutralization number and FTIR shows the advantage of the developed microcantilever sensor. Due to the measurement principle, the direct detection of the varnish particles is possible, rather than monitoring changes of oil parameters that can only indicate the formation of varnish particles.

To demonstrate the applicability of the sensor in an industrial environment for real-time monitoring of the oil condition, two test rigs were developed that simulate the conditions found in the oil circuit of lubricated machinery. In the first test rig, the sensor was placed in the oil circuit and allowed to accumulate particles for a duration of 7 days without a continuous measurement of the resonance characteristics. After removal from the oil circuit, the sensor's resonance frequency was characterized off-line and a clear correlation between the accumulated particle mass and the aging duration of the oil was found. This experiment showed that the sensor is capable of accumulating particles under the conditions (temperature, oil flow) found in lubricated machinery. The second test rig was designed to show the real-time detection capabilities of the sensor. Oil was pumped in between a climate chamber, simulating the hot spots in the oil circuit, and an oil container, simulating the oil well of the machinery. Three MEMS sensors were integrated and the vibrational characteristics were monitored with an impedance analyzer for a duration of approximately 110 hours to detect the build-up of varnish particles. All three sensors gave plausible results corresponding to the oil quality, as measured by conventional oil analysis techniques. Due to the long experiment duration and the resulting excessive build-up of varnish on the sensor surface, the determination of the resonance frequency suffered reliability issues in later stages of the experiment. This circumstance was amplified by the large dimensions of the test setup,

resulting in long sensor supply lines. However, the data obtained during this experiment was sufficient to validate the sensor concept for the real-time monitoring of varnish particles in lubricated machines.

In the present work, the behavior of the developed MEMS sensors was correlated with the results of conventional analytical methods used in the industry to evaluate oil condition. For a deeper understanding, future research efforts should focus on the in-depth analysis of the chemical changes in the oil and the associated behavior of the sensor using advanced chemical analysis techniques. These methods enable the precise quantification of individual chemical components, allowing the sensor to be optimized in terms of sensitivity and robustness and potentially expanding its application to the detection of other deterioration products.

In the current sensor design, the crosstalk between the particle-accumulating structures on the sensor surface and the piezoelectric stack posed a challenge during the measurements. The removal of overlaps between these elements in the final iteration of the varnish sensor improved the crosstalk significantly. A reliable measurement, however, was only possible by temporarily deactivating the interdigitated electrodes during the measurement of the vibrational characteristics. Revising the routing of the supply leads and introducing shielding structures could improve the sensor performance significantly. To drive the sensors towards industrialization, the interface electronics for excitation and for read out of the vibration characteristics must be integrated into the sensor chip. This also prevents long signal paths, which made it difficult to determine the conductance spectrum, particularly in the final phases of the experiment in section 5.2.

Another interesting aspect are the different approaches to operate the cantilevers on the sensor chip. As the accumulated particles have a negative effect on the vibration properties of the cantilever (decrease in the Q factor due to internal losses), the operational life of the sensor is limited in time. Changing the roles of the active and reference cantilevers at a certain threshold value can theoretically double the deployment time of the sensor, which is important for the economical use of the sensor in an industrial environment.

7 Bibliography

[1] D. Dowson, History of Tribology, WILEY, 1998.

[2] N. K. Myshkin and L. V. Markova, "Methods and Instruments for Condition Monitoring of Lubricants," in *On-line Condition Monitoring in Industrial Lubrication and Tribology*, Cham, Springer International Publishing, 2018, p. 1–29.

[3] D. E. Chasan, "Gas Turbine Engine Lubricants," in *Encyclopedia of Tribology*, Springer US, 2013, p. 1460–1467.

[4] L. V. Markova, N. K. Myshkin, M. S. Semenyuk, V. M. Makarenko, A. V. Kolesnikov, H. Kong, H. G. Han and E. S. Yoon, "Methods and instruments for condition monitoring of lubricants," *Journal of Friction and Wear,* vol. 24, p. 50–59, 2003.

[5] L. V. Markova, N. K. Myshkin, H. Kong and H. G. Han, "On-line acoustic viscometry in oil condition monitoring," *Tribology International,* vol. 44, p. 963–970, August 2011.

[6] T. Manzaneque, V. Ruiz-Díez, J. Hernando-García, E. Wistrela, M. Kucera, U. Schmid and J. L. Sánchez-Rojas, "Piezoelectric MEMS resonator-based oscillator for density and viscosity sensing," *Sensors and Actuators A: Physical,* vol. 220, p. 305–315, December 2014.

[7] J. Toledo, V. Ruiz-Díez, G. Pfusterschmied, U. Schmid and J. L. Sánchez-Rojas, "Calibration procedure for piezoelectric MEMS resonators to determine simultaneously density and viscosity of liquids," *Microsystem Technologies,* vol. 24, p. 1423–1431, August 2017.

[8] M. Heinisch, T. Voglhuber-Brunnmaier, E. K. Reichel, I. Dufour and B. Jakoby, "Application of resonant steel tuning forks with circular and rectangular cross sections for precise mass density and viscosity measurements," *Sensors and Actuators A: Physical,* vol. 226, p. 163–174, May 2015.

[9] J. Toledo, T. Manzaneque, V. Ruiz-Díez, F. Jiménez-Márquez, M. Kucera, G. Pfusterschmied, E. Wistrela, U. Schmid and J. L. Sánchez-Rojas, "Comparison of in-plane and out-of-plane piezoelectric microresonators for real-time monitoring of engine oil contamination with diesel," *Microsystem Technologies,* vol. 22, p. 1781–1790, January 2016.

[10] J. Sun, L. Wang, J. Li, F. Li, J. Li and H. Lu, "Online oil debris monitoring of rotating machinery: A detailed review of more than three decades," *Mechanical Systems and Signal Processing,* vol. 149, p. 107341, February 2021.

[11] W. Cao, G. Dong, Y.-B. Xie and Z. Peng, "Prediction of wear trend of engines via on-line wear debris monitoring," *Tribology International,* vol. 120, p. 510–519, April 2018.

[12] T. Tauber, "A new chip detector," *Aircraft Engineering and Aerospace Technology,* vol. 49, p. 4–6, October 1977.

[13] S. Showalter, S. Pingalkar and S. Pasha, "Oil debris monitoring in aerospace engines and helicopter transmissions," in *2012 1st International Symposium on Physics and Technology of Sensors (ISPTS-1)*, 2012.

[14] S. Itomi, "Oil condition sensor". Patent 7151383, 2006.

[15] S. Itomi, "Oil condition sensor". Patent 7112973, 2006.

[16] I. M. Flanagan, J. R. Jordan and H. W. Whittington, "An inductive method for estimating the composition and size of metal particles," *Measurement science and technology,* vol. 1, p. 381, 1990.

[17] R. A. Masom, "The development, proving and application of an in-line metal particle detector (MPD)," *British journal of Non-destructive testing,* vol. 27, p. 159–166, 1985.

[18] B. Howe and D. Muir, "In-line oil debris monitor (ODM) for helicopter gearbox condition assessment," 1998.

[19] J. L. Miller and D. Kitaljevich, "In-line oil debris monitor for aircraft engine condition assessment," in *2000 IEEE Aerospace Conference. Proceedings (Cat. No.00TH8484)*, 2000.

[20] D. Muir and B. Howe, "In-Line Oil Debris Monitor (ODM) for the Advanced Tactical Fighter Engine," in *Aerospace Atlantic Conference & Exposition*, 1996.

[21] I. M. Flanagan, J. R. Jordan and H. W. Whittington, "Wear-debris detection and analysis techniques for lubricant-based condition monitoring," *Journal of Physics E: Scientific Instruments,* vol. 21, p. 1011–1016, November 1988.

[22] L. Du, J. Zhe, J. E. Carletta and R. J. Veillette, "Inductive Coulter counting: detection and differentiation of metal wear particles in lubricant," *Smart Materials and Structures,* vol. 19, p. 057001, March 2010.

[23] L. Du, J. Zhe, J. Carletta, R. Veillette and F. Choy, "Real-time monitoring of wear debris in lubrication oil using a microfluidic inductive Coulter counting device," *Microfluidics and Nanofluidics,* vol. 9, p. 1241–1245, May 2010.

[24] L. Du and J. Zhe, "A high throughput inductive pulse sensor for online oil debris monitoring," *Tribology International,* vol. 44, p. 175–179, February 2011.

[25] L. Du and J. Zhe, "Parallel sensing of metallic wear debris in lubricants using undersampling data processing," *Tribology International,* vol. 53, p. 28–34, September 2012.

[26] L. Du, X. Zhu, Y. Han and J. Zhe, "High Throughput Wear Debris Detection in Lubricants Using a Resonance Frequency Division Multiplexed Sensor," *Tribology Letters,* vol. 51, p. 453–460, July 2013.

[27] L. Du, X. Zhu, Y. Han, L. Zhao and J. Zhe, "Improving sensitivity of an inductive pulse sensor for detection of metallic wear debris in lubricants using parallel LC resonance method," *Measurement Science and Technology,* vol. 24, p. 075106, June 2013.

[28] X. Zhu, L. Du and J. Zhe, "A 3x3 wear debris sensor array for real time lubricant oil conditioning monitoring using synchronized sampling," *Mechanical Systems and Signal Processing,* vol. 83, p. 296–304, January 2017.

[29] X. Zhu, C. Zhong and J. Zhe, "A high sensitivity wear debris sensor using ferrite cores for online oil condition monitoring," *Measurement Science and Technology,* vol. 28, p. 075102, June 2017.

[30] S. Murali, A. V. Jagtiani, X. Xia, J. Carletta and J. Zhe, "A microfluidic Coulter counting device for metal wear detection in lubrication oil," *Review of Scientific Instruments,* vol. 80, p. 016105, January 2009.

[31] S. Murali, X. Xia, A. V. Jagtiani, J. Carletta and J. Zhe, "Capacitive Coulter counting: detection of metal wear particles in lubricant using a microfluidic device," *Smart Materials and Structures,* vol. 18, p. 037001, January 2009.

[32] T. J. Harvey, S. Morris, L. Wang, R. J. K. Wood and H. E. G. Powrie, "Real-time monitoring of wear debris using electrostatic sensing techniques," *Proceedings of the Institution of Mechanical Engineers, Part J: Journal of Engineering Tribology,* vol. 221, p. 27–40, January 2007.

[33] R. Liu, H. Zuo, J. Sun and L. Wang, "Electrostatic monitoring of wind turbine gearbox on oil-lubricated system," *Proceedings of the Institution of Mechanical Engineers, Part C: Journal of Mechanical Engineering Science,* vol. 231, p. 3649–3664, May 2016.

[34] H. Mao, H. Zuo and H. Wang, "Electrostatic Sensor Application for On-Line Monitoring of Wind Turbine Gearboxes," *Sensors,* vol. 18, p. 3574, October 2018.

[35] J. G. Miller, R. E. Clark, M. S. Conradi, D. R. Dietz and J. S. Heyman, "Ultrasonic continuous wave particle monitor". Patent US4015464A, 1977.

[36] J. Edmonds, M. S. Resner and K. Shkarlet, "Detection of precursor wear debris in lubrication systems," in *2000 IEEE Aerospace Conference. Proceedings (Cat. No. 00TH8484)*, 2000.

[37] C. P. Nemarich, H. K. Whitesel and A. Sarkady, "On-line wear particle monitoring based on ultrasonic detection and discrimination," 1988.

[38] X. Zhu, C. Zhong and J. Zhe, "Lubricating oil conditioning sensors for online machine health monitoring – A review," *Tribology International,* vol. 109, p. 473–484, May 2017.

[39] L. Du and J. Zhe, "An integrated ultrasonic–inductive pulse sensor for wear debris detection," *Smart Materials and Structures,* vol. 22, p. 025003, December 2012.

[40] C. Xu, P. Zhang, G. Ren, B. Li, D. Wu and H. Fan, "Discriminating debris particle in lubricant by ultrasonic waveshape features," *Industrial Lubrication and Tribology,* 2015.

[41] S. Raadnui, "Wear particle analysis—utilization of quantitative computer image analysis: A review," *Tribology International,* vol. 38, p. 871–878, October 2005.

[42] Y. Peng, T. Wu, S. Wang and Z. Peng, "Oxidation wear monitoring based on the color extraction of on-line wear debris," *Wear,* Vols. 332-333, p. 1151–1157, May 2015.

[43] W. Yuan, K. S. Chin, M. Hua, G. Dong and C. Wang, "Shape classification of wear particles by image boundary analysis using machine learning algorithms," *Mechanical Systems and Signal Processing,* Vols. 72-73, p. 346–358, May 2016.

[44] Y. Peng, J. Cai, T. Wu, G. Cao, N. Kwok, S. Zhou and Z. Peng, "Online wear characterisation of rolling element bearing using wear particle morphological features," *Wear,* Vols. 430-431, p. 369–375, July 2019.

[45] T. H. Wu, J. H. Mao, J. T. Wang, J. Y. Wu and Y. B. Xie, "A new on-line visual ferrograph," *Tribology transactions,* vol. 52, p. 623–631, 2009.

[46] B. Li, Y. Xi, S. Feng, J. Mao and Y.-B. Xie, "A direct reflection OLVF debris detector based on dark-field imaging," *Measurement Science and Technology,* vol. 29, p. 065104, April 2018.

[47] V. J. Gatto, W. E. Moehle, T. W. Cobb and E. R. Schneller, "Oxidation Fundamentals and Its Application to Turbine Oil Testing," *Journal of ASTM International,* vol. 3, 2006.

[48] J. C. Fitch, S. Gebarin and S. W. Dean, "Review of Degradation Mechanisms Leading to Sludge and Varnish in Modern Turbine Oil Formulations," *Journal of ASTM International,* vol. 3, 2006.

[49] G. Livingstone and D. Oakton, "The emerging problem of lubricant varnish," *maintenance & asset management,* vol. 25, p. 38–42, 2010.

[50] G. J. Livingstone, B. T. Thompson, M. E. Okazaki, C. A. Migdal, A. B. Wardlow and S. W. Dean, "Physical, Performance, and Chemical Changes in Turbine Oils from Oxidation," *Journal of ASTM International,* vol. 4, 2007.

[51] M. D. Brouwer, L. A. Gupta, F. Sadeghi, D. Peroulis and D. Adams, "High temperature dynamic viscosity sensor for engine oil applications," *Sensors and Actuators A: Physical,* vol. 173, p. 102–107, January 2012.

[52] S. Raadnui and S. Kleesuwan, "Low-cost condition monitoring sensor for used oil analysis," *Wear,* vol. 259, p. 1502–1506, July 2005.

[53] A. T. Pérez and M. Hadfield, "Low-Cost Oil Quality Sensor Based on Changes in Complex Permittivity," *Sensors,* vol. 11, p. 10675–10690, November 2011.

[54] J. Schmitigal and S. Moyer, "Evaluation of Sensors for On-Board Diesel Oil Condition Monitoring of U.S. Army Ground Equipment," in *SAE Technical Paper Series*, 2005.

[55] J. Hedges, P. Voelker, R. McCoy and C. Ladd, "An In-Line Method for Measuring Oxidation in Gear Oils and Hydraulic Fluids," *Tribology Transactions,* vol. 49, p. 215–217, July 2006.

[56] S.-I. Moon, K.-K. Paek, Y.-H. Lee, J.-K. Kim, S.-W. Kim and B.-K. Ju, "Multiwall Carbon Nanotube Sensor for Monitoring Engine Oil Degradation," *Electrochemical and Solid-State Letters,* vol. 9, p. H78, 2006.

[57] F. Dickert, O. Hayden, P. Lieberzeit, C. Palfinger, D. Pickert, U. Wolff and G. Scholl, "Borderline applications of QCM-devices: synthetic antibodies for analytes in both nm- and µm-dimensions," *Sensors and Actuators B: Chemical,* vol. 95, p. 20–24, October 2003.

[58] A. Mujahid, A. Afzal, G. Glanzing, A. Leidl, P. A. Lieberzeit and F. L. Dickert, "Imprinted sol–gel materials for monitoring degradation products in automotive oils by shear transverse wave," *Analytica Chimica Acta,* vol. 675, p. 53–57, August 2010.

[59] U. Latif, A. Rohrer, P. A. Lieberzeit and F. L. Dickert, "QCM gas phase detection with ceramic materials—VOCs and oil vapors," *Analytical and Bioanalytical Chemistry,* vol. 400, p. 2457–2462, February 2011.

[60] *DIN 51453:2004-10: Testing of lubricants - Determination of oxidation and nitration of used motor oils - Infrared spectrometric method,* 2004.

[61] A. Abdul-Munaim, T. Holland, P. Sivakumar and D. Watson, "Absorption Wavebands for Discriminating Oxidation Time of Engine Oil as Detected by FT-IR Spectroscopy," *Lubricants,* vol. 7, p. 24, March 2019.

[62] T. Bley, J. Steffensky, H. Mannebach, A. Helwig and G. Müller, "Degradation monitoring of aviation hydraulic fluids using non-dispersive infrared sensor systems," *Sensors and Actuators B: Chemical,* vol. 224, p. 539–546, March 2016.

[63] A. Helwig, G. Müller and S. Paul, "Health Monitoring of Aviation Hydraulic Fluids Using Opto-Chemical Sensor Technologies," *Chemosensors,* vol. 8, p. 131, December 2020.

[64] A. Helwig, G. Müller, J. Rausch, R. Luther, T. Bley, J. Steffensky and H. Mannebach, "Applikationsnahe Erprobung und Weiterentwicklungsperspektiven eines Infrarot-basierten Sensorsystems für die Fluidik—Assessment of an Infrared-Based Sensor System for Fluid Monitoring Applications," in *Proceedings of the AMA Conference, Nürnberg, Germany*, 2014.

[65] V. Macián, B. Tormos, Y. A. Gómez and J. M. Salavert, "Proposal of an FTIR Methodology to Monitor Oxidation Level in Used Engine Oils: Effects of Thermal Degradation and Fuel Dilution," *Tribology Transactions,* vol. 55, p. 872–882, November 2012.

[66] A. Wolak, J. Molenda, G. Zając and P. Janocha, "Identifying and modelling changes in chemical properties of engine oils by use of infrared spectroscopy," *Measurement,* vol. 186, p. 110141, December 2021.

[67] Y. Takezawa, Y. Ito and J. Katagiri, "Automobile oil deterioration diagnosing apparatus". Patent US20020069021A1, 2002.

[68] Y. Takezawa, Y. Ito and J. Katagiri, "Automobile oil deterioration diagnosing apparatus". Patent US20030060984A1, 2003.

[69] M. Sepaniak, P. Datskos, N. Lavrik and C. Tipple, "Peer Reviewed: Microcantilever Transducers: A new Approach in Sensor Technology," *Analytical Chemistry,* vol. 74, p. 568 A–575 A, November 2002.

[70] A. Setiono, M. Bertke, W. O. Nyang'au, J. Xu, M. Fahrbach, I. Kirsch, E. Uhde, A. Deutschinger, E. J. Fantner, C. H. Schwalb, H. S. Wasisto and E. Peiner, "In-Plane and Out-of-Plane MEMS Piezoresistive Cantilever Sensors for Nanoparticle Mass Detection," *Sensors,* vol. 20, p. 618, January 2020.

[71] V. Pachkawade and Z. Tse, "MEMS sensor for detection and measurement of ultra-fine particles," *Engineering Research Express,* vol. 4, p. 022002, June 2022.

[72] J. Xu and E. Peiner, "Resonant Silicon Microcantilevers for Particle and Gas Sensing," in *Springer Series on Chemical Sensors and Biosensors*, Springer Berlin Heidelberg, 2023.

[73] W. O. Nyang'au, T. Kahmann, T. Viereck and E. Peiner, "MEMS-Based Cantilever Sensor for Simultaneous Measurement of Mass and Magnetic Moment of Magnetic Particles," *Chemosensors,* vol. 9, p. 207, August 2021.

[74] K. R. Buchapudi, X. Huang, X. Yang, H.-F. Ji and T. Thundat, "Microcantilever biosensors for chemicals and bioorganisms," *The Analyst,* vol. 136, p. 1539, 2011.

[75] N. V. Lavrik, M. J. Sepaniak and P. G. Datskos, "Cantilever transducers as a platform for chemical and biological sensors," *Review of Scientific Instruments,* vol. 75, p. 2229–2253, July 2004.

[76] T. Braun, V. Barwich, M. K. Ghatkesar, A. H. Bredekamp, C. Gerber, M. Hegner and H. P. Lang, "Micromechanical mass sensors for biomolecular detection in a physiological environment," *Physical Review E,* vol. 72, September 2005.

[77] T. Braun, M. K. Ghatkesar, N. Backmann, W. Grange, P. Boulanger, L. Letellier, H.-P. Lang, A. Bietsch, C. Gerber and M. Hegner, "Quantitative time-resolved measurement of membrane protein–ligand interactions using microcantilever array sensors," *Nature Nanotechnology,* vol. 4, p. 179–185, January 2009.

[78] A. P. Davila, J. Jang, A. K. Gupta, T. Walter, A. Aronson and R. Bashir, "Microresonator mass sensors for detection of Bacillus anthracis Sterne spores in air and water," *Biosensors and Bioelectronics,* vol. 22, p. 3028–3035, June 2007.

[79] J. Jensen, M. Farina, G. Zuccheri, W. Grange and M. Hegner, "Quantitative, Label-Free Detection of the Aggregation of α-Synuclein Using Microcantilever Arrays Operated in a Liquid Environment," *Journal of Sensors,* vol. 2012, p. 1–7, 2012.

[80] S. Leahy and Y. Lai, "A cantilever biosensor exploiting electrokinetic capture to detect Escherichia coli in real time," *Sensors and Actuators B: Chemical,* vol. 238, p. 292–297, January 2017.

[81] Y. Tao, X. Li, T. Xu, H. Yu, P. Xu, B. Xiong and C. Wei, "Resonant cantilever sensors operated in a high-Q in-plane mode for real-time bio/chemical detection in liquids," *Sensors and Actuators B: Chemical,* vol. 157, p. 606–614, October 2011.

[82] Y.-C. Tseng, J.-S. Chang, S. Lin, S. D. Chao and C.-H. Liu, "3,4-Methylenedioxymethylamphetamine detection using a microcantilever-based biosensor," *Sensors and Actuators A: Physical,* vol. 182, p. 163–167, August 2012.

[83] M. Walther, P. M. Fleming, F. Padovani and M. Hegner, "An optimized measurement chamber for cantilever array measurements in liquid incorporating an automated sample handling system," *EPJ Techniques and Instrumentation,* vol. 2, May 2015.

[84] D. Gross, W. Hauger, J. Schröder and W. A. Wall, Technische Mechanik 3, Springer Berlin Heidelberg, 2019.

[85] S. Schmid, L. G. Villanueva and M. L. Roukes, Fundamentals of Nanomechanical Resonators, Springer International Publishing, 2016.

[86] F. Pfeiffer and T. Schindler, Einführung in die Dynamik, Springer, 1989.

[87] S. Dohn, R. Sandberg, W. Svendsen and A. Boisen, "Enhanced functionality of cantilever based mass sensors using higher modes," *Applied Physics Letters,* vol. 86, p. 233501, June 2005.

[88] J. W. Yi, W. Y. Shih and W.-H. Shih, "Effect of length, width, and mode on the mass detection sensitivity of piezoelectric unimorph cantilevers," *Journal of Applied Physics,* vol. 91, p. 1680–1686, February 2002.

[89] J. P. D. Hartog, Mechanical Vibrations, Dover Publications, 2013.

[90] A. W. Leissa, *Vibration of plates,* Washington: Scientific and Technical Information Division, National Aeronautics and Space Administration; [for sale by the Supt. of Docs., U.S. Govt. Print. Off.], 1969.

[91] Bathe, Finite-Elemente-Methoden, BerlinHeidelbergNew YorkBarcelonaHongkong LondonMailandParisTokio: Springer, 2002.

[92] R. Sandberg, K. Mølhave, A. Boisen and W. Svendsen, "Effect of gold coating on theQ-factor of a resonant cantilever," *Journal of Micromechanics and Microengineering,* vol. 15, p. 2249–2253, October 2005.

[93] F. Lochon, I. Dufour and D. Rebière, "A microcantilever chemical sensors optimization by taking into account losses," *Sensors and Actuators B: Chemical,* vol. 118, p. 292–296, October 2006.

[94] J. E. Sader, "Frequency response of cantilever beams immersed in viscous fluids with applications to the atomic force microscope," *Journal of Applied Physics,* vol. 84, p. 64–76, July 1998.

[95] D. R. Brumley, M. Willcox and J. E. Sader, "Oscillation of cylinders of rectangular cross section immersed in fluid," *Physics of Fluids,* vol. 22, p. 052001, May 2010.

[96] J. W. M. Chon, P. Mulvaney and J. E. Sader, "Experimental validation of theoretical models for the frequency response of atomic force microscope cantilever beams immersed in fluids," *Journal of Applied Physics,* vol. 87, p. 3978–3988, April 2000.

[97] A. Maali, C. Hurth, R. Boisgard, C. Jai, T. Cohen-Bouhacina and J.-P. Aimé, "Hydrodynamics of oscillating atomic force microscopy cantilevers in viscous fluids," *Journal of Applied Physics,* vol. 97, p. 074907, April 2005.

[98] C. Vančura, I. Dufour, S. M. Heinrich, F. Josse and A. Hierlemann, "Analysis of resonating microcantilevers operating in a viscous liquid environment," *Sensors and Actuators A: Physical,* vol. 141, p. 43–51, January 2008.

[99] M. C. Cross and R. Lifshitz, "Elastic wave transmission at an abrupt junction in a thin plate with application to heat transport and vibrations in mesoscopic systems," *Physical Review B,* vol. 64, p. 085324, August 2001.

[100] J. A. Judge, D. M. Photiadis, J. F. Vignola, B. H. Houston and J. Jarzynski, "Attachment loss of micromechanical and nanomechanical resonators in the limits of thick and thin support structures," *Journal of Applied Physics,* vol. 101, p. 013521, January 2007.

[101] Z. Hao, A. Erbil and F. Ayazi, "An analytical model for support loss in micromachined beam resonators with in-plane flexural vibrations," *Sensors and Actuators A: Physical,* vol. 109, p. 156–164, December 2003.

[102] D. M. Photiadis and J. A. Judge, "Attachment losses of high Q oscillators," *Applied Physics Letters,* vol. 85, p. 482–484, July 2004.

[103] G. Pfusterschmied, M. Kucera, W. Steindl, T. Manzaneque, V. R. Díez, A. Bittner, M. Schneider, J. L. Sánchez-Rojas and U. Schmid, "Roof tile-shaped modes in quasi free–free supported piezoelectric microplate resonators in high viscous fluids," *Sensors and Actuators B: Chemical,* vol. 237, p. 999–1006, December 2016.

[104] J. Lu, T. Ikehara, Y. Zhang, R. Maeda and T. Mihara, "Energy Dissipation Mechanisms in Lead Zirconate Titanate Thin Film Transduced Micro Cantilevers," *Japanese Journal of Applied Physics,* vol. 45, p. 8795–8800, November 2006.

[105] I. Dufour, F. Lochon, S. M. Heinrich, F. Josse and D. Rebiere, "Effect of Coating Viscoelasticity on Quality Factor and Limit of Detection of Microcantilever Chemical Sensors," *IEEE Sensors Journal,* vol. 7, p. 230–236, February 2007.

[106] R. Lifshitz and M. L. Roukes, "Thermoelastic Damping in Micro- and Nano-Mechanical Systems," *Phys. Rev. B 61, 5600 (2000).,* September 1999.

[107] J. P. Cleveland, S. Manne, D. Bocek and P. K. Hansma, "A nondestructive method for determining the spring constant of cantilevers for scanning force microscopy," *Review of Scientific Instruments,* vol. 64, p. 403–405, February 1993.

[108] T. P. Burg, M. Godin, S. M. Knudsen, W. Shen, G. Carlson, J. S. Foster, K. Babcock and S. R. Manalis, "Weighing of biomolecules, single cells and single nanoparticles in fluid," *Nature,* vol. 446, p. 1066–1069, April 2007.

[109] J. Chaste, A. Eichler, J. Moser, G. Ceballos, R. Rurali and A. Bachtold, "A nanomechanical mass sensor with yoctogram resolution," *Nature Nanotechnology,* vol. 7, p. 301–304, April 2012.

[110] K. Jensen, K. Kim and A. Zettl, "An atomic-resolution nanomechanical mass sensor," *Nature Nanotechnology,* vol. 3, p. 533–537, July 2008.

[111] I. Dufour, S. M. Heinrich and F. Josse, "Theoretical Analysis of Strong-Axis Bending Mode Vibrations for Resonant Microcantilever (Bio)Chemical Sensors in Gas or Liquid Phase," *Journal of Microelectromechanical Systems,* vol. 16, p. 44–49, February 2007.

[112] L. A. Beardslee, A. M. Addous, S. Heinrich, F. Josse, I. Dufour and O. Brand, "Thermal Excitation and Piezoresistive Detection of Cantilever In-Plane Resonance Modes for Sensing Applications," *Journal of Microelectromechanical Systems,* vol. 19, p. 1015–1017, August 2010.

[113] L. A. Beardslee, F. Josse, S. M. Heinrich, I. Dufour and O. Brand, "Geometrical considerations for the design of liquid-phase biochemical sensors using a cantilever\textquotesingles fundamental in-plane mode," *Sensors and Actuators B: Chemical,* vol. 164, p. 7–14, March 2012.

[114] R. Cox, F. Josse, S. M. Heinrich, O. Brand and I. Dufour, "Characteristics of laterally vibrating resonant microcantilevers in viscous liquid media," *Journal of Applied Physics,* vol. 111, p. 014907, January 2012.

[115] S. Heinrich, R. Maharjan, I. Dufour, F. Josse, L. Beardslee and O. Brand, "An analytical model of a thermally excited microcantilever vibrating laterally in a viscous fluid," in *2010 IEEE Sensors*, 2010.

[116] T. Ikehara, J. Lu, M. Konno, R. Maeda and T. Mihara, "A high quality-factor silicon cantilever for a low detection-limit resonant mass sensor operated in air," *Journal of Micromechanics and Microengineering,* vol. 17, p. 2491–2494, November 2007.

[117] L. B. Sharos, A. Raman, S. Crittenden and R. Reifenberger, "Enhanced mass sensing using torsional and lateral resonances in microcantilevers," *Applied Physics Letters,* vol. 84, p. 4638–4640, June 2004.

[118] H. Xie, J. Vitard, S. Haliyo and S. Regnier, "Enhanced Sensitivity of Mass Detection Using the First Torsional Mode of Microcantilevers," in *2007 International Conference on Mechatronics and Automation*, 2007.

[119] J. Hernando, J. L. Sánchez-Rojas, U. Schmid, A. Ababneh, G. Marchand and H. Seidel, "Characterization and displacement control of low surface-stress AlN-based piezoelectric micro-resonators," *Microsystem Technologies,* vol. 16, p. 855–861, January 2010.

[120] M. Kucera, E. Wistrela, G. Pfusterschmied, V. Ruiz-Díez, T. Manzaneque, J. L. Sánchez-Rojas, J. Schalko, A. Bittner and U. Schmid, "Characterization of a roof tile-shaped out-of-plane vibrational mode in aluminum-nitride-actuated self-sensing micro-resonators for liquid monitoring purposes," *Applied Physics Letters,* vol. 104, p. 233501, June 2014.

[121] M. Kucera, E. Wistrela, G. Pfusterschmied, V. Ruiz-Díez, J. L. Sánchez-Rojas, J. Schalko, A. Bittner and U. Schmid, "Characterisation of multi roof tile-shaped out-of-plane vibrational modes in aluminium-nitride-actuated self-sensing micro-resonators in liquid media," *Applied Physics Letters,* vol. 107, p. 053506, August 2015.

[122] G. Pfusterschmied, M. Kucera, C. Weinmann, M. Schneider, A. Bittner, J. L. Sanchez-Rojas and U. Schmid, "Two-step procedure for multi-mode MEMS resonator-based sensing of fluid properties," in *2017 IEEE 30th International Conference on Micro Electro Mechanical Systems (MEMS)*, 2017.

[123] G. Pfusterschmied, M. Kucera, E. Wistrela, T. Manzaneque, V. Ruiz-Díez, J. L. Sánchez-Rojas, A. Bittner and U. Schmid, "Temperature dependent performance of piezoelectric MEMS

resonators for viscosity and density determination of liquids," *Journal of Micromechanics and Microengineering,* vol. 25, p. 105014, September 2015.

[124] G. Pfusterschmied, J. Toledo, M. Kucera, W. Steindl, S. Zemann, V. Ruiz-Díez, M. Schneider, A. Bittner, J. Sanchez-Rojas and U. Schmid, "Potential of Piezoelectric MEMS Resonators for Grape Must Fermentation Monitoring," *Micromachines,* vol. 8, p. 200, June 2017.

[125] J. Toledo, F. Jiménez-Márquez, J. Úbeda, V. Ruiz-Díez, G. Pfusterschmied, U. Schmid and J. L. Sánchez-Rojas, "Piezoelectric MEMS resonators for monitoring grape must fermentation," *Journal of Physics: Conference Series,* vol. 757, p. 012020, October 2016.

[126] J. Toledo, V. Ruiz-Díez, G. Pfusterschmied, U. Schmid and J. L. Sánchez-Rojas, "Flow-through sensor based on piezoelectric MEMS resonator for the in-line monitoring of wine fermentation," *Sensors and Actuators B: Chemical,* vol. 254, p. 291–298, January 2018.

[127] G. Pfusterschmied, C. Weinmann, M. Hospodka, B. Hofko, M. Schneider and U. Schmid, "Sensing Fluid Properties of Super High Viscous Liquids Using Non-Conventional Vibration Modes in Piezoelectrically Excited MEMS Resonators," in *2019 IEEE 32nd International Conference on Micro Electro Mechanical Systems (MEMS)*, 2019.

[128] D. Platz, G. Pfusterschmied and U. Schmid, "Modelling Fluid Damping of Non-Conventional Vibration Modes in MEMS Resonators," *Proceedings,* vol. 2, p. 896, November 2018.

[129] V. Ruiz-Díez, J. Hernando-García, T. Manzaneque, M. Kucera, U. Schmid and J. L. Sánchez-Rojas, "Modelling out-of-plane and in-plane resonant modes of microplates in liquid media," *Journal of Micromechanics and Microengineering,* vol. 25, p. 074005, June 2015.

[130] V. Ruiz-Díez, J. Hernando-García, J. Toledo, T. Manzaneque, M. Kucera, G. Pfusterschmied, U. Schmid and J. L. Sánchez-Rojas, "Modelling and characterization of the roof tile-shaped modes of AlN-based cantilever resonators in liquid media," *Journal of Micromechanics and Microengineering,* vol. 26, p. 084008, July 2016.

[131] G. Pfusterschmied, F. Patocka, C. Weinmann, M. Schneider, D. Platz and U. Schmid, "Responsivity and sensitivity of piezoelectric MEMS resonators at higher order modes in liquids," *Sensors and Actuators A: Physical,* vol. 295, p. 84–92, August 2019.

[132] G. Pfusterschmied, C. Weinmann, M. Schneider, D. Platz, N. Shen, J. Sader and U. Schmid, "Sound dissipation from plate-type resonators excited in non-conventional transversal modes in liquids," *Journal of Micromechanics and Microengineering,* vol. 30, p. 075004, May 2020.

[133] R. M. Martin, "Piezoelectricity," *Physical Review B,* vol. 5, p. 1607–1613, February 1972.

[134] S. Tadigadapa and K. Mateti, "Piezoelectric MEMS sensors: state-of-the-art and perspectives," *Measurement Science and Technology,* vol. 20, p. 092001, July 2009.

[135] J. Hafner, M. Teuschel, J. Schrattenholzer, M. Schneider and U. Schmid, "Optimized Batch Process for Organic MEMS Devices," *Proceedings,* vol. 2, p. 904, November 2018.

[136] *Electronic archive - New Semiconductor Materials. Characteristics and Properties, http://www.ioffe.ru/SVA/NSM/Semicond/ (accessed 08 Sept. 2022).*

[137] A. Iqbal and F. Mohd-Yasin, "Reactive Sputtering of Aluminum Nitride (002) Thin Films for Piezoelectric Applications: A Review," *Sensors,* vol. 18, p. 1797, June 2018.

[138] H. C. Barshilia, B. Deepthi and K. S. Rajam, "Growth and characterization of aluminum nitride coatings prepared by pulsed-direct current reactive unbalanced magnetron sputtering," *Thin Solid Films,* vol. 516, p. 4168–4174, April 2008.

[139] M.-A. Dubois and P. Muralt, "Properties of aluminum nitride thin films for piezoelectric transducers and microwave filter applications," *Applied Physics Letters,* vol. 74, p. 3032–3034, May 1999.

[140] C. M. Lueng, H. L. W. Chan, C. Surya and C. L. Choy, "Piezoelectric coefficient of aluminum nitride and gallium nitride," *Journal of Applied Physics,* vol. 88, p. 5360–5363, November 2000.

[141] S.-R. Jian and J.-Y. Juang, "Indentation-Induced Mechanical Deformation Behaviors of AlN Thin Films Deposited onc-Plane Sapphire," *Journal of Nanomaterials,* vol. 2012, p. 1–6, 2012.

[142] L. Yate, J. C. Caicedo, A. H. Macias, F. J. Espinoza-Beltrán, G. Zambrano, J. Muñoz-Saldaña and P. Prieto, "Composition and mechanical properties of AlC, AlN and AlCN thin films obtained by r.f. magnetron sputtering," *Surface and Coatings Technology,* vol. 203, p. 1904–1907, March 2009.

[143] M. N. Yoder, "Wide bandgap semiconductor materials and devices," *IEEE Transactions on Electron Devices,* vol. 43, p. 1633–1636, 1996.

[144] M. Kucera, T. Manzaneque, J. L. Sánchez-Rojas, A. Bittner and U. Schmid, "Q-factor enhancement for self-actuated self-sensing piezoelectric MEMS resonators applying a lock-in driven feedback loop," *Journal of Micromechanics and Microengineering,* vol. 23, p. 085009, June 2013.

[145] G. Pfusterschmied, M. Kucera, V. Ruiz-Diez, A. Bittner, J. L. Sanchez-Rojas and U. Schmid, "Multi roof tile-shaped vibration modes in mems cantilever sensors for liquid monitoring

purposes," in *2015 28th IEEE International Conference on Micro Electro Mechanical Systems (MEMS)*, 2015.

[146] J.-P. Colinge, Silicon-on-Insulator Technology, Springer US, 1991.

[147] M. J. Madou, Fundamentals of microfabrication: the science of miniaturization, 2 ed., CRC press, 2018.

[148] K. R. Williams and R. S. Muller, "Etch rates for micromachining processing," *Journal of Microelectromechanical Systems,* vol. 5, p. 256–269, 1996.

[149] K. R. Williams, K. Gupta and M. Wasilik, "Etch rates for micromachining processing-part II," *Journal of Microelectromechanical Systems,* vol. 12, p. 761–778, December 2003.

[150] R. A. Haefer, Oberflächen- und Dünnschicht-Technologie, Springer Berlin Heidelberg, 1987.

[151] G. Gerlach and W. Dötzel, Einführung in die Mikrosystemtechnik: ein Kursbuch für Studierende, Fachbuchverl. Leipzig im Carl-Hanser-Verlag, 2006.

[152] S. Nonogaki, U. Takumi and T. Ito, Microlithography Fundamentals in Semiconductor Devices and Fabrication Technology, CRC Press, 2018.

[153] B. Ilic, S. Krylov, K. Aubin, R. Reichenbach and H. G. Craighead, "Optical excitation of nanoelectromechanical oscillators," *Applied Physics Letters,* vol. 86, p. 193114, May 2005.

[154] D. K. Schroder, Semiconductor Material and Device Characterization, Wiley, 2015.

[155] P. Eaton and P. West, Atomic Force Microscopy, OUP Oxford, 2010.

[156] R. Scott, The practical handbook of machinery lubrication, Noria Corporation, 2012.

[157] R. Stribeck, "Die wesentlichen Eigenschaften der Gleit-und Rollenlager," *Zeitschrift des Vereines Deutscher Ingenieure,* vol. 46, p. 1341–1348, 1902.

[158] B. J. Hamrock, S. R. Schmid and B. O. Jacobson, Fundamentals of fluid film lubrication, CRC press, 2004.

[159] M. Eklund, N. Naphthenics, P. Jarman and M. Edwall, Transformer Oil Handbook, Nynäs Naphthenics, 2004.

[160] R. N. Sarma and R. Vinu, "Current Status and Future Prospects of Biolubricants: Properties and Applications," *Lubricants,* vol. 10, p. 70, April 2022.

[161] L. R. Rudnick, Lubricant additives: chemistry and applications, CRC press, 2009.

[162] L. Quick, G. Livingstone and J. Ameye, "Turbine Oils," in *Encyclopedia of Lubricants and Lubrication*, Springer Berlin Heidelberg, 2014, p. 2183–2194.

[163] *ASTM D7042-20: Standard Test Method for Dynamic Viscosity and Density of Liquids by Stabinger Viscometer (and the Calculation of Kinematic Viscosity),* ASTM International, West Conshohocken, PA, USA, 2020.

[164] "DIN 51558-2: Prüfung von Mineralölen - Bestimmung der Neutralisationszahl - Teil 2: Farbindikator-Titration, Isolieröle," Deutsches Institut für Normung, Berlin, Germany, 2017.

[165] *ASTM D4055-04: Test Method for Pentane Insolubles by Membrane Filtration,* ASTM International, West Conshohocken, PA, USA, 2019.

[166] *ASTM D2272-14a: Test Method for Oxidation Stability of Steam Turbine Oils by Rotating Pressure Vessel,* ASTM International, West Conshohocken, PA, USA, 2014.

[167] *ASTM D943-19: Standard Test Method for Oxidation Characteristics of Inhibited Mineral Oils,* ASTM International, West Conshohocken, PA, USA, 2019.

[168] M. Pach, H. K. Zobel and T. Norrby, "Evaluation and Comparison Between Oxidation Stability Test Methods for Turbine Oils," *Journal of ASTM International,* vol. 3, 2006.

[169] *DIN 51545:2023-10: Testing of lubricants and related products - determination of the temperature stability of turbine oils,* 2023.

[170] F. Patocka, M. Schneider, N. Dörr, C. Schneidhofer and U. Schmid, "Position-dependent mass responsivity of silicon MEMS cantilevers excited in the fundamental, two-dimensional roof tile-shaped mode," *Journal of Micromechanics and Microengineering,* vol. 29, p. 045009, February 2019.

[171] J. Tamayo, P. M. Kosaka, J. J. Ruz, Á. S. Paulo and M. Calleja, "Biosensors based on nanomechanical systems," *Chem. Soc. Rev.,* vol. 42, p. 1287–1311, 2013.

[172] M. A. Hopcroft, W. D. Nix and T. W. Kenny, "What is the Young's Modulus of Silicon?," *Journal of Microelectromechanical Systems,* vol. 19, p. 229–238, April 2010.

[173] L. Fadel, I. Dufour, F. Lochon and O. Francais, "Signal-to-noise ratio of resonant microcantilever type chemical sensors as a function of resonant frequency and quality factor," *Sensors and Actuators B: Chemical,* vol. 102, p. 73–77, September 2004.

[174] S. Faegh, N. Jalili and S. Sridhar, "A Self-Sensing Piezoelectric MicroCantilever Biosensor for Detection of Ultrasmall Adsorbed Masses: Theory and Experiments," *Sensors,* vol. 13, p. 6089–6108, May 2013.

[175] N. Nugaeva, K. Y. Gfeller, N. Backmann, M. Düggelin, H. P. Lang, H.-J. Güntherodt and M. Hegner, "An Antibody-Sensitized Microfabricated Cantilever for the Growth Detection of Aspergillus niger Spores," *Microscopy and Microanalysis,* vol. 13, p. 13–17, January 2007.

[176] H. S. Wasisto, S. Merzsch, A. Waag, E. Uhde, T. Salthammer and E. Peiner, "Airborne engineered nanoparticle mass sensor based on a silicon resonant cantilever," *Sensors and Actuators B: Chemical,* vol. 180, p. 77–89, 2013.

[177] N. Bajaj, J. F. Rhoads and G. T.-C. Chiu, "Characterizing the Spatially Dependent Sensitivity of Resonant Mass Sensors Using Inkjet Deposition," *Journal of Dynamic Systems, Measurement, and Control,* vol. 139, July 2017.

[178] W. F. van Dorp and C. W. Hagen, "A critical literature review of focused electron beam induced deposition," *Journal of Applied Physics,* vol. 104, p. 081301, October 2008.

[179] I. Utke, V. Friedli, J. Michler, T. Bret, X. Multone and P. Hoffmann, "Density determination of focused-electron-beam-induced deposits with simple cantilever-based method," *Applied Physics Letters,* vol. 88, p. 031906, January 2006.

[180] K. Nieradka, H. Stegmann and T. Gotszalk, "Focused ion beam milling and deposition techniques in validation of mass change value and position determination method for micro and nanomechanical sensors," *Journal of Applied Physics,* vol. 112, p. 114509, December 2012.

[181] K. A. Telari, B. R. Rogers, H. Fang, L. Shen, R. A. Weller and D. N. Braski, "Characterization of platinum films deposited by focused ion beam-assisted chemical vapor deposition," *Journal of Vacuum Science & Technology B: Microelectronics and Nanometer Structures,* vol. 20, p. 590, 2002.

[182] J. Tamayo, D. Ramos, J. Mertens and M. Calleja, "Effect of the adsorbate stiffness on the resonance response of microcantilever sensors," *Applied Physics Letters,* vol. 89, p. 224104, November 2006.

[183] A. D. Slattery, J. S. Quinton and C. T. Gibson, "Atomic force microscope cantilever calibration using a focused ion beam," *Nanotechnology,* vol. 23, p. 285704, June 2012.

[184] F. Zhao and Z. Chen, "Bidirectional and location-dependent frequency tuning of single crystal 4H-SiC micromechanical cantilevers," *Microsystem Technologies,* vol. 21, p. 1663–1668, June 2014.

[185] S. Dohn, W. Svendsen, A. Boisen and O. Hansen, "Mass and position determination of attached particles on cantilever based mass sensors," *Review of Scientific Instruments,* vol. 78, p. 103303, October 2007.

[186] S. Dohn, S. Schmid, F. Amiot and A. Boisen, "Position and mass determination of multiple particles using cantilever based mass sensors," *Applied Physics Letters,* vol. 97, p. 044103, July 2010.

[187] D. Kim, S. Hong, J. Jang and J. Park, "Simultaneous determination of position and mass in the cantilever sensor using transfer function method," *Applied Physics Letters,* vol. 103, p. 033108, July 2013.

[188] K. Park and R. Bashir, "MEMS-based resonant sensor with uniform mass sensitivity," in *TRANSDUCERS 2009 - 2009 International Solid-State Sensors, Actuators and Microsystems Conference*, 2009.

[189] G. K. Batchelor, An Introduction to Fluid Dynamics, Cambridge University Press, 2010.

[190] L. D. Landau, Fluid mechanics, London, Reading: Pergamon Press Addison-Wesley Pub. Co, 1959.

[191] I. Dufour, E. Lemaire, B. Caillard, H. Debéda, C. Lucat, S. M. Heinrich, F. Josse and O. Brand, "Effect of hydrodynamic force on microcantilever vibrations: Applications to liquid-phase chemical sensing," *Sensors and Actuators B: Chemical,* vol. 192, p. 664–672, March 2014.

[192] B. J. Konijn, O. B. J. Sanderink and N. P. Kruyt, "Experimental study of the viscosity of suspensions: Effect of solid fraction, particle size and suspending liquid," *Powder Technology,* vol. 266, p. 61–69, November 2014.

[193] C. A. V. Eysden and J. E. Sader, "Frequency response of cantilever beams immersed in viscous fluids with applications to the atomic force microscope: Arbitrary mode order," *Journal of Applied Physics,* vol. 101, p. 044908, February 2007.

[194] B. Fan, B. Li, S. Feng, J. Mao and Y.-B. Xie, "Modeling and experimental investigations on the relationship between wear debris concentration and wear rate in lubrication systems," *Tribology International,* vol. 109, p. 114–123, May 2017.

[195] F. Patocka, M. Schlögl, M. Schneider and U. Schmid, "Novel MEMS Sensor for Detecting Magnetic Particles in Liquids," *Proceedings,* vol. 2, p. 868, November 2018.

[196] F. Patocka, M. Schlögl, C. Schneidhofer, N. Dörr, M. Schneider and U. Schmid, "Novel MEMS Sensor for Real-time Lubricant Condition Monitoring," in *ÖTG-Symposium 2018*, 2018.

[197] F. Patocka, M. Schlögl, C. Schneidhofer, N. Dörr, M. Schneider and U. Schmid, "Piezoelectrically excited MEMS sensor with integrated planar coil for the detection of ferrous particles in liquids," *Sensors and Actuators B: Chemical,* vol. 299, p. 126957, November 2019.

[198] A. Agoston, C. Ötsch and B. Jakoby, "Viscosity sensors for engine oil condition monitoring—Application and interpretation of results," *Sensors and Actuators A: Physical,* vol. 121, p. 327–332, June 2005.

[199] A. Munaz, M. J. A. Shiddiky and N.-T. Nguyen, "Recent advances and current challenges in magnetophoresis based micro magnetofluidics," *Biomicrofluidics,* vol. 12, p. 031501, May 2018.

[200] Q. Ramadan, V. Samper, D. Poenar and C. Yu, "On-chip micro-electromagnets for magnetic-based bio-molecules separation," *Journal of Magnetism and Magnetic Materials,* vol. 281, p. 150–172, October 2004.

[201] A. Hamilton, A. Cleary and F. Quail, "Development of a Novel Wear Detection System for Wind Turbine Gearboxes," *IEEE Sensors Journal,* vol. 14, p. 465–473, February 2014.

[202] F. Patocka, M. Schlögl, M. Schneider, C. Schneidhofer, N. Dörr and U. Schmid, "MEMS Sensor for Monitoring the Degradation of Lubricating Oils," in *7th European Conference on Tribology (Ecotrib 2019)-Book of Abstracts*, 2019.

[203] F. Patocka, C. Schneidhofer, N. Dörr, M. Schneider and U. Schmid, "Novel resonant MEMS sensor for the detection of particles with dielectric properties in aged lubricating oils," *Sensors and Actuators A: Physical,* vol. 315, p. 112290, November 2020.

[204] A. Sasaki, S. Uchiyama, M. Kawasaki, D. G. Holt, D. K. Wills and S. W. Dean, "Varnish Formation in the Gas Turbine Oil Systems," *Journal of ASTM International,* vol. 5, 2008.

[205] P. W. R. Smith, C. A. Migdal, A. B. Wardlow and S. W. Dean, "Modern Turbine Oil Oxidation Performance Limits—Meeting and Measuring Them—A Shell Perspective," *Journal of ASTM International,* vol. 4, 2007.

[206] S.-H. Hong and E. K. Jang, "Varnish Formation and Removal in Lubrication Systems: A Review," *Materials,* vol. 16, p. 3737, May 2023.

[207] M. G. Hobbs and P. T. D. Jr., "Lubricant Varnishing and Varnish Mitigation," in *LUBMAT 2014, Manchester, UK (Paper number: L141082)*, 2014.

[208] "ASTM D7843-16: Standard Test Method for Measurement of Lubricant Generated Insoluble Color Bodies in In-Service Turbine Oils using Membrane Patch Colorimetry," ASTM International, West Conshohocken, PA, USA, 2016.

[209] T. Kon, T. Honda and A. Sasaki, "Influence of Solvents, Oil Temperature, and Incubation Period on Membrane Patch Color," *Tribology Online,* vol. 13, p. 225–231, October 2018.

[210] R. Pethig, "Review Article—Dielectrophoresis: Status of the theory, technology, and applications," *Biomicrofluidics,* vol. 4, p. 022811, June 2010.

[211] A. Sasaki and S. Uchiyama, "A New Technology for Oil Management: Electrostatic Oil Cleaner," in *SAE Technical Paper Series*, 2002.

[212] D. S. Bulgarevich, S. Tsukamoto, T. Kasuya, M. Demura and M. Watanabe, "Pattern recognition with machine learning on optical microscopy images of typical metallurgical microstructures," *Scientific Reports,* vol. 8, February 2018.

[213] L. Breiman, "Random forests," *Machine learning,* vol. 45, p. 5–32, 2001.

[214] B. C. Ko, S. H. Kim and J.-Y. Nam, "X-ray Image Classification Using Random Forests with Local Wavelet-Based CS-Local Binary Patterns," *Journal of Digital Imaging,* vol. 24, p. 1141–1151, April 2011.

[215] L. Staniewicz and P. A. Midgley, "Machine learning as a tool for classifying electron tomographic reconstructions," *Advanced Structural and Chemical Imaging,* vol. 1, August 2015.

[216] N. Vyas, R. L. Sammons, O. Addison, H. Dehghani and A. D. Walmsley, "A quantitative method to measure biofilm removal efficiency from complex biomaterial surfaces using SEM and image analysis," *Scientific Reports,* vol. 6, September 2016.

[217] Y. Hongbin, L. Liang and A. G. Yuandong, "Capacitive micromachined ultrasonic transducer (CMUT) based micro viscosity sensor," *Sensors and Actuators B: Chemical,* vol. 227, p. 346–351, May 2016.

[218] A. O. Niedermayer, T. Voglhuber-Brunnmaier, J. Sell and B. Jakoby, "Methods for the robust measurement of the resonant frequency and quality factor of significantly damped resonating devices," *Measurement Science and Technology,* vol. 23, p. 085107, July 2012.

[219] W. J. Marshall and G. A. Brigham, "Determining equivalent circuit parameters for low figure of merit transducers," *Acoustics Research Letters Online,* vol. 5, p. 106–110, July 2004.

[220] O. Lacroix-Andrivet, M. Hubert-Roux, C. L. Bourhis, S. Moualdi, A. L. M. Siqueira and C. Afonso, "Characterization of Base Oil and Additive Oxidation Products from Formulated Lubricant by Ultra-High Resolution Mass Spectrometry," *Lubricants,* vol. 11, p. 345, August 2023.

[221] S. Bots and R. Krethe, "Used Oil Laboratory Tests," in *Encyclopedia of Lubricants and Lubrication*, Springer Berlin Heidelberg, 2014, p. 2213–2252.

[222] *CEC L-48-A00: Oxidation stability of lubricating oils used in automotive transmissions by artificial ageing.,* CEC Working Group, Brussels, Belgium, 2007.